DEVELOPMENT OF CERAMIC FLOOR TILES MADE FROM FERRIC OXIDE SOURCED AS STEEL INDUSTRIAL WASTE

BY

MUGISHA ABEL

22/U/GMEM/404/PE

A DISSERTATION SUBMITTED TO THE DIRECTORATE OF RESEARCH AND GRADUATE TRAINING IN PARTIAL FULFILMENT OF THE REQUIREMENTS FOR THE AWARD OF DEGREE OF MASTER OF SCIENCE IN ADVANCED MANUFACTURING SYSTEMS ENGINEERING OF KYAMBOGO UNIVERSITY

NOVEMBER, 2025

DECLARATION

I, Mugisha Abel, declare that this research dissertation is my original work and has never been presented for a degree award in any University or tertiary institution.

Sign. ..... Date. .....

APPROVAL

This Master of Science Dissertation titled ***"DEVELOPMENT OF CERAMIC FLOOR TILES MADE FROM FERRIC OXIDE SOURCED AS A STEEL INDUSTRIAL-WASTE"***, prepared and submitted by Mugisha Abel has been under our supervision and is ready for examination.

Sign. ..... Date. .....

Dr. Nalubowa Maureen Ssempijja

Department of Mechanical and Production Engineering,

Faculty of Engineering,

Kyambogo University.

Sign. ..... Date. .....

Dr. Ochen William

Department of Physics,

Faculty of Science,

Kyambogo University.

ACKNOWLEDGEMENT

I am incredibly thankful to the supreme God for his love, which has enabled me to stay committed to this academic path. Though I had a number of hurdles throughout this study, He guided me through each step. In addition, I would want to express my gratitude to my supervisors, Dr. Ochen William from Physics department of Kyambogo University and Dr. Maureen Nalubowa SSempijja from Mechanical department of Kyambogo University for their intellectual guidance and unwavering dedication that elevated the quality of my work.

I sincerely extend my deepest gratitude to Mr. Ivan Fredrick Kalega from Uganda Industrial Research Institute (UIRI) for sample processing, Mr. Talemwa Collins from Roofings Rolling Mills (RRM) who helped me to acquire the industrial steel waste. I appreciate the help from Mr. Okumu Lawrence of Kyambogo University for his support in the compressive strength testing. Similarly, to Mr. Wabwire Andrew from Makerere University department of Mechanical Engineering for his support during scanning electron microscope analysis (SEM) and the flexural strength testing of the samples. Finally, I acknowledge the assistance from Dr. Charles Wilson Messo from the department of Geo Sciences, University of Dar es Salaam for his guidance during X-Ray Diffraction analysis (XRD) of the samples.

Words cannot describe my appreciation to my wife, Mrs. Twinobusingye Hildah, for her unwavering financial and spiritual support for the success of this research. I also extend my heartfelt appreciation to my classmates, Mr. Agaba Pius, Mr. Kalanzi Jesouphat, and Mr. Banura Pascal for being a tremendous source of inspiration and for their invaluable peer review of this report.

DEDICATION

I dedicate this work to my children, Musinguzi Jeremiah, Kaganzi Esther, Nimurungi Joella Itangaza, and Arinanye Jemimah, as well as my wife, Twinobusingye Hilda.

TABLE OF CONTENTS

LIST OF ABBREVIATIONS

CCD	Central Composite Design
XRF	X-ray Fluorescence
XRD	X-ray Diffractometer
RSM	Response Surface Methodology
SEM	Scanning Electron Microscope
ARP	Acid Regeneration Plant
PET	Polyethylene Terephthalate
ASTM	American Society for Testing and Materials
CPHA	Coffee Parchment Husks Ash
LPG	Liquefied Petroleum Gas
UIRI	Uganda Industrial Research Institute
RRM	Roofings Rolling Mills
PSD	Particle Size Distribution
MOR	Modulus of Rapture
LOI	Loss of Ignition

LIST OF TABLES

LIST OF FIGURES

ABSTRACT

The goal of this research was to develop ceramic floor tiles made from ferric oxide sourced as an industrial steel waste. Traditional ceramic tiles are made from clay, feldspar, kaolin and sand. These materials are known to deplete over time due to the increasing demand of construction materials such as ceramic floor tiles. Ferric oxide produced from steel industries as waste was used as an alternative to feldspar. The physical and mechanical qualities of fired products were examined. In addition, a scanning electron microscope (SEM) and an X-ray diffractometer (XRD) were used to analyze the microstructure and phase. Furthermore, design expert software was utilized to optimize the attributes of fired products, and the results were compared to experimental data.

The results revealed that the samples containing 15 wt % ferric oxide, 15 wt % feldspar, 20 wt % ball clay, 40 wt % kaolin and 10 wt % sand exhibited the highest flexural strength of 45.3 ± 2.2 MPa (experimental value). The optimized value of the samples containing 15 wt % ferric oxide, 15 wt % feldspar, 20 wt % ball clay, 40 wt % kaolin and 10 wt % sand for flexural strength was 41.6 ± 2.08 MPa (model value). The high flexural strength was attributed to the formation of mullite fibres as corroborated by XRD diffractograms. In addition, the same composition exhibited the lowest water absorption of 9.62 ± 0.481 % (experiment value) and 10.69 ± 0.53 % (model value). This was attributed to the microstructure of the fired products as reported by the SEM micrographs. Therefore, the ceramic tiles developed satisfied ISO 13006 standard, and they can be classified as group BI_a or BII_b simply because their flexural strength was ≥ 35MPa and water absorption was in a range of 6-10 %.

Key words: Industrial waste materials, Ceramic tiles, Sustainability, Vetrification, Mixing ratios.

CHAPTER ONE: INTRODUCTION

1.1 Background of the Study

Globally, the demand for ceramic tiles has been increasing annually and the production reached 18.3 million square meters in 2021, marking a notable 7.2 % increase from the previous year. The current projection of ceramic tile production indicates a steady annual growth rate of 5% (Varghese et al., 2024). In Uganda, the booming construction industry has led to the increase in demand of ceramic tiles. Several tile-manufacturing companies have been established, such as Goodwill Uganda Ceramic Company, Millennium Tiles Uganda Limited and Modern Tiles Limited. As of 2020, Uganda exported ceramic tiles valued at approximately US$ 11 million, reflecting a significant increase from US$ 3 million recorded in 2018. Kenya emerged as Uganda's leading importer of these products, accounting for 81% of the total export share (Panzi Mukhokosi et al., 2023).

The process of making ceramic tiles is intricate and uses a variety of natural raw materials, all of which are essential to the quality of the finished tile. In order to produce ceramic tiles that meet the ISO 13006 standard. The essential materials are carefully chosen and processed (Ekincioglu, 2023). Ceramic tiles are vitreous products made from a triaxial mixture of clay, feldspar and sand. Although clays are the primary component of ceramic tiles, additional elements are added to enhance their qualities (Bayer Ozturk et al., 2024). The raw materials used play different roles for example, ball clay has a high plasticity therefore it helps in the formation of the tile shape (Bombazaro & Bernardin, 2022). When fired at high temperatures of up to 1200 ^{o}C, kaolin increases flexural strength

significantly. This is because it contains a significant amount of aluminum oxide, which facilitates the formation of the mullite phase during the sintering process. The mullite hypothesis states that the mullite needles increase the flexural strength of the fired body (S. Wang et al., 2023). After sintering, feldspar, which includes earth metals, forms a glassy phase that serves as a fluxing agent. This improves vitrification at lower sintering temperatures (Gikunju et al., 2024). Sand works as a filler material and helps in reducing shrinkage and warping of the ceramic tiles (Zheng et al., 2025). All these raw materials are sourced from natural deposits and therefore they can deplete with time. The depletion is exacerbated by the increasing demand of the ceramic products in Uganda. Therefore, the ceramic tile industry is continuously working to acquire sustainable alternatives of the raw materials to replace the traditional triaxial materials.

Recycling of waste has been crucial in reducing their accumulation and also resource depletion (Ozturk et al., 2025). In view of rising environmental concerns, the ceramic tile sector is aggressively seeking alternate materials. An efficient and long-lasting method of reducing waste is to use industrial wastes as a raw ingredient in ceramic tile compositions (Almeida et al., 2021). Granite wastes (Gautam et al., 2021), shards of glass (Ezra, 2022), different slags (Piemonti et al., 2021), boron wastes (Karslıoğlu et al., 2022), various ashes (Odzijewicz et al., 2022), are some kinds of waste from industries that have been utilized for ceramic tile manufacturing.However, ferric oxide has not been given any attention.

The Acid Regeneration Plant (ARP) at Roofings Rolling Mills Limited, located in the Namanve Industrial and Business Park in Uganda, generates ferric oxide as a waste by-product from the pickling process. Since this ferric oxide is not used, it is disposed of in landfills, exposing risks to both human health and the environment. This is because iron particles can leach into the soil and eventually contaminate water that we consume, posing potential hazards to both humans and animals. Moreover, the expansion of galvanized steel production at Roofings Rolling Mills has led to a steady increase in ferric oxide output.

Consequently, annual disposal volumes rose to approximately 800 tonnes by 2022, significantly raising the company's disposal costs (Lindex, 2022). Despite this, there has been limited interest in utilizing ferric oxide in the development of ceramic tiles. Notably, ferric oxide possesses a chemical oxide (Fe_3O_2) that can act as a fluxing oxide in ceramic tiles. This study, therefore, explores the potential use of ferric oxide, sourced as industrial waste, in the manufacture of ceramic floor tiles.

1.2 Problem Statement

The ceramic industry is increasingly seeking alternative raw materials to replace traditional triaxial components, which are gradually depleting due to the growing demand for ceramic tiles. Ferric oxide is an industrial waste, which is dumped in landfills hence causing environmental pollution. This waste by-product from the steel industry, presents a promising alternative as it contains a fluxing oxide such as Fe_2O_3. This oxide when fired melts and vitrifies the final product hence improving on the flexural strength of the body. This study therefore explores the

potential use of ferric oxide in the manufacture of eco-friendly ceramic floor tiles.

1.3 Main Objective of the Study

To develop ceramic floor tiles using ferric oxide sourced as industrial waste from the steel industry.

1.3.1 Specific Objectives of the Study

The specific objectives of the study are to;

(i) Characterize the chemical composition and particle size distribution of raw materials used in the development of ceramic floor tiles.
(ii) Determine the physical and mechanical properties of the ceramic tiles produced from ferric oxide waste.
(iii) Optimize the physical and mechanical properties of ceramic tiles using design expert software.

1.4 Research Questions

The research questions of the study are;

1. How does the chemical composition and particle size distribution of various raw materials influence their suitability for ceramic floor tile production?
2. How does the addition of ferric oxide waste affect the physical and mechanical properties of ceramic flooring tiles?

3. What is the best formulation for maximizing the physical and mechanical properties of ceramic tiles using Design Expert software?

1.5 Significance

The United Nations Sustainable Development Goal (SDG) 12, emphasizes sustainable patterns of manufacture and consumption and is centered on the reuse of end-of-life materials as secondary resources and the sustainable management of industrial waste. This is in line with Uganda's Fourth National Development Plan (NDP IV) and Vision 2040, which both place a high priority on effective use of natural resources, sustainable development, and environmental preservation. Vision 2040 underscores the importance of green growth and the transition to a circular economy, while NDP IV highlights industrial waste reuse and innovation in resource efficiency as key strategies for inclusive and sustainable development. In this context, the development of ceramic floor tiles using ferric oxide waste from the steel industry provides a viable solution for reducing industrial waste, conserving raw materials, and fostering environmentally responsible manufacturing directly supporting Uganda’s national goals for sustainable industrial transformation and environmental sustainability.

1.6 Justification of the Study.

The rising demand for ceramic tiles in Uganda has increased the usage of natural raw resources such clays, feldspars, and sands, creating worries about resource depletion and environmental effect. At the same time, the steel industry particularly Roofings Rolling Mills Limited generates about 800 tonnes of ferric

oxide waste annually, which is currently landfilled, causing pollution and disposal costs. Ferric oxide (Fe_2O_3) has fluxing properties similar to feldspars, making it a potential alternative raw material in ceramic production. However, its use in Uganda's ceramic industry remains unexplored.

This study is therefore justified as it will:

- Scientifically evaluate the feasibility and performance of ferric oxide in ceramic formulations.
- Economically reduce production costs and dependence on imported raw materials.
- Environmentally minimize industrial waste and support circular economy practices.
- Strategically align with Uganda's Vision 2040, NDP IV, and UN SDG 12 on sustainable production.

In summary, the research offers a sustainable, cost-effective, and eco-friendly solution by valorizing ferric oxide waste for ceramic tile production, contributing to green industrial development in Uganda.

1.7 Scope of the Study

1.7.1 Content Scope

In this investigation, the mechanical properties of interest were flexural strength and compressive strength whereas the physical properties are linear shrinkage, water absorption, texture and color. These properties were assessed depending on the ASTM procedures of material testing. The chemical composition of the

raw resources was evaluated by means of XRF technique. Microstructure and phase analysis of the fired product were performed using SEM and XRD, respectively. Flexural strength, compressive strength, water absorption, and linear shrinkage were all optimized using design expert software.

1.7.2 Geographical Scope

The study involved using steel industrial waste in form of ferric oxide from Roofings Rolling Mills located at Namanve industrial park, Mukono district found in the central Uganda. Feldspar and kaolin were obtained from the Mutaaka deposits in Bushenyi district located in western Uganda. Sand was collected from lido beach on the shores of Lake Victoria in Wakiso district and ball clay was sourced from Ntaawo deposit in Mukono district found in central Uganda. The location of the raw materials was chosen based on the studies by Ochen et al., 2021 and Olupot et al., 2006 who ascertained the chemical composition and hence their suitability in the production of ceramic tiles.

CHAPTER TWO: LITERATURE REVIEW

2.1 Introduction

The parameters used in the development and analysis of the ceramic tiles are thoroughly summarized in this section. An evaluation of the literature is conducted on the impact of chemical compositions and particle size distribution on the mechanical qualities of the materials used to make ceramic tiles in general. The mechanical attributes, water absorption capacity, and fire temperatures are also examined.

2.2 Properties of Ceramic Materials

Ceramics are known as hard and scratch resistant materials and this makes them suitable for making cutting tools, abrasives, and wear-resistant applications. They are also known to withstand high temperatures of 1600 – 2000 °C without melting or deforming which makes them useful in refractory applications (Abdullah et al., 2024). They exhibit high flexural and compressive Strengths and are resistant to corrosion, oxidation, and chemical attacks, making them ideal for chemical processing equipment.

Many ceramics are light in weight, which is advantageous in aerospace industry and structural applications. Ceramics are excellent electrical insulators, used in electronic and electrical applications. Some ceramics have low thermal conductivity, making them good insulators, while others can conduct heat effectively (Kurian & Thankachan, 2023). Despite their hardness, ceramics are brittle and can fracture or shatter under impact or tensile stress.

Most of these ceramic materials properties arise because of firing that produce dense heterogeneous structure. For ceramic materials to be used as porcelain tiles, flexural strength is the most important property with a value greater than 35 MPa (Ochen et al., 2021).

2.3 Chemical Composition of Ceramic Raw Materials

According to Elakhame et al., (2016), ceramic tiles are non-metallic inorganic solid materials developed from triaxial materials such as feldspar, quartz, clay, sand, which are all good sources of silica and alumina. In the development of ceramic tiles, composition and the conditions of treatment of the body affects and determines the transformation of the raw materials (Khalil et al., 2024). The manufacture and formulation of the ceramic tiles is typically based on raw materials and production processes.

Mineral oxides extracted from natural minerals, silica like quartz, and mineral silicates like clays of various compositions constitute ceramics. The most prevalent clays are based on the mineral kaoliniten ($Al_2Si_2O_5\,(OH)_4$), which is composed of tiny particles of hydrous aluminum silicate. These secondary geological deposits are created when igneous rocks weather due to the action of organic acids, dissolved carbon dioxide, and water. Feldspars are alumino silicates that contain sodium (Na), potassium (K), and calcium. They vary in composition from Albite ($NaAlSi_3O_8$) with a firing range between 1100−1200 °C and Othorclase ($KAlSi_3O_8$) with a higher firing range from 1150 -1400°C to Anorthite ($CaAl_2Si_2O_8$) with a narrow firing range (from 1200 to 1300 °C) (Olupot, 2006). Quartz (SiO_2) whose main source is sandstone is relatively high in the ceramic products, both in Free State and in combined form as clay.

Advanced ceramic materials consist of various compounds, including silicon carbide, silicon nitride (Si_3N_4), steatite (magnesium silicates), titanium carbide, uranium oxide (UO_2), yttrium barium copper oxide ($YBa_2Cu_3O_7-x$), zinc oxide (ZnO), and zirconium dioxide (zirconia) (Zawrah et al., 2024). The chemical composition of ceramic materials determines its application and composition can be analyzed by employing different methods such as XRF, SEM and XRD.

2.4 Characterization of Raw Materials

2.4.1 Characterization of Sand

Sand plays an important role in formulation of ceramic products. Sand acts as a filler material that helps to shape and form ceramic bodies, providing a bulk structure. As a fluxing agent, it serves to reduce the melting point and vetrify the mixture during sintering.

Sand can also influence the texture and surface finish of the final ceramic product, contributing to its aesthetic qualities.

Several studies have been conducted to quantify sand particle properties such form, size, spatial coordinates, and orientation (Cox & Budhu, 2008). The spatial arrangement of sand particles is shown in 98Figure 2.1. Osman, 2021 used the XRD technique to analyze the chemical composition of sand and results showed that sand is comprised of major oxides as.19% - SiO_2, 0.57% - Al_2O_3, 0.08% - Fe_2O_3, 0.10% - CaO, 0.08 - % MgO, 0.06% - Na_2O, 0.01% - K_2O, 0.03% - P_2O_5, 0.13% - SO_3, 0.04% - Cl and 0.3% - Loss on ignition (LOI). Sand with such a high percentage of silica content is categorized as high-grade silica sand (Nigussie et al., 2023).

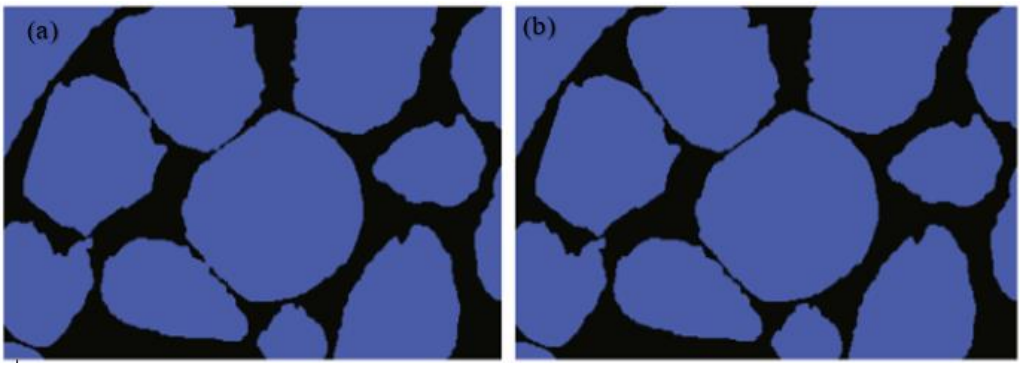

Figure 2. 1: Shows binary image of sand particles (a) with intact contact points and (b) with separated particles (Druckrey et al., 2016).

2.4.2 Characterization of Ball Clay

Ball clay has smaller crystal sizes than other types of clay and is a fine-grained material mostly made of the mineral kaolinite (Bauluz et al., 2021). Physically and chemically worn rocks, such as orthoclase, which is present in granite and combine with the atmospheric CO_2 and H_2O to generate clays as follows; see equation 2.1(Zhao et al., 2017).

$$K_2O.Al_2O_3.6SiO_2 + 2H_2O + CO_2 \rightarrow Al_2O_3.2SiO_2.2H_2O + 4SiO_2 + K_2CO_3 \quad (2.1)$$

Ball clay is made up of kaolinite (20-80%), mica (10-25%), and quartz (6-65%) (Dhivya & Keshav, 2022). Mullite ($3Al_2O_3 \cdot 2SiO_2$) is a key crystalline phase obtained in ceramic mixes as a as a consequence of the chemical interaction between alumina (Al_2O_3) and silica (SiO_2) within clay minerals. This reaction is essential to the service life and durability of the ceramic product. Ball clay has a high plasticity and strength due to its small particle size; the presence of these minerals affects the final characteristics and firing behaviour of the final body. During sintering, the clay minerals and other oxides melt, forming a viscous glassy phase that binds the crystalline phases together (Altimari et al., 2024).

2.4.3 Characterization of Ferric Oxide

Ferric oxide is an inorganic compound, commonly known as iron (iii) oxide (Fe_2O_3) (Aronniemi et al., 2004). Ferric oxide (Fe_2O_3) in a ceramic mix can react with other oxides, particularly during firing, to form new compounds and alter the ceramic's properties. It can act as a flux, a colorant, and can also interact with other oxides to influence color and the formation of crystalline phases (ZHOU et al., 2016). The reaction of Ferric oxide with silica (SiO_2) forms a glassy phase and a crystalline phase like mullite. It can also react with alumina (Al_2O_3) to form hercynite ($FeAl_2O_4$), which can further react with silica to form mullite ($3Al_2O_3 \cdot 2SiO_2$). The chemical reaction requires higher firing temperatures of above 1000^oC to form mullite while low temperatures result into the formation of ferrous oxide.

Muthukumar et al., (2024) characterized iron oxide nanoparticles and an XRD analysis of the particles showed that the crystalline phase structure of the produced particles is shown by diffraction peaks. Janjaroen et al., (2018) studied the chemical composition of ferric oxide and results showed that ferric oxide comprised of mainly Fe_2O_3 with a percentage weight of 96.08% and followed by SiO_2 with 2.7%. Other compounds such as CuO and SO_3 were present but in very small quantities.

2.4.4 Characterization of Kaolin

Kaolin exists as a rock material rich in kaolinite ($Al_2Si_2O_5(OH)_4$) which is a hydrous alumino silicate mineral usually found in soils, sedimentary rocks (Dewi et al., 2018). Kaolin contains Al_2O_3, which reacts with other oxides

present in the composition at a temperature above 1100 ºC to form mullite with a chemical composition of $Al_6Si_2O_{13}$. According to Bouzerara et al., (2009), kaolin exhibits properties such as opacity, electrical, and mechanical properties and is a versatile mineral that finds its application in ceramic and glass industry due to its distinct chemical and physical characteristics. Zewdie et al., (2021) carried used XRF technique to analyze the chemical composition of raw kaolin and results showed that SiO_2 was the most dominant metal oxide present with a weight percentage of 59.2%. The author further found that the presence of iron oxide as an impurity caused the raw kaolin clay to appear to be white with brownish red, yellow, and black colour impurities. Separate studies revealed similar findings by Buyondo et al., (2024) and Morsy et al., (2014) who reported other metal oxides such as Na_2O, K_2O, MgO, Fe_2O_3, CaO, TiO and P_2O_5 that were discovered, however in exceptionally small amounts.The low content of Fe_2O_3 in kaolin makes it suitable for white wares and fabrication of electro-porcelain ceramics (Yaya et al., 2017). On the other hand, Ayalew & Demir, (2023) examined surface morphology of raw kaolin using a scanning electron microscope (SEM). The SEM image revealed that raw kaolin had an uneven form, a rough age, and an agglomerated surface throughout, as seen in Figure 2.2.

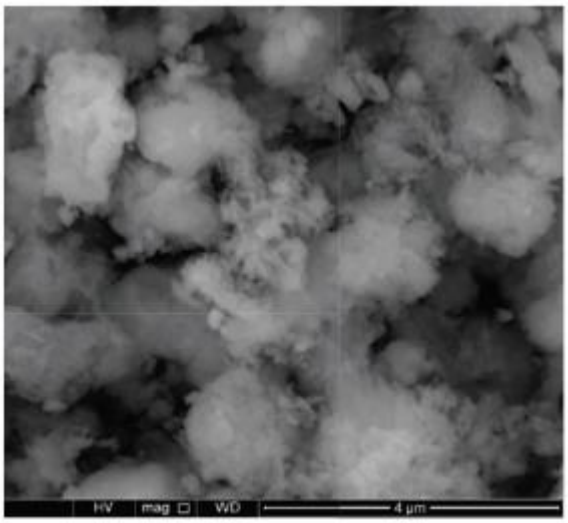

Figure 2. 2 :Shows SEM image of raw kaolin (Ayalew & Demir, 2023).

2.4.5 Characterization of Feldspar

Feldspars are used in ceramic mixes and the reaction takes place in different ways depending on their composition (potassium, sodium, or calcium-rich) and the specific ceramic mix. They primarily act as fluxes, lowering the melting point and promoting verification. For feldspar, the standard chemical equation is $xAl(Al,Si)_3O_8$, where x can be Na, Ca, or K. Specific examples of feldspar include albite ($NaAlSi_3O_8$), orthoclase/microcline ($KAlSi_3O_8$), and Anorthite ($CaAl_2Si_2O_8$) (Olupot et al., 2006). Feldspars are crucial for reducing the firing temperature of ceramics. They melt and react with other materials in the mix, forming a glassy phase that bonds the particles together (Taib, 2020). Feldspars contribute to the overall chemical composition of the ceramic mix by providing alumina (Al_2O_3) and silica (SiO_2). These are essential components for the formation of a stable ceramic body (Taib, 2020). Feldspar appears in three forms of Albite ($NaAlSi_3O_8$), Orthoclase/Microcline ($KAlSi_3O_8$) and Anorthite ($CaAl_2Si_2O_8$) as shown in Figure 2.3, which is less commonly used in ceramics due to its narrow firing range (Gorelova, 2023).

.

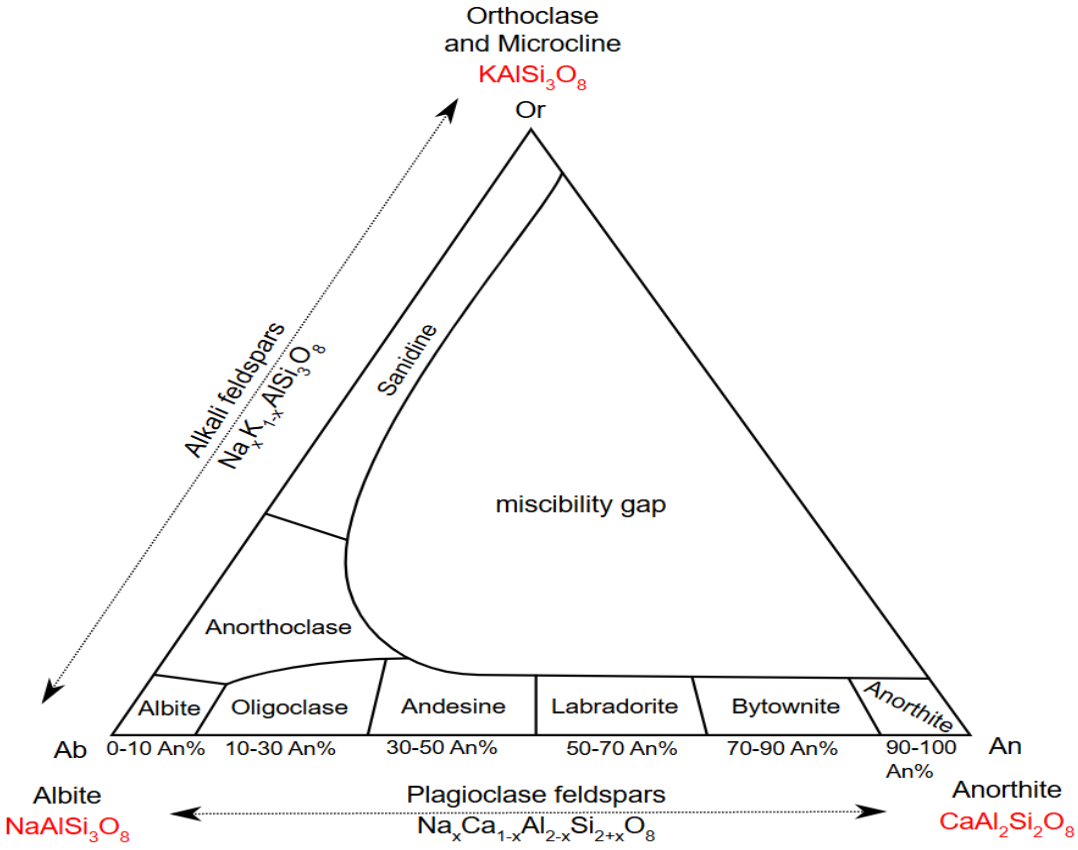

Figure 2. 3:Compositional phase diagram of the different minerals that constitute feldspar solid solution (Gorelova, 2023).

Fatile et al., (2014) carried out a chemical analysis on three different samples of feldspar from different locations. The results showed that SiO_2, Al_2O_3, and K_2O_3 were the major compounds present in the feldspar with percentage weights ranging from 65.6 % - 66.5 %, 13.8 % - 18.1 %, and 9.0 % - 11.0 % respectively. In a different research study, Aliyu et al., (2016) carried out a characterization of feldspar and results showed that feldspar constituted 67.3 % of SiO_2, 17.5 % of Al_2O_3, and 11.3 % of K_2O as the major compounds present. Similar results were obtained in separate characterizations carried out by (Boulos et al., 2015) and (Aljaradin & Amareh, 2015), as shown in Table 2.1.

Table 2. 1: Chemical composition of feldspar samples (Boulos et al., 2015).

Constituent	Sample I %	Sample II %
Total SiO_2	72.37	73.50
Al_2O_3	11.97	12.50
Fe_2O_3	0.53	0.22
Na_2O	2.28	2.13
K_2O	8.38	9.30
MgO	0.25	0.23

2.5 Particle Size Distribution and Its Effect on Mechanical Properties

Particle sizes are important in porcelain tile since they define the product's most prevalent crystalline phase (C. L. Alves et al., 2024). Additionally, it was shown that the average coefficient of linear thermal expansion of quartz in the tile matrix and the c-lattice parameter were consistent (Leide et al,2019). This behavior shows the process of quartz thermal expansion.

According to research by Ochen et al. (2019) on porcelain tiles created from Ugandan raw materials, quartz's anisotropic nature promotes particle dispersion from the matrix under conditions where quartz particle diameter directly impacts flexural strength and sintering behaviour. Tiles with fine quartz particles (<45 µm) indicated higher FS (33 MPa) and lower WA (0.47 %) compared to those with coarse particles (>45 µm), which showed 8 MPa strength and 7.1 % water absorption. The improved properties are attributed to finer particles promoting better densification and forming smaller, isolated pores, whereas coarser particles lead to larger, interconnected pores that act as crack propagators

A study by Aydın et al., (2021) explored how granule size distribution affects mould filling and the resulting mechanical properties of wall tiles. By adjusting, spray dryer parameters to reduce granule sizes to between 75–500 μm, they achieved better mould filling. This led to tiles with higher strength and improved technical characteristics, demonstrating that optimizing granule size distribution enhances tile quality.

The interaction between grain size and mechanical properties in ceramics follows Hall–Petch relation, where decreasing grain size increases tensile strength. However, fracture toughness tends to increase with larger grain sizes due to the rougher fracture surfaces impeding crack propagation. Hardness generally increases with decreasing grain size, provided the ceramics are densified to similar levels.

In 3D-printed ceramic scaffolds, bimodal granule blends (combinations of large and small particles) have shown to enhance mechanical strength compared to unimodal distributions. Despite higher porosity, the optimized packing density achieved with bimodal distributions results in stronger structures, highlighting the importance of tailored PSD in ceramic applications.

The particle size of glaze slurries also affects the final properties of ceramic tiles. Studies have demonstrated that decreasing the average particle size of glaze particles through extended milling times leads to increased whiteness index and glossiness. This is due to a higher number of crystals forming in the glaze structure, which enhances its optical properties.

Optimizing particle size and distribution is crucial in ceramic tile manufacturing to enhance mechanical properties and overall quality. Fine particles improve densification and strength, while controlled PSD ensures better mold filling and surface characteristics.

2.6 Firing of Ceramic Green Body

Firing transforms a ceramic green body into a durable, fired ceramic by sintering the particles, often with the help of a glass phase, and removing organic components (Park et al., 2024). This process, which involves a green body containing organic or inorganic additives. Firing occurs in a kiln or a furnace, which accommodates high temperatures and creates a strong, vitrified ceramic product. Firing initiates sintering, where the ceramic particles fuse together through atomic movement and chemical bonding (Fujishiro et al., 2025).

Certain ceramics have components that, when heated, turn into a glass phase. Vitrification is the process by which this glass phase liquefies and fills in the gaps between the particles after firing. The heat treatment process known as vitrification causes the inorganic components of the material to convert into the glass structure while the organic components dissolve down (Iwaszko et al., 2024).

Typical ceramic firing often involves two stages such as bisque firing or first firing and glaze firing. Bisque firing burns out organic components, while glaze firing applies a glass coating for decoration and functionality (C. Liu et al., 2025).

As stated by Furszyfer Del Rio et al., (2022), the sintering temperatures of ceramic bodies usually ranges from 800 ºC and 2500 ºC for about 1 hour to 2 hours. However, studies have shown that using feldspar in the development of ceramic products reduces the sintering temperature in addition to improving their mechanical properties (Vasić et al., 2022). The results revealed that green body samples sintered at 950 ºC produced better properties and was considered as the optimum sintering temperature for that application.

2.7 Water Absorption Capacity of Ceramic Tiles

The capacity of ceramic tiles to absorb water is a crucial physical feature for evaluating their quality (Yibing, 2020). Ceramic formulations are either found in liquid or powder form and therefore are typically combined with water. The permeability characteristic of ceramic proportions determines how well sample particles suspend in water. The dispersion of particles on ceramic wares during the application stage and during vitrification is measured by the absorption coefficient of particles in water (Yakubu, 2025). The relationship between ceramic tile wet and dry mass allows water absorption to be calculated using the Equation 2.2.

$$\text{WA}\ (\%) = \left(\frac{\text{Ww}-\text{Wd}}{\text{Wd}}\right) \text{x}100\ \%, \qquad (2.2)$$

where Ww is mass of the tile after being immersed in water and Wd is the mass of the tile in dry condition.

Standard ISO 10545-3 defines two test methods; by boiling and by using vacuum. ASTM C 373-14 method of the determination of tile water absorption, which also uses the boiling method requires longer tile soaking times in boiling

and cooling (5 hours and 24 hours, respectively) than the method described in standard ISO 10545-3 (Menegazzo et al., 2022).

Due to the tinny particle diameters produced during the grinding and high-pressure pressing processes, glazed porcelain ceramic tiles exhibit water absorption capabilities far below 0.5% (Vieira et al., 2017). Ghosh et al., (2002) made a ceramic tile utilizing blast furnace slag and ordinary clay. The findings indicated that the fired samples had a water absorption capacity in a range of 2.5 -0.1%.

Furthermore, Guo et al., (2024) developed a solar-fired ceramic cup fired using a solar ceramic kiln and results revealed that the cup's surface was free of cracks and had a WA capacity of 4.25 % and with an open porosity of 9.93 %. According to Dutra et al., (2008), a high content of potassium oxide in the ceramic body can lower water absorption capacity.

2.8 Linear Shrinkage Capacity

The linear shrinkage parameter can be utilized to adjust the size of the sintered ceramic tiles (Jayaweera et al., 2024). Therefore, it is a property that measures how much the tiles shrink. In the ceramic industry, shrinkage is important because modifying the shrinkage during the firing process can negatively impact the fired ceramic tile's mechanical and physical characteristics (Jayaweera et al., 2024). Experimental kinetic models for the shrinkage behaviour of various ceramic materials at varying firing temperatures have been the subject of numerous research studies (Jayaweera et al., 2024).

Using a kinetic model-based approach using computational fluid dynamics (CFD), Bayer Ozturk et al. (2024) examined how the shrinkage of porcelain tiles changed during the firing process and found that the linear shrinkage was greater than 5%. The ISO 13006 standard for ceramic tiles was used to assess the linear shrinkage of sintered ceramic tiles (SL).

Equation 2.3 was used to calculate the linear shrinkage of sintered ceramic tiles (SL), where L_i represented the starting lengths of the ceramic tile sample prior to firing and L_F represented the final lengths of the ceramic tile sample following firing.

$$SL = \frac{Li - LF}{Li} x100\%. \quad (2.3)$$

Patrick et al., (2015) carried out a shrinkage test on the tile samples developed and the study results showed that the developed tiles had a shrinkage higher by 3 % compared to the recommended shrinkage for stoneware made through plastic deforming. However, the authors discovered that the fired samples had slightly lower shrinkages and concluded that acceptable shrinkages would be achieved through dry pressing instead of plastic forming.

2.9 Mechanical Properties of Ceramic Tiles

Ceramic materials have gained increased interest for industrial applications since they exhibit excellent chemical, thermal, mechanical stability, long life time and good defouling property (Benito et al., 2005). Because of their color, textures, and designs, ceramic tiles are used in very many industries like the construction industry. The mechanical characteristics of ceramic tiles are one of several elements that affect their durability. Excellent mechanical qualities including

hardness, wear, flexural strength, toughness, and so forth are achieved by the fabrication of advanced ceramic materials. Ball clay, one of the raw ingredients used to make ceramic materials, enhances mechanical strength and aids in shaping by offering plasticity (Iqbal & Lee, 2000).

2.9.1 Flexural Strength

Flexural strength is a mechanical property exhibited by ceramic tiles such that they resist bending in presence of an external force. The major component in the ceramic body, kaolinite, crystallizes into mullite when fired at temperatures higher than 1100 ^{o}C, which is considered to improve the flexural strength of ceramic product (Stathis et al., 2004). Iqbal & Lee, (2000) developed ceramic tiles from local raw materials sourced in Uganda and the results showed that firing temperatures of 1200 ^{o}C increased mullite population.

The maximum flexural strength reported was 33 MPa for tile samples containing 30-40% kaolin, 30-40% feldspar, 20% clay, and 10% sand. According to Ochen et al., (2019), the ceramic body reduces pyroplastic effects during sintering due to quartz but has a negative impact on the flexural strength of tiles.

In similar study by (Stathis et al., 2004), a 20-30 % increase in the bending strength of tiles when the quartz grain size is controlled in the optimum ranges of 5-20 micrometers was reported.

2.9.2 Compressive Strength

This is a parameter that shows how resistant a material is to being crushed under stresses (Fragassa, 2015). As a result, its assessment is of major significance to

the materials used in the building sector since the material must be able to sustain significant loads.

Patrick et al., (2015), studied the physical properties of tiles produced from clay blended with feldspar, quartz, and filler. The authors reported that the developed tile samples exhibited a maximum compressive strength of 482 kg/cm^2. In another study conducted by Prahara & Meilani, (2014), The size of the coarse aggregate utilized during the mixing and development of the tiles has an impact on the products' strength, based on the research authors. According to reports, the compressive strength dropped as aggregate size increased. Liu et al., (2020), made a black ceramic tile out of residual slag. The results demonstrated that the compressive strength was 58.58 MPa at optimal firing temperatures of 1150 ^{o}C, exceeding the Chinese national code for compressive strength of 27 MPa for polished tiles.

2.10 Optimization of Ceramic Raw Materials

Raw materials are susceptible to changes in processing for industrial production of ceramic tiles. During the manufacturing stages, tests are frequently used to quantify the modulus of rupture, linear firing shrinkage, and water absorption as quality and process control metrics (Silveira et al., 2010). Since the mixture of raw material determines the mechanical and physical properties under constant processing conditions, the optimization methods specific to mixture experiment design can be used to model them.

Mixed experiment design is a unique example of the response surface technique employing statistical and mathematical tools, which have significant applications in the creation of new products as well as the enhancement of present designs.

The underlying concept is that a mixture's response is determined by the proportions of its constituent parts, or fractions, rather than by the mixture's overall amount The initial step is to decide which mixes are suitable for evaluating the response surface. Once this is known, any mixture's property value can be estimated using changes in the ratios of its constituent components (Zawada et al., 2021). The response quantity and the influencing variables have a functional relationship that can be quantitatively described by statistical methods, among other methods. A statistical model is developed to show the correlations between influencing factors and goal variables in a reasonably accurate manner, depending on the quality of the modification A statistical model is developed to show the correlations between transformation factors and goal variables to accurately illustrate the relationship and the quality of the modification (Li et al., 2013).

2.11 Summary of Literature Review

The creation and characterization of ceramic tiles were the main topics of the examined literature, with an emphasis on the impact of firing conditions, particle size distribution, raw material composition, and the consequent mechanical properties on tile performance.

Ceramic materials provide exceptional hardness, wear resistance, high-temperature stability (up to 2000 °C), and chemical inertness. However, their brittleness remains a major disadvantage.

For applications using porcelain tiles, flexural strength (>35 MPa) is very important. Chemical composition of raw materials: Sand, quartz, feldspar, and clay make up the majority of ceramic bodies, which are sources of silica and alumina. Phase formation and colour are altered by additives such as ferric oxide. The final mechanical behaviour, densification, and vitrification process are all significantly influenced by the proportions and mineralogical composition.

2.12 Research Gaps

Insufficient research on locally accessible raw materials Comprehensive compositional and performance optimization using local raw materials is still lacking, despite some research (Ochen et al., 2019; Iqbal & Lee, 2000) examining Ugandan sources. Absence of comprehensive research relating PSD, chemical makeup, and firing conditions Few models predict combined impacts on densification, strength, and porosity; the majority of research examines these factors separately. Insufficient optimization models for the links between composition and properties.

There is a need for localized prediction models that are suited to particular raw material properties and firing regimes, while current statistical models mostly focus on industrial formulations.

Limited experimental validation of alternative fluxing agents or additives:

In order to increase sustainability and lower costs, few studies investigate substituting industrial or agricultural wastes for conventional feldspar or quartz. Inadequate research on microstructural correlations There is little research linking microstructural evolution (such as mullite production and glass phase distribution) with mechanical behavior under different sintering profiles, despite the fact that XRF, XRD, and SEM are employed for characterisation. Standardization and comparative gaps with global benchmarks: Performance benchmarking is challenging since many studies report mechanical parameters but do not directly compare them to ISO/ASTM requirements for porcelain tiles.

CHAPTER THREE: MATERIALS AND METHODS

3.1 Introduction

This section outlines the materials and methodologies employed in the development of ceramic tiles. It details the formulation process, experimental procedures, and the characterization of raw materials, including their collection and preparation. The physical and mechanical parameters of the finished products are also discussed. Additionally, it also includes the optimization process aimed at determining the most effective mixing proportions to achieve optimal tile properties, using design expert software.

3.2 Research Design

This was based on experimental and simulation approach. The experiment involved mixing various proportions of the raw materials to create a slurry, which was pressed to produce ceramic tiles. Both the physical and mechanical properties of the tiles were tested. These properties are dependent variables of the study whereas the independent variables included composition of ferric oxide in the samples. Simulation was initiated using design expert software. In this case, the mixing ratios were optimized, and the outcomes were compared with the experimental data.

3.3 Collecting of Raw Materials

Raw minerals were obtained from reserves situated in various locations of Uganda as shown in Figure 3.1 (b). Feldspar and kaolin were sourced from Mutaaka deposit located on Latitude: 0° 31' 59.99" N and Longitude; 30° 10'

60.00" E. This deposit is found in western Uganda and it is about 340 km from Kampala city. Sand was sourced from lido beach on the shores of L.Victoria located on Latitude: 0° 02' 24.00" N and Longitude; 32° 27' 34.19" E. Ball clay was sourced from Ntaawo deposit located at Latitude; 0° 14' 60.00" N Longitude; 32° 54' 59.99" E in central Uganda, Mukono district which is about 20 km from Kampala capital city. Roofing Rolling Mills located in Namanve industrial park at Latitude 0°20'31" N and Longitude 32°42'1"E about 15 km from Kampala city provided the industrial steel waste in the form of ferric oxide. The X-ray fluorescence (XRF) method was used to examine the chemical constituents of these raw materials. Additionally; the hydrometer method was applied to determine the raw material particle size distribution. This was done to assess the quality of the raw materials used in the study

..

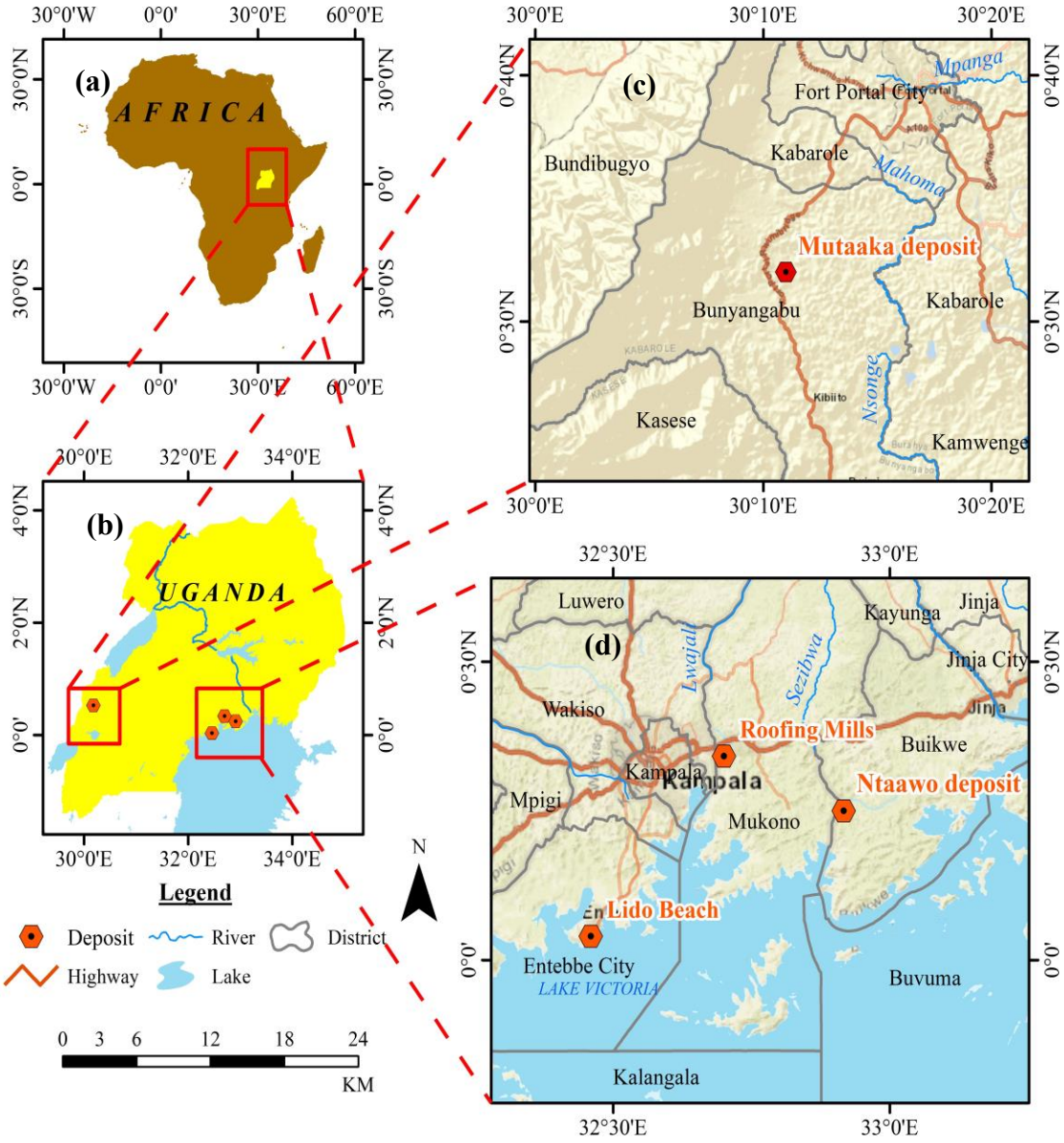

Figure 3. 1: (a) Map of Africa showing the location of Uganda, (b) Map of Uganda showing the location of deposits, (c) Map of western Uganda showing the Mutaaka deposit and (d) Map of Central Uganda showing the location of Ntaawo deposit, lido beach and roofing mills.

3.4 Processing of Raw Materials

3.4.1 Sand

Sand was mined in its original state as shown in Figure 3.2 (a). It was sieved through a 300 µm mesh to eliminate contaminants such as shells and stones. It was then cleaned using water and then wet milled using a ball mill containing lake stones as a grinding medium. The average diameter of the lake stones was 30 millimeters and the ball mill was operating at 50 rev/min. The time taken for complete milling was 40 hours. Wet milling was considered effective than dry milling since it tampers the particles size thus resulting in finer powder. The milled sand was then oven dried at 110 ^{o}C for 12 hrs. Following drying, the ground powder was filtered by a 50 µm mesh screen to create a fine powder, as seen in Figure 3.2 (b).

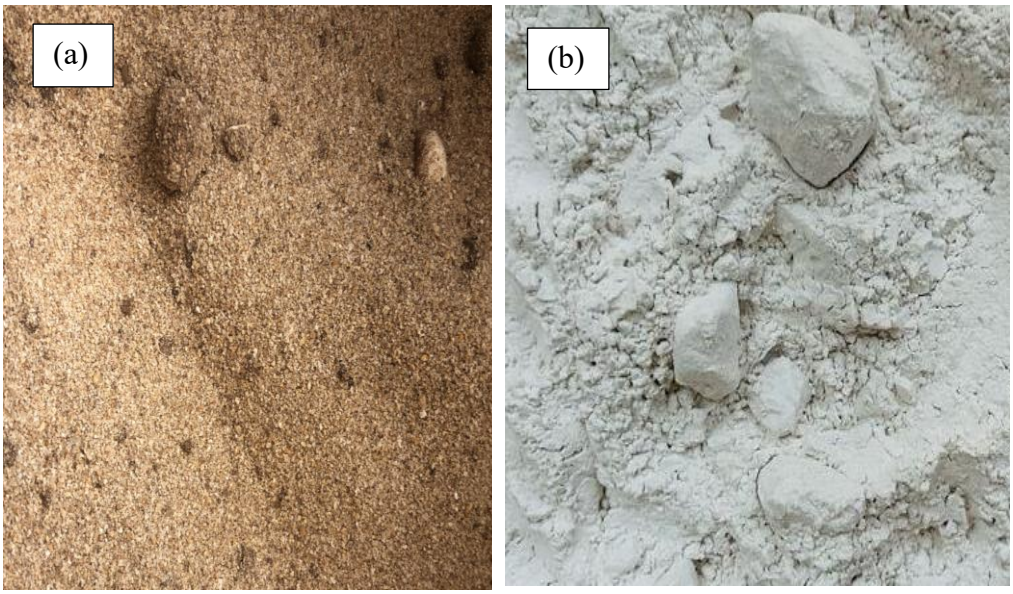

Figure 3. 2: (a) Raw sand before processing and (b) Fine sand powder after processing.

3.4.2 Ball Clay

Ball clay was sourced in its raw form and left to dry under direct sunlight (see Figure 3.3 a). It contained impurities such as quartz, stones, roots, and metals, which were manually removed by hand. The dried clay was ground in a ball mill using lake stones, which had an average diameter of 50 mm. The clay powder was then sieved through a 40 µm mesh to produce a fine powder, as shown in Figure 3.3 (b).

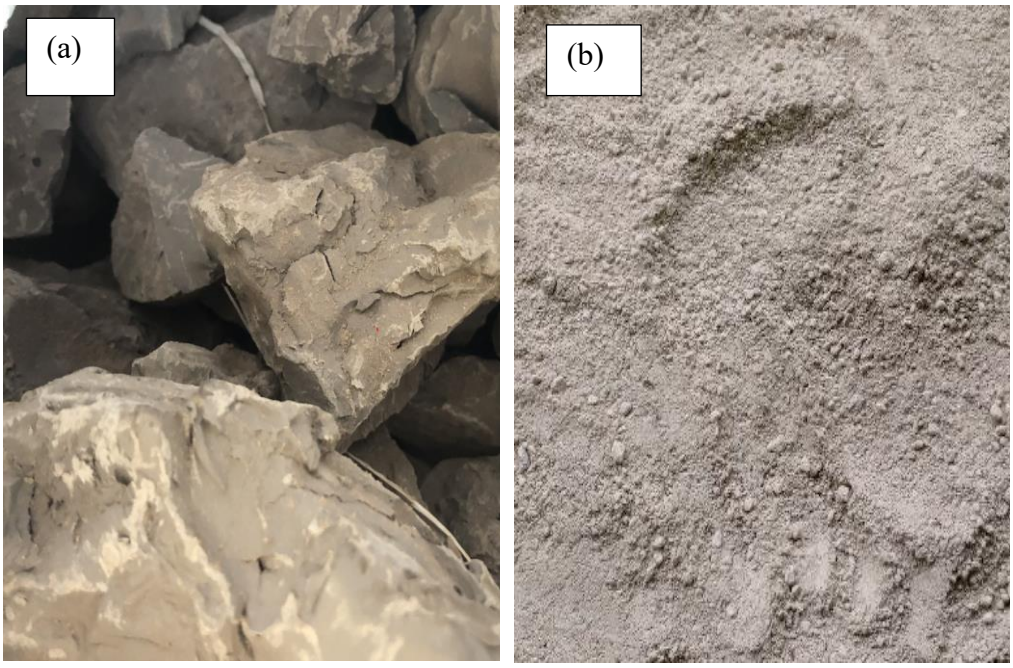

Figure 3. 3: (a) Ball clay after sun drying (b) Processed clay powder.

3.4.3 Kaolin

Kaolin was dried using the sunlight for two days and thereafter, to get rid of impurities, a 300 µm sieve was used. Kaolin was then milled and later sieved using 53 µm mesh size to obtain fine powder as shown in Figure 3.4.

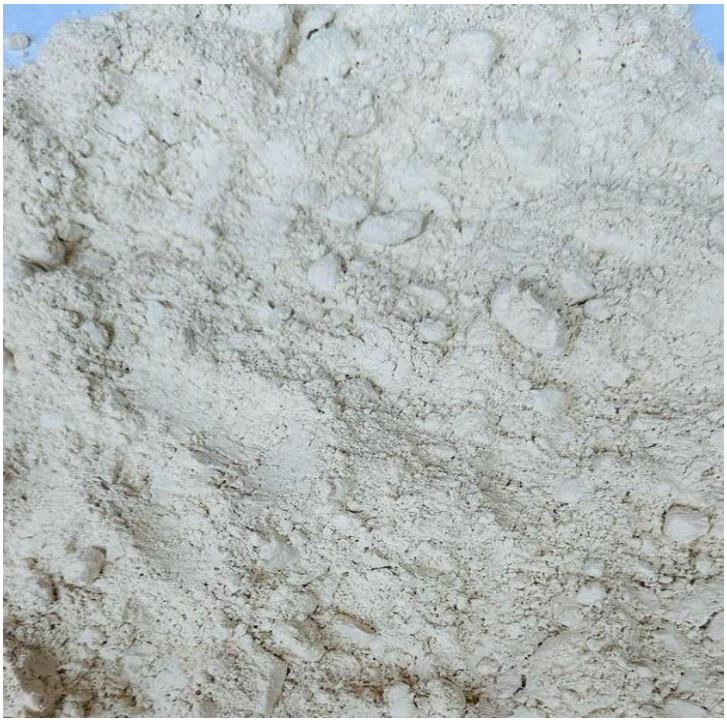

Figure 3. 4: Processed kaolin after milling.

3.4.4 Feldspar

Feldspar from Mutaaka deposits was mined using forked hoes. The mined raw material contained various impurities, such as soils, which were manually removed by hand. As seen in Figure 3.5 (a), it was further cleaned with water to get rid of dirt and other surface impurities. It was cleaned, then dried in the sun after being ground for 72 hours at 50 rpm in a ball mill. As shown in Figure 3.5 (b), the dry material was subsequently sieved through a 53 μm mesh to produce a fine powder.

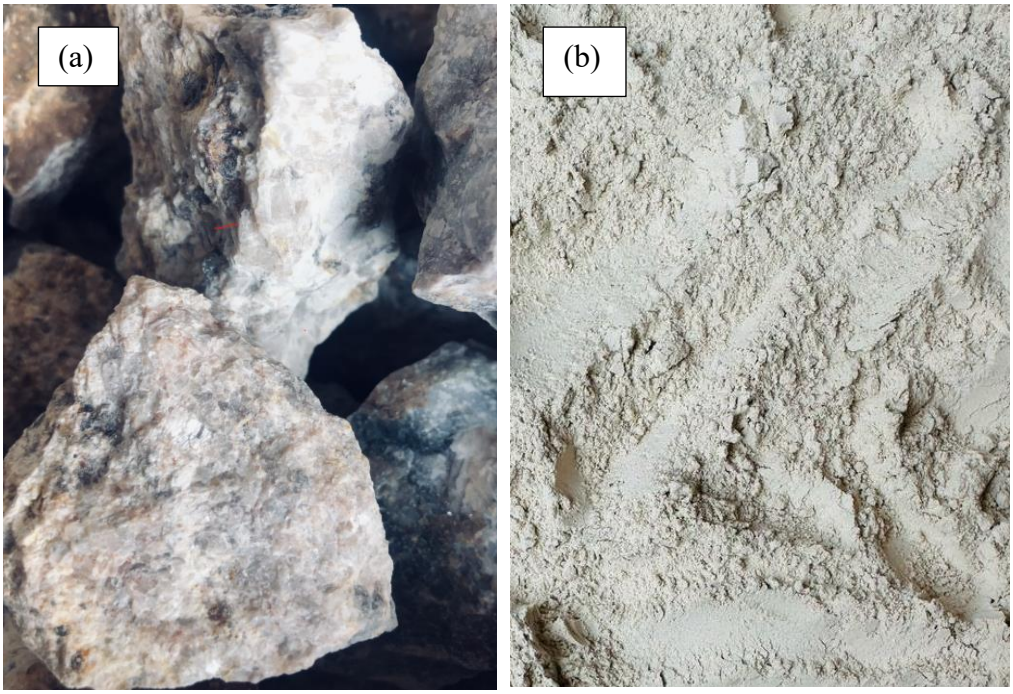

Figure 3. 5: (a) Un processed feldspar and (b) fine powdered feldspar.

3.4.5 Ferric Oxide

The ferric oxide shown in Figure 3.6 was sieved by a 53 µm mesh sieve. The sieve size used was selected based on the particle sizes of feldspar used in the study since they were used interchangeably in terms of weight percentages (wt %) in the mixing ratios. The sieve sizes used in the study were also chosen in accordance with prior research that reported that particle sizes in a range of 10-150 µm results in improved quality since finer particles can vitrify easily hence enhancing the mechanical properties of the fired product (Atidi et al., 2023).

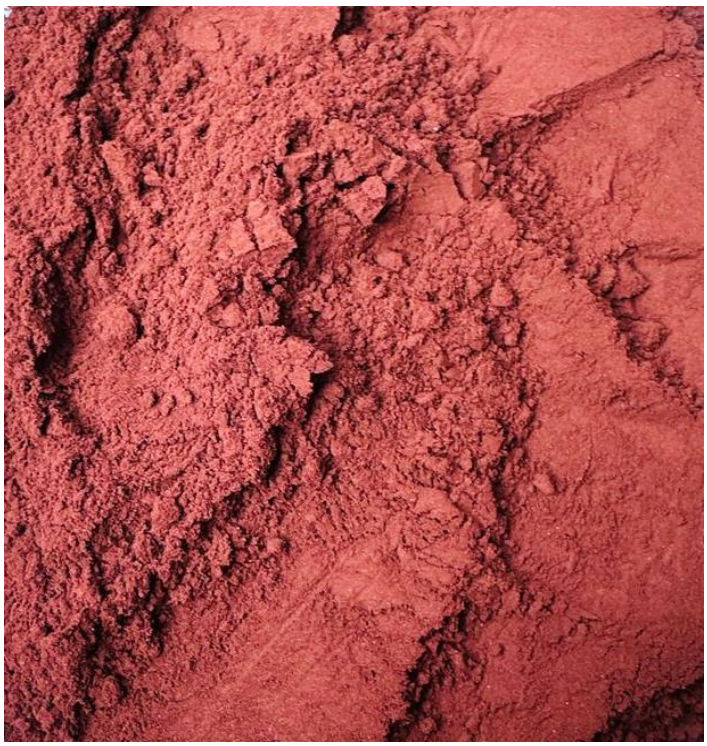

Figure 3. 6: Processed ferric oxide used in the study.

3.5 Characterization of the Raw Materials

3.5.1 Chemical Composition Analysis

The X-ray fluorescence (XRF) method was used in the chemical composition analysis to ascertain the elemental content of the raw materials. Pulverized samples were combined with lithium bromide in a gold-platinum mold and burned at 750 ^{o}C with oxygen and liquid petroleum gas (LPG) on an XRF bead maker. After cooling down naturally, the burned sample was collected and taken to the XRF cassette for examination using various material calibrations.

X-ray fluorescence device uses the detection method based on fluorescent X-rays to identify components present in a sample. The sample is exposed to high

energy X-rays from the XRF machine and these rays interact with the sample's atoms causing atoms to move out of their inner-shell electrons. The atom becomes unstable when an electron from its inner shell moves out. An electron with a higher energy level fills the vacancy to restore stability. The energy released in this transition is converted into X-rays and this is unique for each element.

Since each element emits X-rays at a different energy level, the XRF device identifies and measures the elements in the sample by detecting the X-rays that are released. Chapter 4, Section 4.2, presents the findings of the elemental composition of the raw materials employed in this investigation.

3.5.2 Particle Size Analysis

Particle size analysis of the raw materials was carried out using the hydrometer method, which involves sedimentation of the sample. Classification was based on particle diameter, aligning with defined particle size ranges. This method is suitable for particles smaller than 2 mm and operates based on Stokes' Law, where fine clay particles (less than 0.002 mm) remain suspended, while heavier particles like quartz (0.05–2 mm) settle at the bottom. Particle size distribution was determined by analyzing the difference between initial and final hydrometer readings, with the total composition normalized to 100 %.

3.6 Formulation of the Samples

3.6.1 Mixing of the Raw Materials

The proportions listed in Table 3.1 were used to mix the processed raw components. Homogenization of the mix proportions was done for 1 hour using a ball mill as shown in Figure 3.7 running at 50 rpm. The ball mill contained lake stones of average diameter of 30 mm as a mixing medium. After adding 12 wt % moisture, the mixture was further homogenized for 10 minutes to ensure that the moisture was uniformly absorbed by particles throughout the mixture. This was done in order to prevent the formation of dry spots or overly wet areas, which could affect compaction and drying behavior of the green body. The mixing proportions shown in Table 3.1 were chosen based on a study by Ochen et al., 2021,who reported that these proportions are known to give properties that are recommended by ISO 13006 for porcelain tiles (Ochen et al., 2021). As seen in Table 3.1, mixing ratios of sand, ball clay, and kaolin were kept constant, while the proportions of feldspar and ferric oxide were varied to evaluate the effect of ferric oxide on the properties of the ceramic tiles. Both ferric oxide and feldspar are considered as fluxing agents in this study. Composition with 30 wt % feldspar, 0 wt % ferric oxide, 20 wt % ball clay, 40 wt % kaolin and 10 wt % sand was considered as control sample.

Table 3.1: Mixing ratios of raw materials.

Raw materials	**Composition of the body (wt %)**				
	1	2	3	4	5
Feldspar	30	20	15	10	0
Ferric oxide	0	10	15	20	30
Ball clay	20	20	20	20	20
Kaolin	40	40	40	40	40
Sand	10	10	10	10	10
Total	**100**	**100**	**100**	**100**	**100**

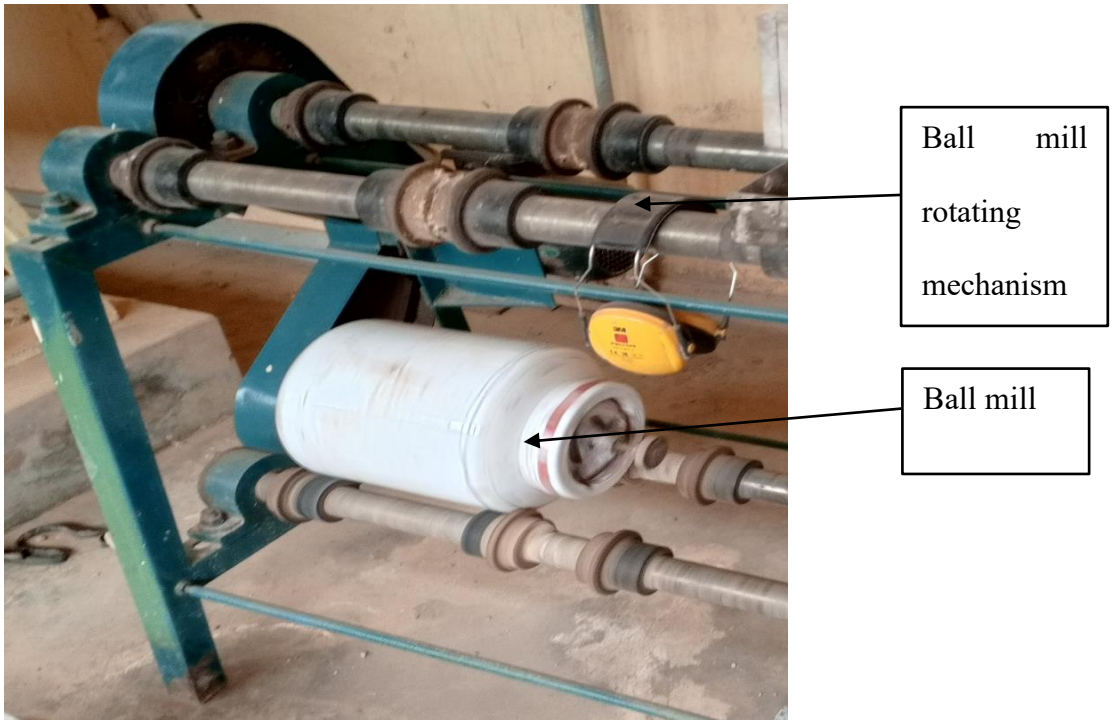

Figure 3. 7: Mixing of the raw materials using a ball mill.

3.6.2 Pressing of the Powder

A mixture of 250 g was weighed using an electronic beam balance, it was poured and spread evenly in a rectangular steel mold measuring 110 x 50 x10 mm. A

pressing force of 220 kN at a rate of 25mm/s was applied on the powder using a A-9210 VALENTIN STOSSIER hydraulic pressing machine shown in Figure 3.8. The pressure applied on the powder was 40 MPa calculated using equation 3.1. To prevent breaking from abrupt moisture loss, the green samples were allowed to dry in open air for two days after pressing. Figure 3.9 (a) and (b) shows the appearance of the samples after extrusion.

$$P = \frac{F}{A}, \tag{3.1}$$

where A is the cross-sectional area of the mold and F is the pressing force.

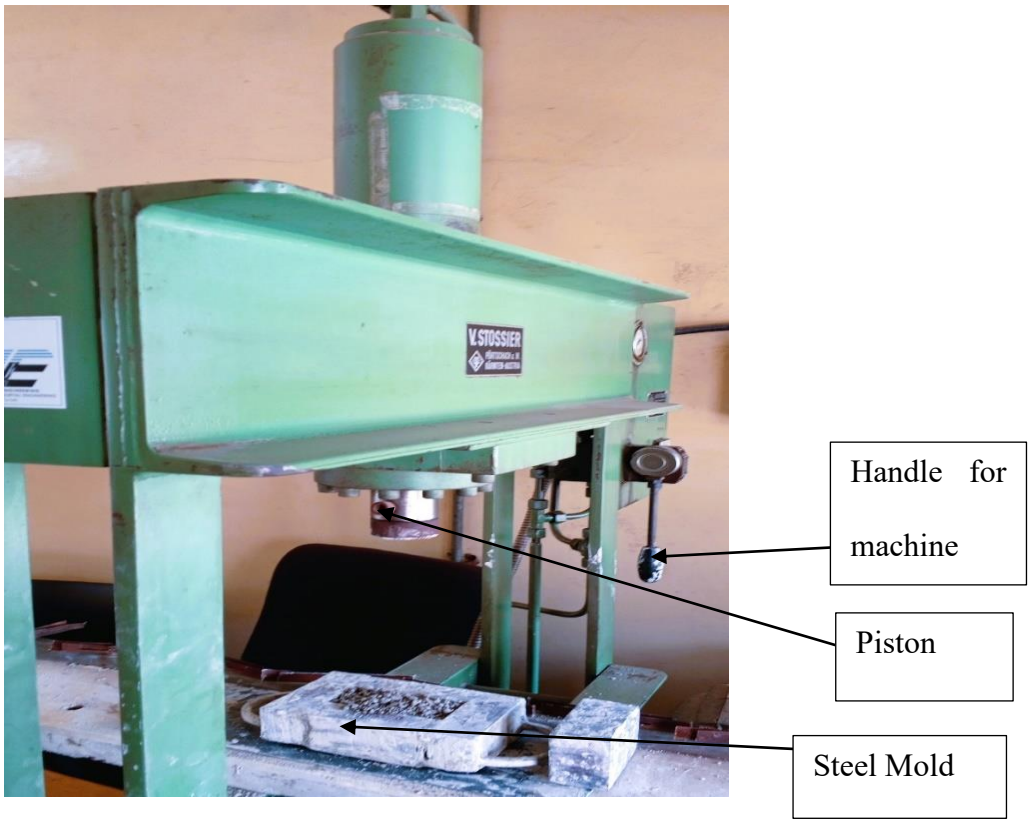

Figure 3. 8 : Shows a *V. STOSSIER* hydraulic-pressing machine

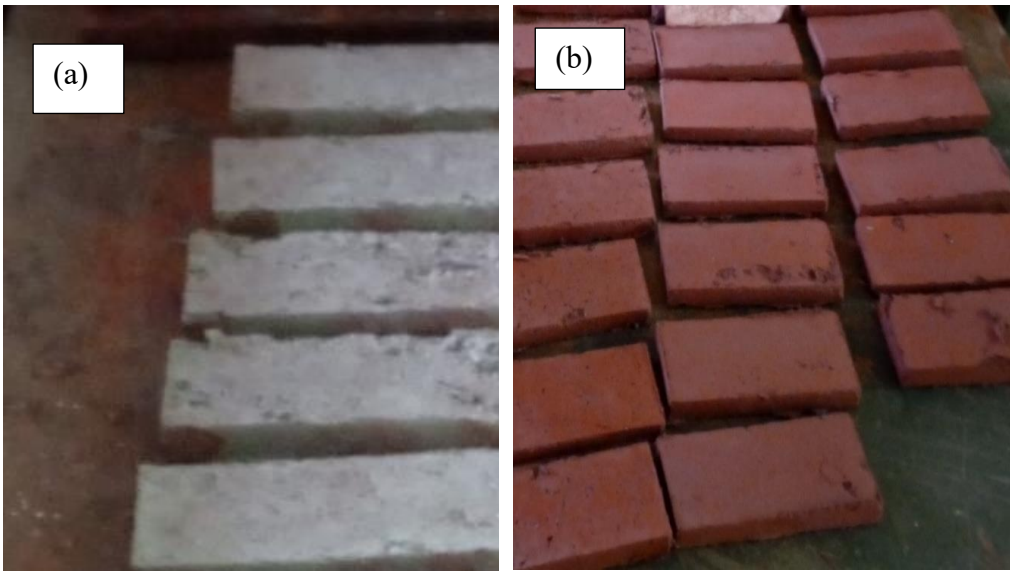

Figure 3. 9 (a) Tile samples without ferric oxide and (b) Tile samples with ferric oxide.

3.6.3 Firing of Samples

To remove the moisture that had been chemically held, the green samples were oven dried at 110 ºC for 24 hours. Dried samples were then fired to a peak temperature of 1200 ºC using an RHF 1600 Carbolite electrical furnace as shown in Figure 3.10. Firing temperature of 1200 °C was chosen as it offers an optimal balance for achieving full densification, along with complete sintering and vitrification of the raw materials (Ochen et al., 2021). This results in strong, dense, and low-porosity tiles, thereby enhancing their physical and mechanical properties. During firing, a fast-firing rate of 35 ºC/min was used and the furnace was later switched off to allow natural cooling. A fast-firing schedule was adopted in this study, which involved a rapid firing process to a peak temperature of 1200 ºC. This firing schedule was chosen because it enhances the formation of dense microstructures with limited grain growth, potentially enhancing the flexural strength of the ceramic tiles.

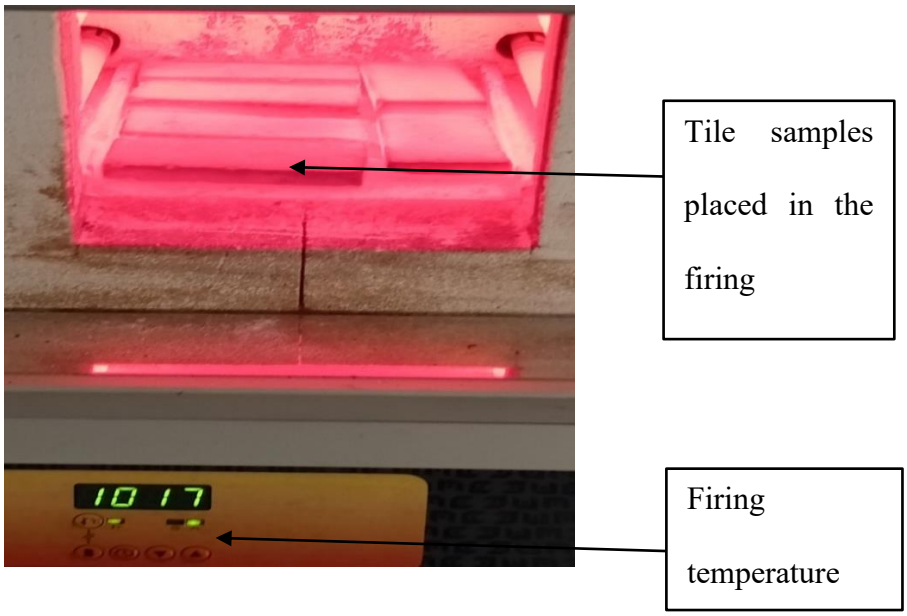

Figure 3. 10: Firing of the green tile samples in the electric furnace.

3.7 Experimental Measurements

Several methods were used to assess the physical properties, including linear shrinkage, water absorption, color, and texture.The mechanical properties considered included flexural strength and compressive strength.

3.7.1 Linear Shrinkage

Using a Vernier caliper, the measurements of the dry green samples and the fired samples were considered in millimeters as shown in Figure 3.11. A total of ten samples were obtained and measured from which the average and standard deviation were computed and thereafter, linear firing shrinkage (LS) was calculated using equation 3.1 (Sawadogo et al., 2023).

$$LS = \left(\frac{Lg-Lf}{Lf}\right) x100\ \%\ , \qquad (3.1)$$

where *Lg* is the measurement of the dry green sample, *Lf* is the measurement of the fired sample.

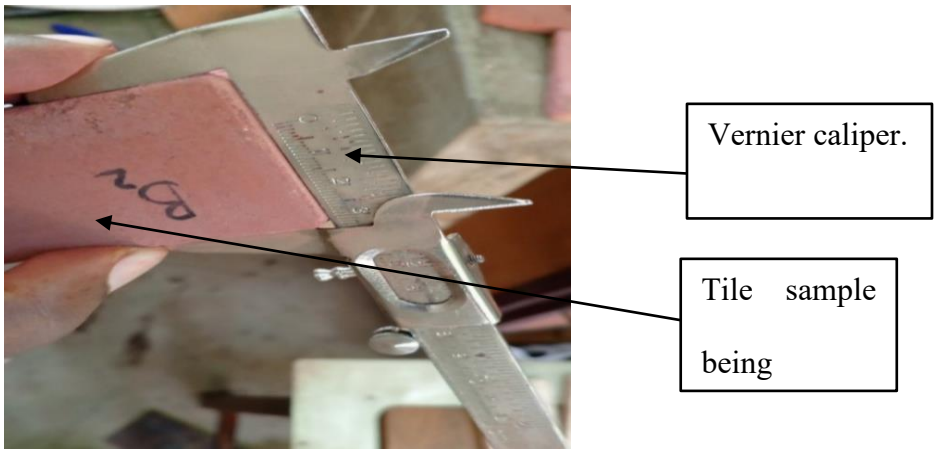

Figure 3. 11: Measurements of the dry body using a Vernier caliper.

3.7.2 Water Absorption

The water absorption was calculated using the ASTMC 373-88 standard for material testing. As shown in Figure 3.12, an electronic beam balance was used to determine the mass of each fired sample, and the result was noted as M_f. After weighing, the specimens were fully submerged in water and subjected to boiling at approximately 100°C. Following the boiling process, the samples were allowed to remain immersed and soak for an additional 12 hours at ambient room temperature to ensure complete water penetration into any open pores. The mass of the immersed fired sample was then measured using an electronic beam balance, model number PRC B500 as shown in Figure 3.12 and recorded as M_s. A total of ten samples were measured from which the average value and the standard deviation were obtained. The water absorption (W.A) was then calculated using equation 3.2 (Atidi et al., 2023).

$$WA = \frac{M_s - M_f}{M_f} \; x \; 100 \; \%, \qquad (3.2)$$

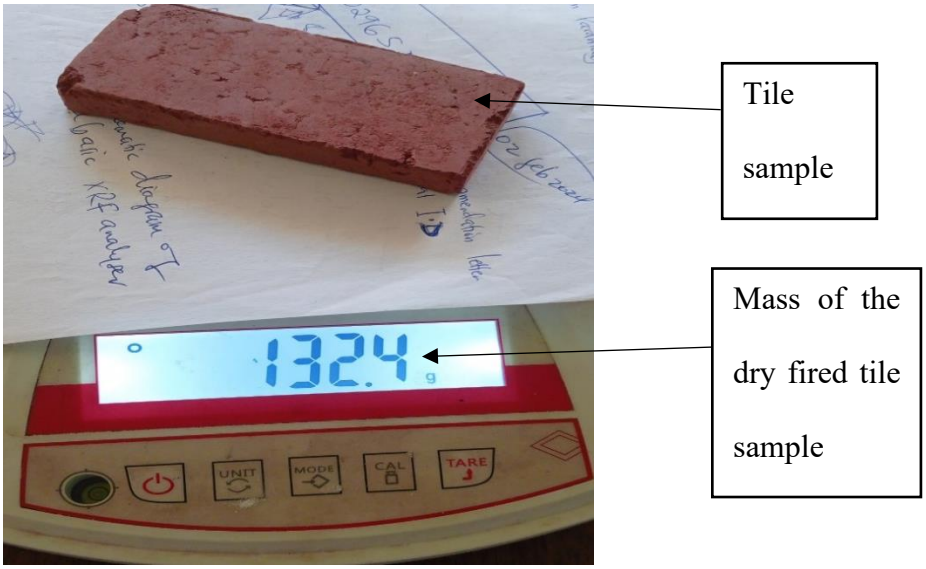

Figure 3. 12: Measurement of the dry mass of the sample using an electronic beam balance.

3.7.3 Texture and Color

The texture of the sample was studied by gently rubbing with bare hands and the color was examined visually under natural lighting conditions, using the un-aided eyes (Ochen et al., 2021).

3.7.4 Flexural Strength

The three-point flexural test method was used to determine the flexural strength. Using a Vernier caliper, the center of the sample was determined and marked off at a distance equal from both sides over the whole span. In order to provide a loading force to the ceramic tile sample, the prepared samples were thereafter placed on the Testometric Universal Testing Machine (UTM) with the loading pin placed on the machine's upper part, as seen in Figure 3.13.Using the loading

pin, the loading force P was applied at a rate of 1 mm/min to the centre of the marked tile. A value of P at failure was observed and noted. The modulus of rapture (MOR) was computed as the flexural strength of the sample. The modulus of rapture was calculated using equation (3.3) (Ochen et al., 2021). The average value of the five samples and their standard deviation was considered as the overall value of the flexural strength.

$$MOR = \frac{3lp}{2bd^2}, \tag{3.3}$$

where, MOR is the modulus of rapture strength, l is the length of the span, b is the width and d is the thickness.

The length of the samples were measured in millimeters using a Vernier caliper.

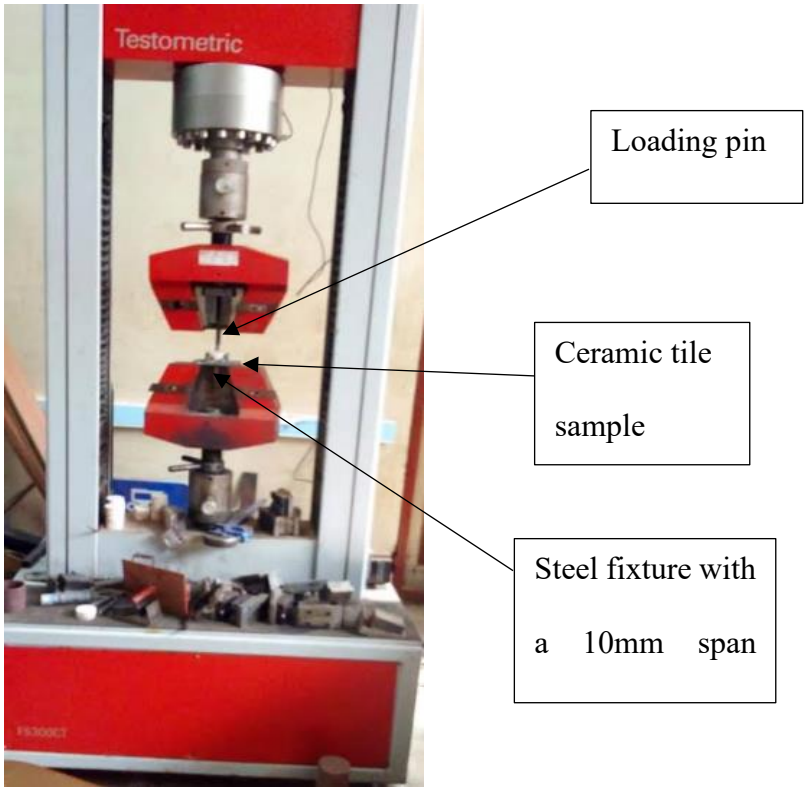

Figure 3. 13: Determination of MOR on a universal testing machine

3.7.5 Compressive Strength

A compression-testing machine, as illustrated in Figure 3.14, was used to determine the compressive strength. The test was performed according to the BS EN 12390-3 (2009) standard. The sample was placed in between the two steel plates on the machine. Progressive compressive loading of the machine was then applied to the specimen until failure occurs. The loading at failure was then recorded as Q. The cross-sectional area of the sample was determined by measuring length and width of the samples using a Vernier caliper and later multiplying the two to get the cross-sectional area. The average and standard deviation of the ten samples was considered and the compressive strength $(C.S)$ was then calculated using equation 3.4 (Ochen et al., 2021).

$$\mathrm{C.S} = \frac{\mathrm{Q}}{\mathrm{A}}, \tag{3.4}$$

where, Q is load at failure and A is the cross-sectional area of the sample.

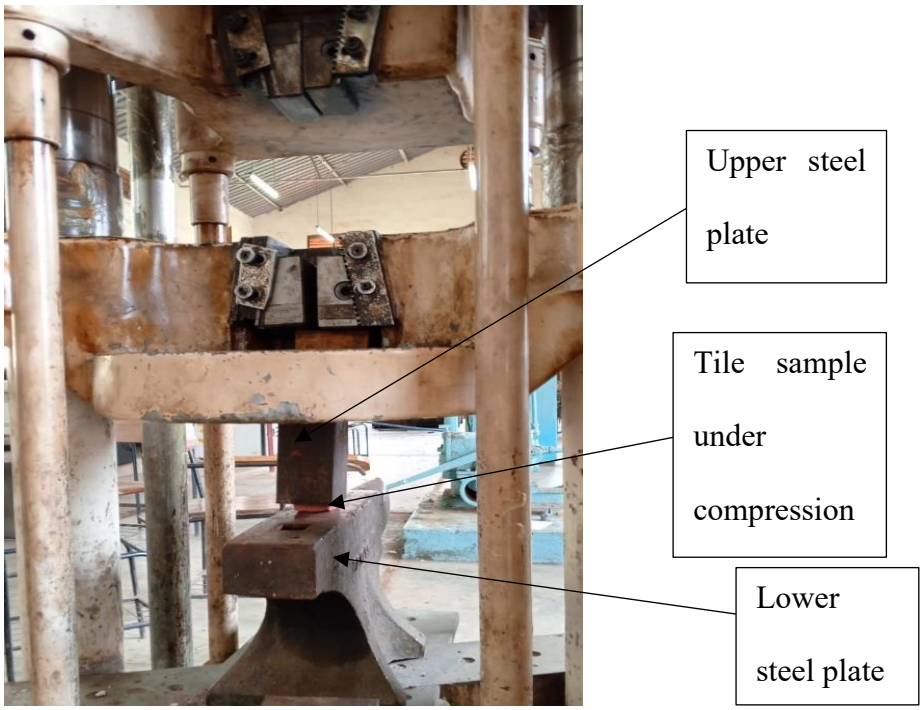

Figure 3. 14 : Determination of compressive strength on a compression-testing machine

3.8 Characterization of the Fired Products

3.8.1 SEM Analysis

A FEG-SEM device, LEO 1530, equipped with a GEMINI column, was used to perform microstructural examination on the fired tile samples. For this study, polished and sectioned samples of the sintered tiles were utilized. The specimens were subjected to cleaning; drying, polishing, and later examined using a FEG-SEM instrument after being soaked in 40% concentrated hydrochloric acid for 25 seconds. The Scanning Electron Microscopy machine (SEM) was used to scan tile samples with a focused electron beam to produce high-resolution images of the tile surfaces. The resulting images showed the microstructure of the tiles containing various ratios of ferric oxide as the waste material.

Before the analysis, preparation of the samples started with the wearing a pair of gloves and cleaning the samples. The samples were then reduced to small portions in order to be stable in the vacuum. Stubs were used and the specimen holder with isopropanol and Kim wipe papers were used. The fragment samples were then firmly held on Al-stubs using C-tape and fixed onto the ZEISS specimen holder. Eight (8) stubs were then loaded and mounted the thin sections directly on the specimen holder. Maps were drawn in order to easily locate each sample in the SEM.

The analysis of the samples involved loading the specimen holder into the Scanning Electron Microscopy machine and then adjusting the SEM operating conditions to suitable conditions i.e. Voltage, Working Distance (WD), Display of live sample, Magnification / Focus, Brightness / Contrast, Stigmation, Aperture Alignment. The SE2 detector was selected and the images acquired and later saved for analysis. The results of the microstructure analysis can be found in Table 4.1.

3.8.2 XRD Analysis

The fired samples were examined using X-ray Diffraction (XRD) to determine the phases present. Samples were powdered to a fine grain size (<150 μm), and the powdered samples were analyzed using a Bruker D2 Phaser XRD. The data obtained from the XRD analysis were then processed using Match 4 powder diffraction software for phase identification and semi-quantitative analysis. X-ray diffraction (XRD) was an effective method for identifying the phases present in unknown polycrystalline powders. During the preparation phase, the samples were ground using a ball mill to achieve an average particle size of

< 75 μm and the crystalline powders obtained were pressed into the sample holder, having a smooth surface. The samples were held at an angle of 45 degrees to obtain better results. Before the analysis, all scans were smoothed, theta corrected, and the background removed. XRD analysis was subsequently carried out by matching the diffraction pattern obtained from the unknown sample with reference patterns of established crystalline phases. This comparison was performed automatically, where the experimental diffraction profile was evaluated against standardized diffraction scans of pure compounds stored in the International Centre for Diffraction Data (ICDD) Powder Diffraction File (PDF) database. This process enabled accurate identification of the mineral phases present in the sample. The Particle X-Ray Diffraction (PXRD) method was also used in this study. The crystalline particle were measured in equal quantities and then ground to form particles of 10 μm particles using a ball mill. The PXRD profile was checked and the preliminary measurement conditions using a one-dimensional (1D) detector at a speed of 50°/min and the 2θ range of 3–80°, with a step size of 0.01° was used. The data obtained included the diffraction peak at the lowest angle.

3.9 Optimization of the Properties

Three-factor and 2^3 full factorial Central Composite Design (CCD) based on Response Surface Methodology (RSM) was employed to design the experiments. The resulting data were analyzed using Design Expert Software 13. Statistical evaluations such as regression analysis were conducted to assess the quality and predictive capability of the developed models. Key metrics for model appropriateness include coefficient of determination (R^2), adjusted R^2,

anticipated R^2, acceptable precision, and coefficient of variation (CV). The signal-to-noise ratio was evaluated with adequate precision, and CV was calculated as the ratio of the standard error to the mean of the observed response.

The signal-to-noise ratio was assessed with adequate precision, and CV calculated the ratio of the standard error to the mean of the observed response.

The statistical significance of the models and their regression coefficients was determined using Fisher's F-test and associated p-values derived from ANOVA at a 95% confidence level.

The numerical optimization tool was used to identify the optimal combination of ferric oxide, feldspar, kaolin, ball clay and sand content to achieve the desired flexural strength.

CHAPTER FOUR: RESULTS AND DISCUSSIONS

4.1 Introduction

This chapter analyses the results and discusses the findings of the study on the tiles made from ferric oxide as a waste from steel industries, with a focus on key mechanical properties such as flexural strength, compressive strength and physical properties such as water absorption, linear shrinkage. These properties (flexural strength and water absorption) were analyzed based on the ISO 13006 standard of ceramic tiles and compressive strength was performed according to BS EN 12390-3 (2009) standard. Additionally, the results from the mechanical properties were compared with ISO 13006 standard for ceramic tiles. Optimization using Design Expert 13 software was carried out to effectively identify the most desirable mixing proportions and obtain the best of fit results, leading to sample tiles with enhanced performance for the construction industry. Optimized results were compared with experimental data.

4.2 Chemical Composition of the Raw Materials

The XRF method was used to analyse the chemical composition, and Table 4.1 shows the XRF results. This was carried out in order to evaluate the suitability of the raw materials used in the study.

4.2.1 Chemical Composition of Kaolin

The percentage composition of oxides in kaolin seen in Table 4.1 shows that silica (SiO_2) and alumina (Al_2O_3) were the most dominant oxides present each exhibiting 62.5 % and 28.3 % respectively. Low composition (≤ 6 %) of the flux

oxides such as MgO, K_2O, CaO and P_2O_5 were found present however, the oxides such as Na_2O, Cr_2O_3, and Ti_2O were absent. Additionally, a small amount of iron oxide (Fe_2O_3) of 3 % was found present in the kaolin.

Elgamouz et al., (2019) reported that due to the oxidation process during the sintering process of the samples, the presence of iron oxide affects the color of the fired product, see Figure 3.8 (a). Furthermore, the presence of high silica and alumina content in kaolin has a positive effect on the mechanical strength of the final products developed (Benali et al., 2016). In the presence of heat, alumina and silica react to form mullite crystals, more details of this reaction are found in subsection 4.6.1.

4.2.2 Chemical Composition of Feldspar

To ascertain and evaluate the kind of oxides present in feldspar, the raw material was subjected to an XRF analysis to determine its chemical composition. According to Yuan et al., (2019), feldspar is an alumina-silicate that also contains an abundant amount of mineral elements such as potassium, phosphorous, calcium, among others. Table 4.1 also displays the chemical makeup of the feldspar, and it can be seen that silica (SiO2) was the most frequent oxide present, accounting for 68.0 %.

Calcium oxide (CaO) which is a fluxing oxide exhibited the second highest composition in the feldspar with 19.1 %. Alumina (Al_2O_3) and iron oxide (Fe_2O_3) were also found to be present in the feldspar in a range of 2-8 %. The flux oxides such as MgO, K_2O, and P_2O_5 were found to be present in very small quantities as shown in Table 4.1. However, metal oxides of mineral elements

such as sodium, chromium, and titanium were absent, similar results were reported by Bell et al., (2020). Feldspar helps in the vetrification processes, when fired at 1200 ^{o}C the flux oxides such as CaO (see Table 4.1) melts and the liquid phase formed occupies the pores present hence improving on the mechanical strength of the final product.

4.2.3 Chemical Composition of Ferric Oxide

Ferric oxide, as one of the raw materials used in the formulation of tiles in this study, was subject to a chemical composition test using the XRF method. Analysis results presented in Table 4.1 revealed that iron oxide (Fe_2O_3) exhibited the highest value of 98.3 %.These results are consistent with those obtained by Abd Halim et al., (2023). Unlike kaolin and feldspar, the XRF analysis revealed that alumina (Al_2O_3) was absent in the ferric oxide but also the silica (SiO_2) content was negligible at only 0.006 %. Additionally, the flux oxides such as Ca_2O, MgO, and P_2O_5 were found to be in a range of 0.006 - 0.618 %, which is also negligible. Other metal oxides found absent in the ferric oxide were K_2O, Na_2O, and Ti_2O. Same results were highlighted by Blagojević et al., 2018. The presence of high iron oxide in ferric oxide has two roles; firstly, it is responsible for the brown color of the fired products as seen in Figure 3.9 (a) (Zhao et al., 2017). Secondly, it acts as fluxing oxide (Zhao et al., 2017), details are explained in section 4.2.2.

4.2.4 Chemical Composition of Ball Clay

Results of chemical composition of ball clay used in this study, as determined using an XRF analysis is presented in Table 4.1. The results indicate that ball

clay primarily contained SiO_2 (65.4 %), Fe_2O_3 (13.0 %), and Al_2O_3 (10.1 %) as the main oxides present. The results were consistent with those obtained by Khalil et al., 2024. Flux oxide K_2O constituted only 0.1 % in the ball clay. Flux oxides such as MgO and CaO corresponded to a total of 8.5 %. Oxides of heavy metals such as titanium and chromium were found present in the ball clay and these had compositions of 2.0 % and 0.1 % respectively. However, the presence of iron oxide resulted in the coloration of the final product (see Figure 3.8 a). In addition, iron oxide present in ball clay also contributed to the vetrification of the final product.

4.2.5 Chemical Composition of Sand

A chemical analysis of the sand particles using XRF is presented in Table 4.1. The data shows that silica (SiO_2) was the most dominant compound present in the sand exhibiting a composition of 85.7 % followed by alumina (Al_2O_3) with composition of 10.9 %. Similar results were obtained by Ariyanto et al., (2023). Flux oxides such as Na_2O and K_2O had a combined composition of 1.6 %. Fe_2O_3 which has a coloring effect on the final fired product as reported by Khalil et al., (2024), exhibited a negligible value of 0.7 %. Additionally, besides the Fe_2O_3, the other two coloring metal oxides such as Cr_2O_3 and Ti_2O were found to be absent in sand. Sand is known to provide dimensional stability to the fired products consequently avoiding warping as seen in Figure 3.8 (a) and (b). Sand has a high melting point of 1610 ^oC and as result, it gives the body dimensional stability during the sintering process (Wang et al., 2021).

Table 4. 1: Chemical composition of the raw materials used in the formulation of tiles.

Oxides	Raw materials (%)				
	Kaolin	Feldspar	Ferric oxide	Ball clay	Sand
SiO_2	62.527	68.018	0.006	65.455	85.793
Al_2O_3	28.329	8.207	0.000	10.151	10.967
Fe_2O_3	2.964	2.798	98.317	13.06	0.732
CaO	5.342	19.177	0.618	8.07	0.000
MgO	0.009	0.389	0.389	0.431	0.474
K_2O	0.233	0.931	0.000	0.179	1.549
P_2O_5	0.315	0.219	0.006	0.244	0.297
Cr_2O_3	0.000	0.000	0.229	0.197	0.000
Na_2O	0.000	0.000	0.000	0.000	0.141
Ti_2O	0.000	0.000	0.000	2.015	0.000
LOI	0.281	0.261	0.435	0.198	0.047
Total	**100**	**100**	**100**	**100**	**100**

LOI-Loss on Ignition.

4.3 Particle Size Distribution

The particle sizes affect the firing temperature and pore size of ceramic tiles developed. According to Isobe et al., 2012, the growth of pores in the ceramic body depends on the particle sizes and the pressing pressures used during preparation. In this study, the particle size distribution was determined using the hydrometer method and the data was analyzed using origin pro software version 2025. Figure 4.1 shows the particle size distribution characteristics of ball clay, feldspar, kaolin, ferric oxide, and sand. The particle size diameter which was

calculated using the volume weighted mean formula for all powder samples of raw materials found that the samples had different particle size distributions.

The particle size distribution (PSD) results, presented in Figures 4.1(a–e), reveal notable differences in the fineness and range of the raw materials used in the ceramic tile formulation. Feldspar exhibited a particle size range of 0.001– 0.43 mm**,** indicating the presence of both fine and coarse particles. This broad distribution suggests that feldspar can contribute to fluxing behavior during sintering while also helping improve the packing density of the ceramic body (H. J. Alves et al., 2012).

Ferric oxide, kaolin, ball clay and sand showed identical PSD ranges of 0.001– 0.063 mm, indicating a more finer particle size distribution than feldspar with limited coarseness. The finer size of ferric oxide enhances its reactivity and coloration effect, while sand in this case contributes to structural strength and dimensional stability during firing due to its moderate fineness. Kaolin's higher proportion of fine particles supports its role as a plasticizer and matrix-forming material, promoting better particle cohesion and surface quality of the green body. As expected, ball clay had the same PSD range of 0.001– 0.063 mm, reflecting its well-known high plasticity and excellent green body binding properties. The extremely fine particles (ball clay) enhance workability and green strength. However, the excessive fineness increased the risk of cracking as observed in some samples (see Figure 4.2). These cracked samples were not considered for experimental analysis.

Robertson et al., 2010 stated that finer particles in a range of 1-10 μm require lower sintering temperatures but lead to high transport resistances because of

small pore sizes. Conversely, coarser particle sizes tend to reduce the mechanical strength of the ceramic body, primarily due to the formation of larger pore structures and less efficient particle packing. These macro pores not only compromise densification but also require higher firing temperatures to achieve comparable strength and vitrification levels (Yan et al., 2013). The finer particles used in the formulation of tile samples as indicated in the particle size distribution data suggests that the samples required lower sintering temperatures of ≥1200 °C. As a result, the samples were fired at 1200 °C hence resulting into enhanced mechanical properties championed by the vetrification of the body.

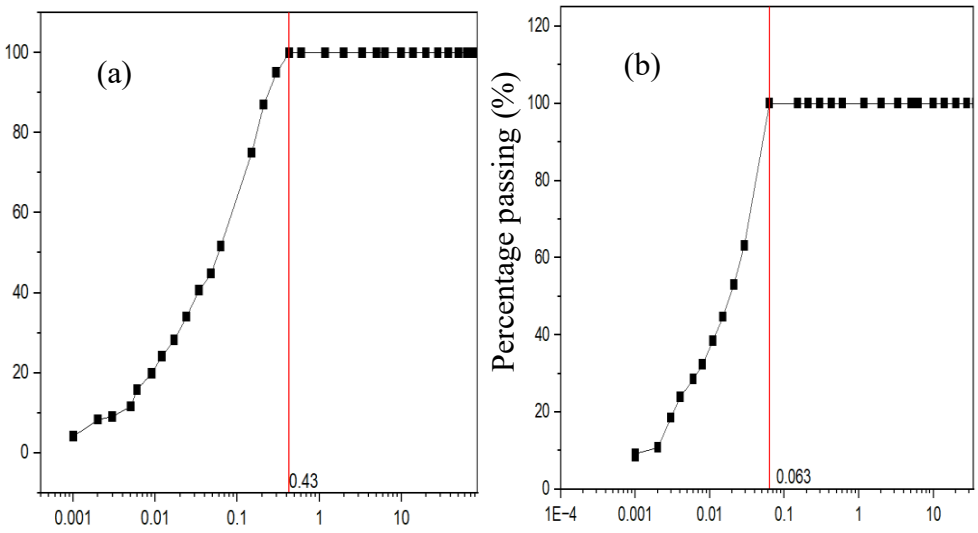

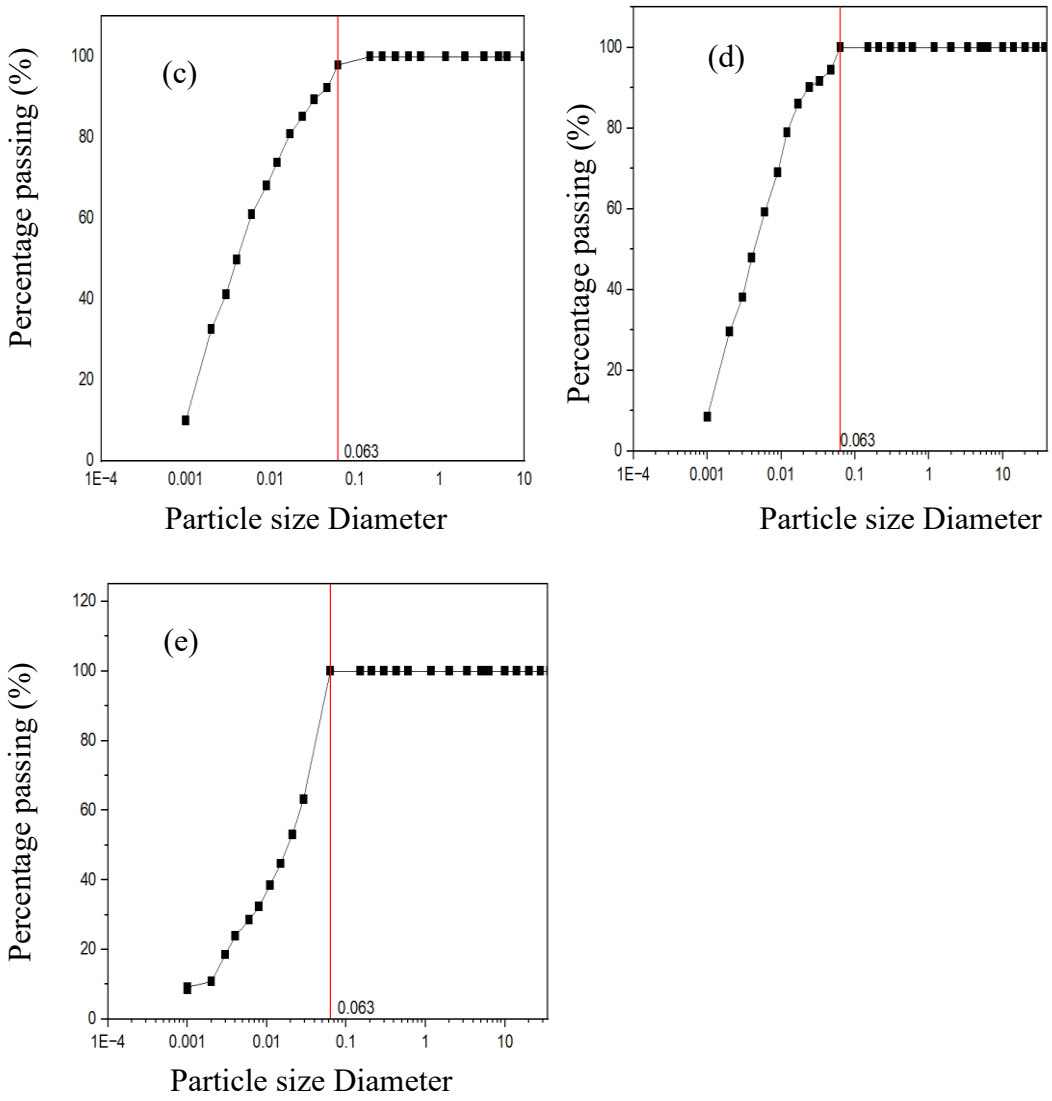

Figure 4. 1 Shows a logarithmic plot of particle size distribution for (a) feldspar, (b) ferric oxide, (c) kaolin, (d) sand and (e) ball clay.

4.4 Microstructure Analysis

The SEM micrographs in Figure 4.2 revealed that all tile specimens exhibited a generally homogeneous structure, which was notably influenced by the proportion of ferric oxide relative to feldspar at a constant sintering temperature of 1200 °C. The results demonstrate that increasing the amount of ferric oxide in a range of 0-15 wt % resulted into a decrease in the presence of open pores

consequently reducing the water absorption of the tile products as seen in Figure 4.6. Figure 4.2 (a), corresponding to the control tile sample without ferric oxide (0 %) and sintered at 1200 °C shows no evidence of mullite fiber formation. In contrast, Figures 4.2 (b) to (e) which represent samples containing ferric oxide in a range of 10-30 wt % exhibited a rougher texture with mullite fibres and quartz crystals clearly visible in the micrographs. The presence of mullite fibres resulted in the improvement of the flexural strength of the fired samples as seen in Figure 4.5 (Njoya et al., 2017).

The tile samples containing 15 wt % ferric oxide exhibited the highest flexural strength of 45.34 MPa as seen in Table 4.2 and the lowest water absorption of 9.62 % (see Table 4.3). This is attributed to the presence of a dense microstructure that contains mullite phases and quartz crystals as seen in Figure 4.2 (d). This is further supported by the XRD data as described in Figure 4.4, which confirms the presence of mullite and quartz in the samples.

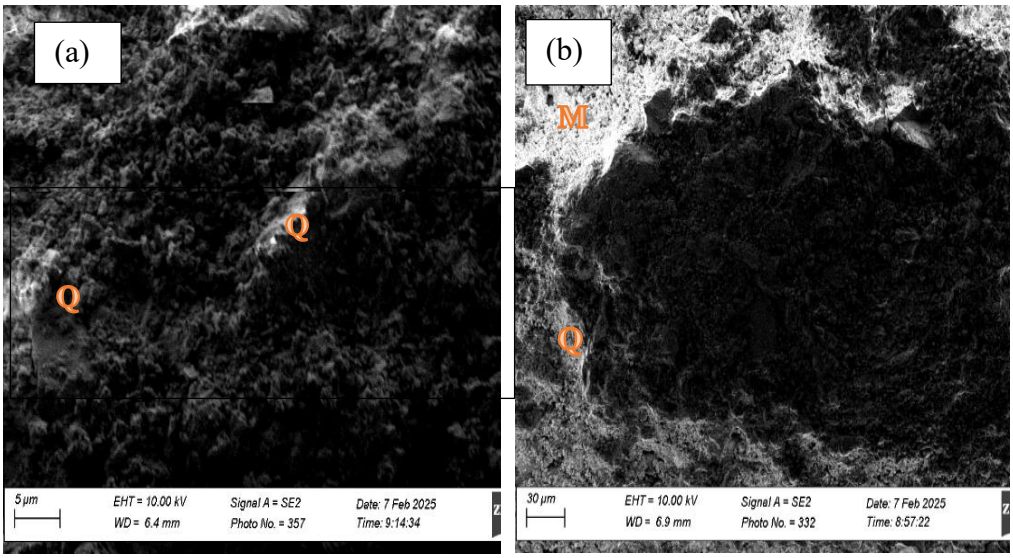

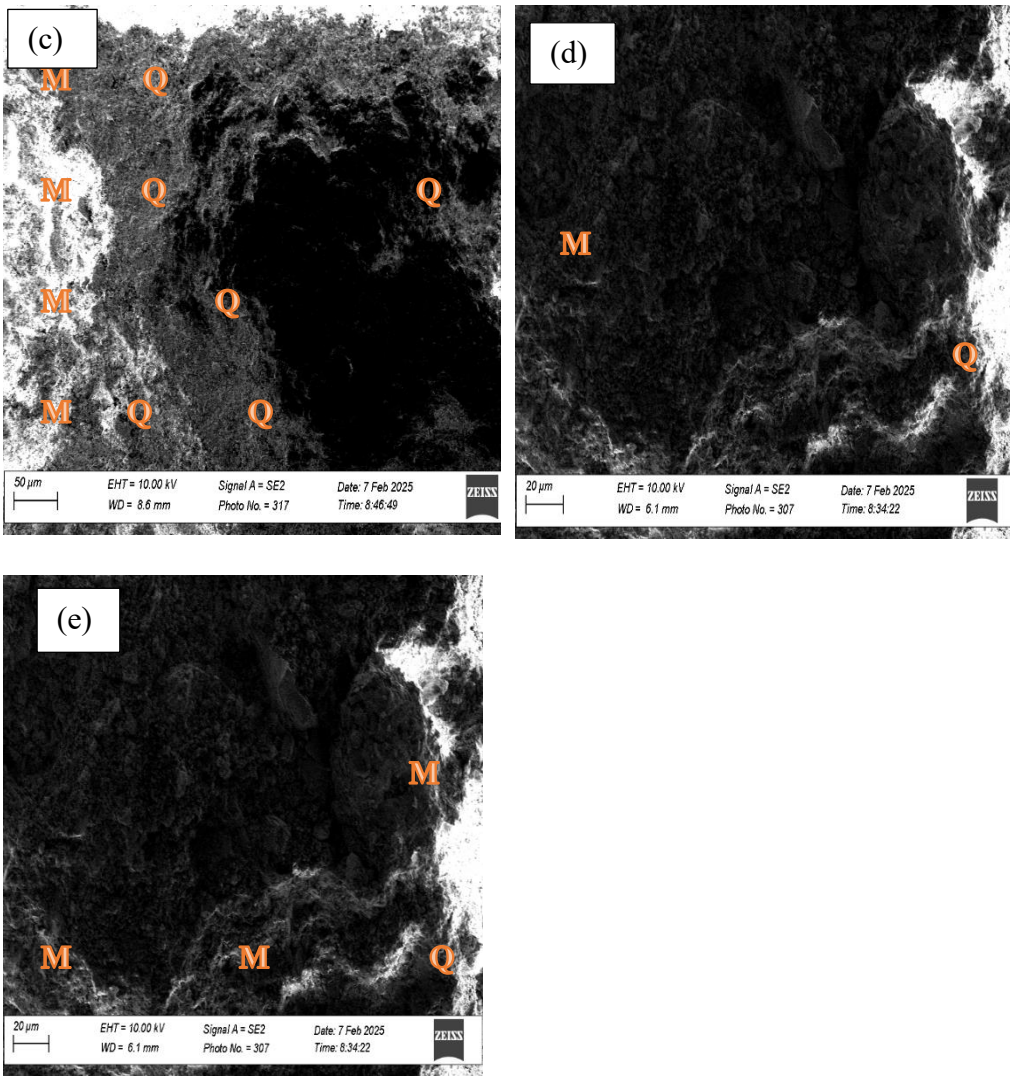

Figure 4. 2: (a) Tile sample with 0 % ferric oxide (b) Tile sample with 10 % ferric oxide, (c) Tile sample with 15 % ferric oxide, (d) Tile sample with 20 % ferric oxide, (e) Tile sample with 30 % ferric oxide.

Table 4. 2: Flexural strength of the developed tile samples.

Parameter	Tiles samples				
	1	**2**	**3**	**4**	**5**
Width (mm)	48.4	50	50	48	50
Thickness (mm)	15	13.2	12.2	12	14
Maximum force (N)	2534	2293	2309	2346	2417
Modulus (MPa)	540.1	22200.2	32602.6	14758.4	1292.5
Flexural Strength (MPa)	11.39	43.96	45.34	38.59	40.32

Table 4. 3: Water absorption of the developed tile samples.

Parameter	Tiles samples				
	1	**2**	**3**	**4**	**5**
Average mass of the fired sample, M_f(g)	129.06	112.93	105.83	106.3	109.46
Average mass of saturated sample, M_s (g)	143.87	124.18	115.8	116.91	121.76
Average water absorption	11.77	9.99	9.62	10.01	11.24

4.5 XRD Analysis of the Samples

The representative XRD patterns of the sintered samples at 1200 °C shown in Figure 4.4 (a) to (e) revealed distinct diffraction peaks, indicating the coexistence of both crystalline and amorphous phases within the fired tile samples. The industrial rapid firing process used for ceramic tiles leads to the development of newly formed and residual crystalline phases embedded within

a glassy matrix referred to as Albite. Prominent diffraction peaks corresponding to mullite, quartz, albite, periclase, cristobalite, and hematite confirmed the presence of these phases within the microstructure. Residual quartz, a key crystalline component, was identified by its sharp, well-defined peaks, reflecting its stable lattice structure. Mullite, essential for enhancing mechanical strength, also exhibited characteristic diffraction features. Furthermore, the presence of residual albite, periclase, and cristobalite was confirmed, each playing a significant role in defining the overall phase composition of the ceramic body.

XRD Pattern of the control tile sample containing 0 wt % ferric oxide shows two distinct mineral phases, quartz (SiO_2) at 77.3 %, and albite ($NaAlSi_3O_8$) at 22.7 % as seen in Figure 4.4 (a). Albite is a glassy phase, which embeds the quartz crystals. Since Quartz has a high thermal expansion coefficient of 14.5×10^{-6} /°C than its surrounding (albite) at 4.5×10^{-6} /°C, there is a faster shrinkage rate (Liang et al., 2022). This difference causes uneven shrinkage within the sample, generating internal stresses that leads to crack formation and decrease flexural strength when quartz is present at high composition. This is evident from the flexural strength results observed in Figure 4.5.

The diffractogram in Figure 4.4 (b) shows the XRD analysis of tile sample (10 wt % ferric oxide, 20 wt % feldspar, 20 wt % ball clay, 40 wt % kaolin, 10 wt % sand) with 56.1 % quartz (SiO_2), 29.4 % mullite ($Al_6Si_2O_{13}$) and Hematite (Fe_2O_3) at 14.5 %. Mullite is formed through a solid-state reaction during the high temperature sintering of alumino-silicate raw materials, such as kaolin, sand, feldspar and ball clay. This is due to the presence of SiO_2 and Al_2O_3, as confirmed by the chemical composition of kaolin, sand, feldspar and ball clay

determined through the XRF analysis. In general, an increase in ferric oxide content led to a corresponding rise in the mullite phase and a reduction in quartz crystal content, as illustrated in Figure 4.3. Specifically, increasing ferric oxide from 0 % to 15 % resulted in a steady decline in quartz content from 77 % to 38 %. A further increase in ferric oxide from 15 % to 30 % resulted in a rise in the mullite phase from 30 % to 40 %. This indicates that increasing ferric oxide levels promotes mullite formation during sintering. The raw data supporting these observations are presented in Table 4.4, which were extracted from the XRD data shown in Figure 4.3. Notably, all samples containing mullite phases exhibited high flexural strength values, ranging from 38.59 MPa to 45.34 MPa.

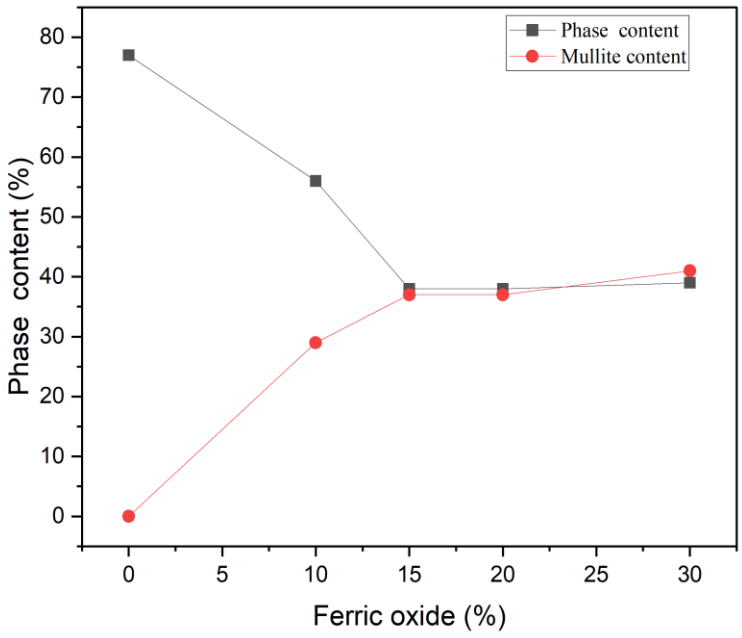

Figure 4. 3: Variation of ferric oxide with mullite and quartz content.

Table 4. 4: Phase identification in relation to ferric oxide.

Ferric oxide (wt %)	Mullite content (%)	Quartz content (%)
0	0	77
10	29	56
15	37	38
20	37	38
30	41	39

Hematite (iron oxide) is mainly responsible for coloration in ceramic tiles and the brown coloration of the samples is attributed to the presence of hematite as seen in Figure 3.9 (b). The high percentage composition of hematite is due to the presence of ferric oxide in tile samples as indicated in Table 4.1. The presence of hematite also enhances vitrification in ceramic bodies by acting as a fluxing agent. During firing, Fe_2O_3 melts creating a liquid phase due to liquid phase sintering hence resulting into improved vetrification. When incorporated in suitable amounts and subjected to sintering at high temperatures (typically between 1100 – 1250 °C), hematite promotes the formation of a glassy or liquid phase (Jalaluddin et al., 2024). This molten phase flows into pores and voids, thereby reducing porosity and improving the densification of the ceramic matrix. As a result, enhanced vitrification leads to decline in water absorption (Figure 4.7)**,** increase mechanical strength (Figure 4.5), and better frost resistance in the final product.

The presence of cristoballite present in the tile samples with 20 wt % ferric oxide, 10 wt % feldspar, 20 wt % ball clay, 40 wt % kaolin, 10 wt % sand and 30 wt % ferric oxide, 0 wt % feldspar, 20 wt % ball clay, 40 wt % kaolin, 10 wt % sand

indicates the presence of silica (SiO_2) which is a high temperature polymorph that forms when quartz transforms at temperatures above 1200 °C. This helps in improving the thermal shock and dimensional stability of the tile samples formed. Periclase is a magnesium oxide (MgO) phase that is formed in ceramic tiles particularly in formulations that include magnesium-bearing raw materials, as shown in Table 4.1, with the exception of ferric oxide, which does not contribute to MgO content. It is highly refractory at high temperatures.

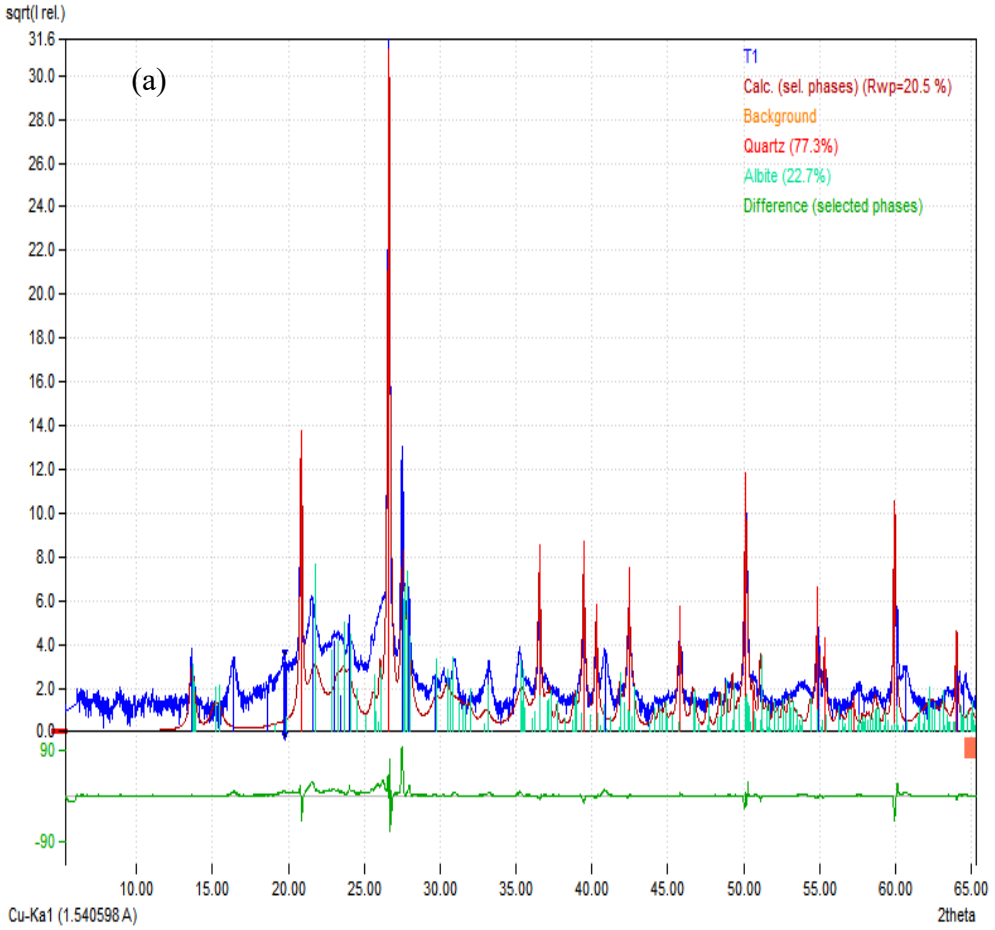

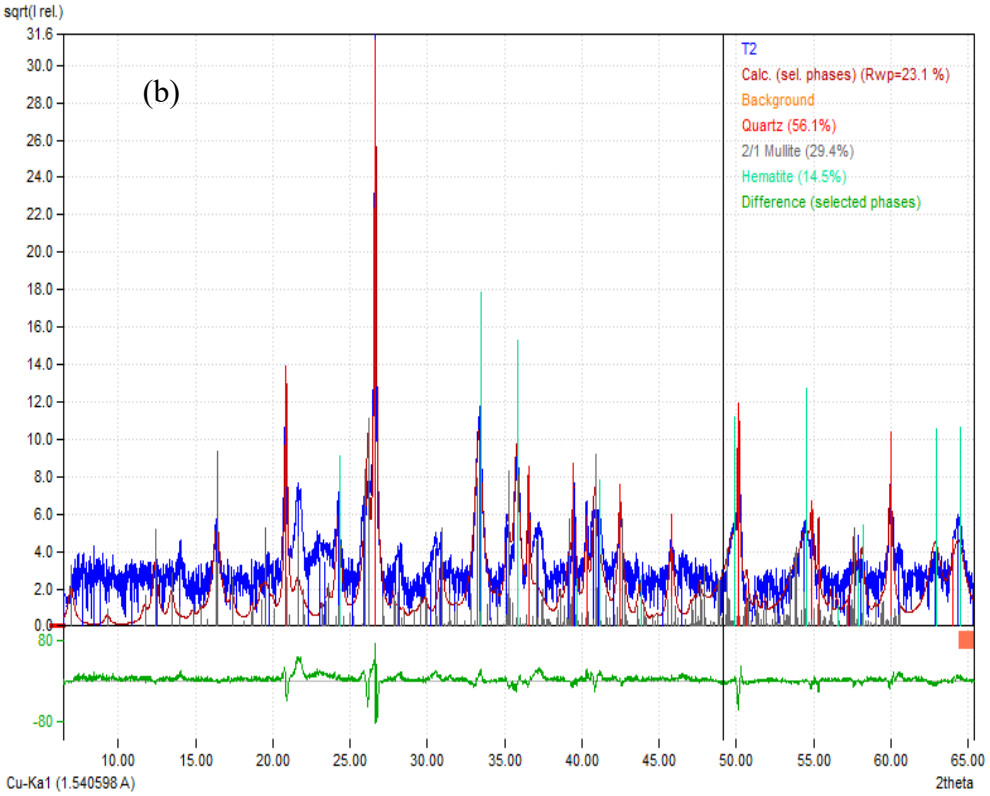
sqrt(I rel.)
(b)
T2
Calc. (sel. phases) (Rwp=23.1 %)
Background
Quartz (56.1%)
2/1 Mullite (29.4%)
Hematite (14.5%)
Difference (selected phases)
Cu-Ka1 (1.540598 A)
2theta

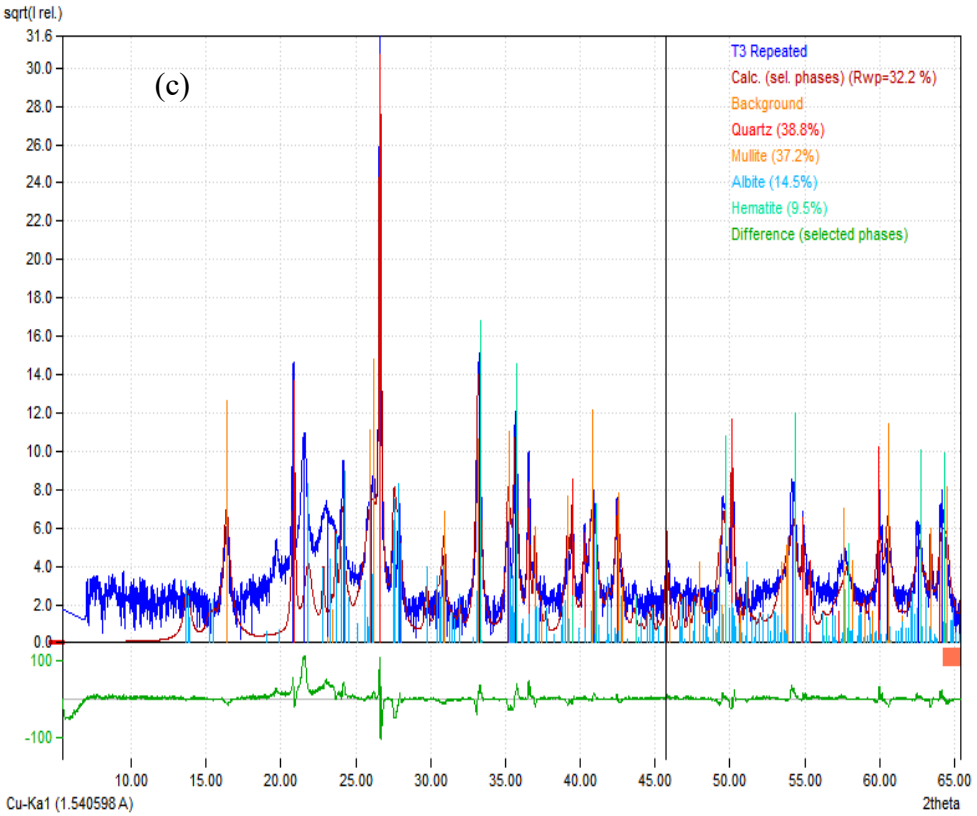
sqrt(I rel.)
(c)
T3 Repeated
Calc. (sel. phases) (Rwp=32.2 %)
Background
Quartz (38.8%)
Mullite (37.2%)
Albite (14.5%)
Hematite (9.5%)
Difference (selected phases)
Cu-Ka1 (1.540598 A)
2theta

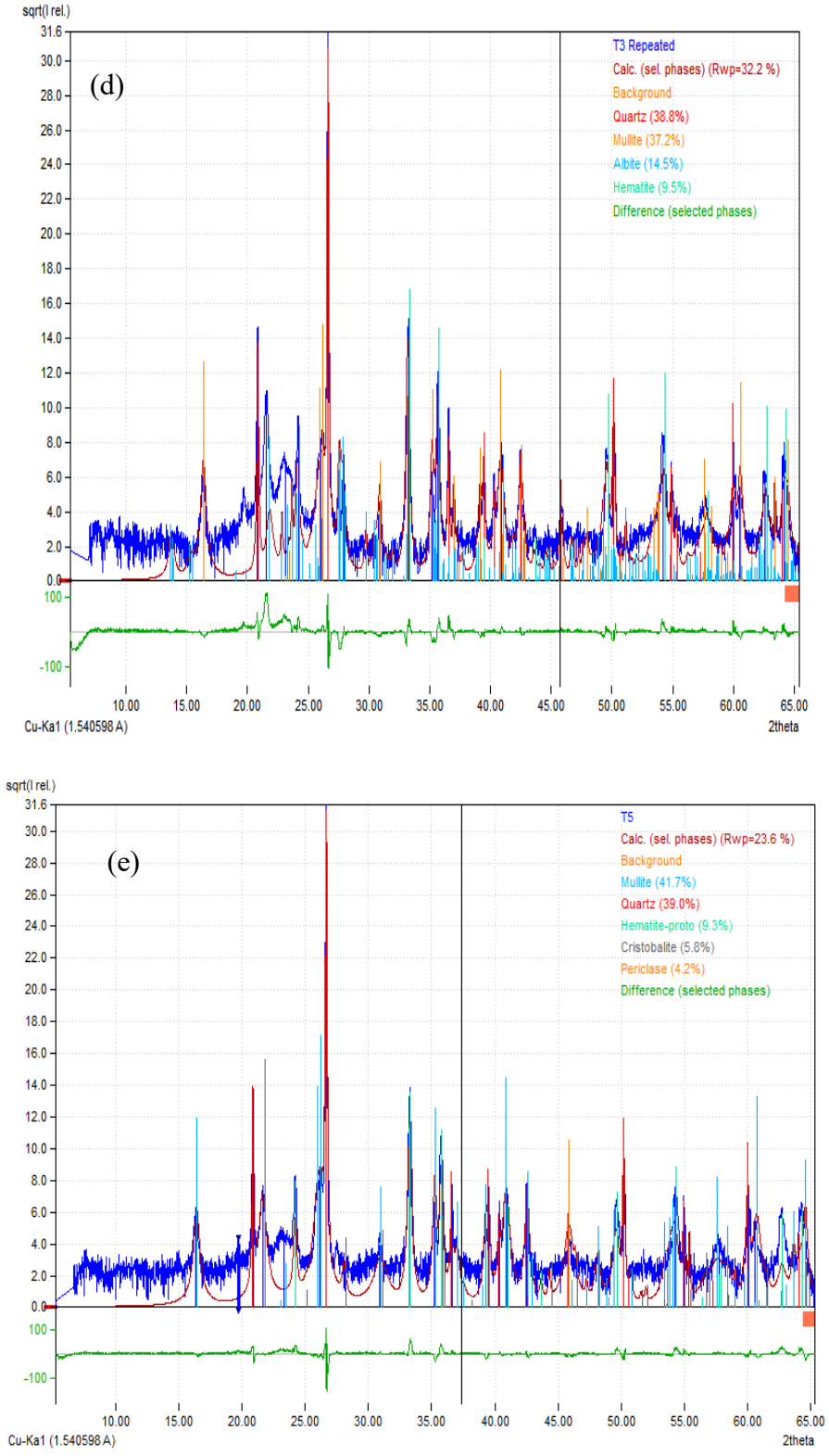

Figure 4. 4: XRD micrographs of sintered tiles at1200 ℃. (a) tile sample with 0 wt % of ferric oxide, (b) tile sample with 10 wt % of ferric oxide, (c) tile sample with 15 wt % of ferric oxide, (d) tile sample with 20 wt % of ferric oxide (e) tile sample with 30 wt % of ferric oxide.

4.6 Experimental Measurements

In this study, the five batches of the tile samples were subjected to a laboratory analysis. This was done to determine the physical properties such as water absorption and linear shrinkage and mechanical properties that included flexural strength and compressive strength.

4.6.1 Flexural Strength

The flexural strength was determined using a three-point loading method described in chapter three section 3.7.4. The raw data used in the determination of flexural strength is presented in Table 4.5. The flexural strength was plotted against the percentage composition of ferric oxide and the results are presented in Figure 4.5. The control sample with 0 wt % ferric oxide recorded a flexural strength of 11.39 MPa, which is relatively low due to the high quartz content (77%) and limited mullite formation (see Figure 4.3). This observation is consistent with findings by Ochen et al., (2021), who reported that excessive quartz reduces mechanical strength due to formation of cracks caused by thermal expansion mismatch between quartz and its surroundings. As ferric oxide content increased to 10 wt %, the flexural strength significantly increased to 43.96 MPa, due to enhanced mullite formation, which is known to reinforce the ceramic matrix. Comparable studies have reported flexural strength values ranging between 35-45 MPa in ceramic bodies with optimized mullite content and reduced quartz fractions (Romero et al., 2021). Beyond 15 wt % ferric oxide, a decline in strength was observed, mirroring results in literature where excessive additives disrupt the mullite matrix or promote glassy phase formation, thus weakening mechanical integrity (Cui et al., 2020). Therefore, the

strength trends reported in this study are consistent with contemporary findings, highlighting the critical role of phase composition particularly the balance between quartz and mullite in determining the flexural performance of sintered ceramics.

Table 4. 5: Flexural strength of the developed tile samples.

Parameter	**Tiles samples**				
	1	**2**	**3**	**4**	**5**
Width (mm)	48.4	50	50	48	50
Thickness (mm)	15	13.2	12.2	12	14
Maximum force (N)	2534	2293	2309	2346	2417
Modulus (MPa)	540.1	22200.2	32602.6	14758.4	1292.5
Flexural Strength (MPa)	11.39	43.96	45.34	38.59	40.32

The formation of mullite crystals as seen in Figure 4.4 increased from 29-41 %, whereas the composition of quartz decreased. Mullite fibres are formed during thermal treatment, typically between 950 °C and 1600 °C, through solid-state reactions or partial melting of alumino-silicate precursors, particularly kaolinite (Mohamed et al., 2024). The formation process begins with dehydroxylation between 450 °C and 650 °C, during which kaolinite loses its structural water and transforms into metakaolinite as per reaction equation 4.1 (Mohamed et al., 2024).

$$Al_2Si_2O_5(OH)_4 \rightarrow Al_2Si_2O_7 + 2H_2O \quad (4.1)$$

According to equation 4.2. according to equation 4.2, amorphous phase

reorganizes into spinel-type structures and amorphous silica when the temperature rises to between 800 °C and 1100 °C.

$$Al_2Si_2O_7 \rightarrow \text{Spinel phase } (\gamma\text{-}Al_2O_3) + 2SiO_2 \text{ (amorphous)} \quad (4.2)$$

Finally, between 1100 °C and 1400 °C, these intermediate phases crystallize to form mullite crystals as shown in the reaction equation 4.3 (Sonuparlak et al., 2005).

$$3Al_2O_3 + 2SiO_2 \rightarrow Al_6Si_2O_{13} \text{ (Mullite)} \quad (4.3)$$

Mullite is highly stable and is characterized by low thermal expansion, making it beneficial for enhancing mechanical strength, thermal shock resistance, and chemical durability in ceramic materials. The presence of mullite fibres increases the strength of ceramic tiles (see Figure 4.5) based on mullite hypothesis. The first hypothesis states that the strength of ceramic products increases with an increase in the mullite population. This is evident in Figure 4.4 and Figure 4.5. The second hypothesis states that the strength of ceramic products increases with the development of fine mullite fibres morphology, as finer fibres enhances better interlocking and densification within the microstructure thus increasing flexural strength (Khater et al., 2024).

The flexural strength values obtained in this study, ranging from 11.39 MPa to 45.34 MPa, are consistent with those reported in recent literature on ceramic materials designed for structural and wall tile applications. At the lower end of the range, the control sample with 0 wt % ferric oxide recorded a flexural strength of 11.39 MPa, which is comparable to values reported in ceramics with high quartz content and poor mullite development. For example, Chen et al.,

(2022) reported flexural strengths as low as 10–15 MPa in bodies composed primarily of quartz and kaolinite, where minimal transformation to mullite occurred during sintering.

Conversely, the highest value in this study (45.34 MPa) aligns well with results from ceramic compositions optimized for mullite formation and reduced glassy or residual quartz phases. Romero et al., (2021**)** and Zhou et al. (2023) observed flexural strength values in the range of 38–47 MPa in ceramic tiles prepared with fluxing agents and sintered at optimized temperatures to maximize mullite crystallization. These studies highlight the strengthening effect of mullite, especially in compositions where quartz content is reduced below 40 %.

Additionally, Gupta and Singh (2021) examined red clay, feldspar, additive systems and reported flexural strengths ranging from 30 to 44 MPa depending on the additive type and sintering conditions. Their results support the conclusion that phase composition specifically the formation of interlocking needle-like mullite crystals plays a crucial role in mechanical reinforcement.

The study by Li et al. (2024) focusing on ferric oxide additions in ceramic bodies showed that strengths increased up to an optimal additive level (~10–15 wt %), beyond which the presence of a glassy phase and structural defects resulted in strength reductions mirroring the trend observed in this research.

The flexural strength values reported in this study are well within the range of values documented by other researchers and reflect widely recognized phase transformation mechanisms. The results reinforce the importance of controlling

quartz and mullite proportions, as well as the role of ferric oxide as a sintering and strengthening agent when used in optimal amounts.

Based on the flexural strength results (38.59 ± 1.9 MPa to 45.34 ± 2.2 MPa) observed in the samples with adequate ferric oxide content and mullite formation, the tiles produced in this study conform to the BIa class under ISO 13006 (Zanelli et al., 2021). This means they are suitable for use as floor tiles, since they also meet the required water absorption limits (≤ 0.5 %) for BIa (Zanelli et al., 2021).

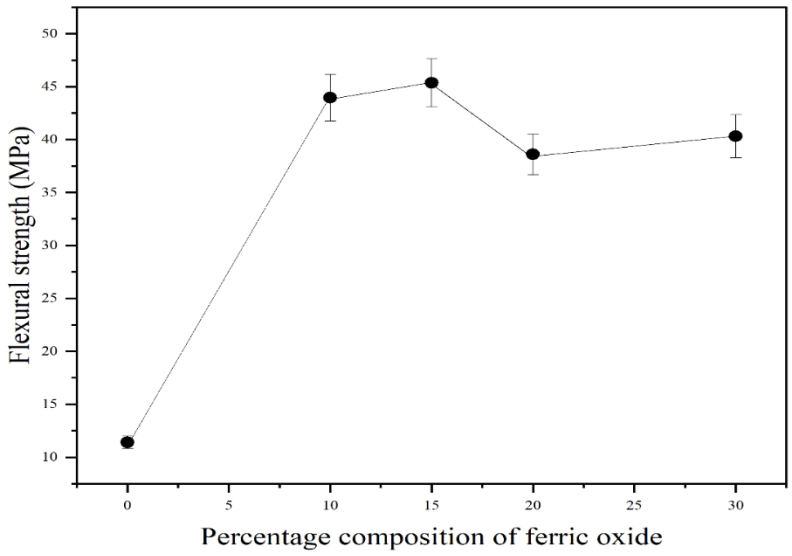

Figure 4. 5: Variation of flexural strength with percentage composition of ferric oxide.

4.6.2 Compressive Strength

The compressive strength of the samples was determined using a compressive testing machine, following the procedure outlined in Chapter 3, Section 3.7.5. The raw data used in the determination of compressive strength is presented in

Table 4.6. The compressive strength was plotted against the percentage composition of ferric oxide and the results are presented in Figure 4.6. The control sample containing 0 wt % ferric oxide exhibited a compressive strength of 52.3 MPa. Upon increasing the ferric oxide content to 10 wt %, there was a noticeable increase in compressive strength to 54.9 MPa, suggesting enhanced densification and microstructural development, likely due to the formation of stronger bonding phases such as mullite (Zawrah et al., 2016; Zhang et al., 2020). At 15 wt % ferric oxide, there was no clear correlation between ferric oxide content and compressive strength, as shown in Figure 4.6. In general, no consistent correlation was found between compressive strength and ferric oxide content in the tile samples at higher concentrations of ferric oxide.

Table 4. 6: Compressive strength of the developed tile samples.

Parameter	**Tiles samples**				
	1	**2**	**3**	**4**	**5**
Length (mm)	52.11	51.00	52.36	51.63	51.71
Width (mm)	49.81	49.95	49.43	51.21	50.51
Load at failure (kN)	178.5	149.3	122.6	117.0	130.33
Average compressive strength (MPa)	52.34	54.93	41.2	44.3	50.27

The compressive strength values obtained in this study, ranging from 41.2 MPa to 54.93 MPa, fall within the typical range for structural ceramics and ceramic tiles developed for moderate to high mechanical performance. The lowest value of 41.2 MPa is consistent with ceramic bodies having higher porosity or limited crystalline phase development. Wang et al., (2022) reported compressive strength values of 38–45 MPa in red clay, feldspar ceramic composites sintered

at moderate temperatures, where incomplete densification and residual quartz were contributing factors to reduced strength. The highest value of 54.93 MPa compares with high-performance ceramic formulations. Zhou et al., (2023) achieved compressive strengths of 50–60 MPa in feldspathic ceramic bodies optimized for mullite formation and low porosity.

Similarly, Ali et al., (2021) reported compressive strength values in the range of 48–55 MPa in iron oxide-doped porcelain ceramics, noting that controlled ferric oxide additions enhance densification and grain bonding, provided they are within an optimal range (typically 5–15 wt %).

Das and Mandal et al., (2024) demonstrated that ceramic materials incorporating fluxing agents and sintered at temperatures around 1200–1250 °C can exhibit compressive strengths exceeding 52 MPa**,** especially when a fine-grained microstructure and well-distributed mullite phase are achieved.

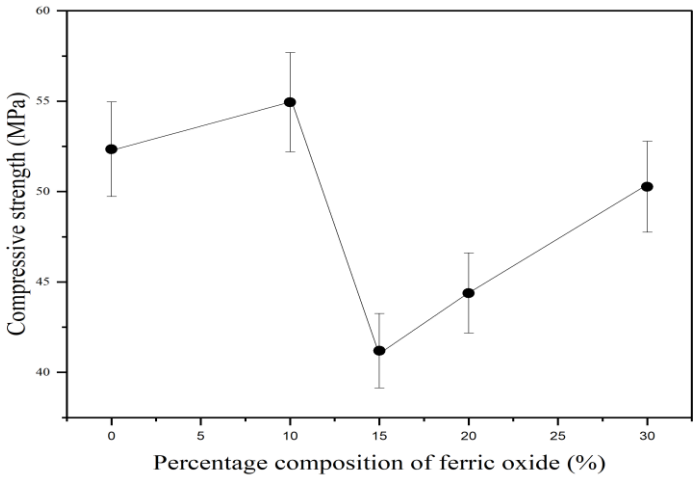

Figure 4. 6: Variation of compressive strength with percentage composition of ferric oxide.

4.6.3 Water Absorption

The water absorption capacity of the samples was evaluated using ASTM C373-88 method, as detailed in Chapter 3, Section 3.7.2. The results, presented in Figure 4.7, were analyzed based on the varying ferric oxide content, the raw data obtained can be found in Table 4.7. The control sample, which contained 0 wt % ferric oxide, exhibited a water absorption capacity of 11.7 %. This relatively high value is attributed to the presence of a substantial amount of undissolved quartz (77 %) (See Figure 4.3a). Quartz is a stable crystalline phase that does not significantly participate in the vitrification process, thus leading to the formation of open pores and grain boundaries that increase water absorption. The presence of quartz also increases cracks due to residual stresses resulting in high water absorption. Similar findings have been reported by Azevedo et al. (2017), who noted that high quartz content in ceramic bodies can result in elevated porosity and water uptake due to insufficient sintering reactions.

Table 4. 7: Water absorption of the developed tile samples.

Parameter	**Tiles samples**				
	1	**2**	**3**	**4**	**5**
Average mass of the fired sample, M_f (g)	129.06	112.93	105.83	106.3	109.46
Average mass of saturated sample, M_s (g)	143.87	124.18	115.8	116.91	121.76
Average water absorption	11.77	9.99	9.62	10.01	11.24

The addition of 10 wt % ferric oxide led to a significant reduction in water absorption to 9.9 %, as shown in Figure 4.7. This trend is consistent with studies by Zhang et al. (2019) and Zawrah et al. (2016), who observed that iron oxide,

can act as a fluxing agent during sintering, promoting the formation of mullite and enhancing the densification of the ceramic matrix. The denser microstructure effectively reduces open porosity, thereby limiting water absorption. Further increase to 15 wt % ferric oxide yielded a slightly lower water absorption value of 9.62 %, indicating continued improvement in densification.

However, a further increase in ferric oxide (20–30 wt %) resulted in an increase in water absorption. This can be attributed to the formation of a porous microstructure due to the presence of high levels of iron oxide, which disrupt vitrification and create micro cracks or intergranular pores during firing (Li et al., 2021).

The ISO 13006 Standard classify tiles whose water absorption is in a range of 6-10% as class BII_b (Zanelli et al., 2021). In this study, tile samples containing ferric oxide, in a range of 10 -20 wt %, 10 -20 wt % feldspar, 10 wt % sand, 40 wt % kaolin, 20 wt % ball clay satisfied the ISO 13006 standard for water absorption hence they are classified as BII_b wall tiles.

Comparable studies have reported similar water absorption capacities depending on the ceramic composition and firing conditions. For example, Romero et al., (2021) reported water absorption values ranging from 7.5 % to 10.2 % in ceramic tiles made from red clays and fluxing agents, noting that absorption decreased with increased vitrification and mullite content.

Zhou et al., (2023) found that ceramics doped with 10–15 wt % ferric oxide and sintered at optimal temperatures exhibited water absorption values between 8 % and 9.5 %, attributing this to improved densification and reduced open porosity.

Abdelrahman et al., (2022) investigated kaolin–feldspar–quartz bodies and reported water absorption values between 10.0 % and 12.3 %, particularly in compositions with high quartz and incomplete vitrification, which closely resembles your results.

Li et al., (2024) emphasized that water absorption above 10 % is typical in compositions with excess quartz or insufficient flux, which hampers liquid-phase sintering and promotes residual porosity.

These findings suggest that the tile samples fall within the expected range for moderately vitrified ceramics, although slightly exceeding the ideal range for some commercial wall tile standards. The results further underscore the importance of optimizing the quartz to mullite ratio, firing temperature, and ferric oxide content to reduce open porosity and enhance ceramic quality.

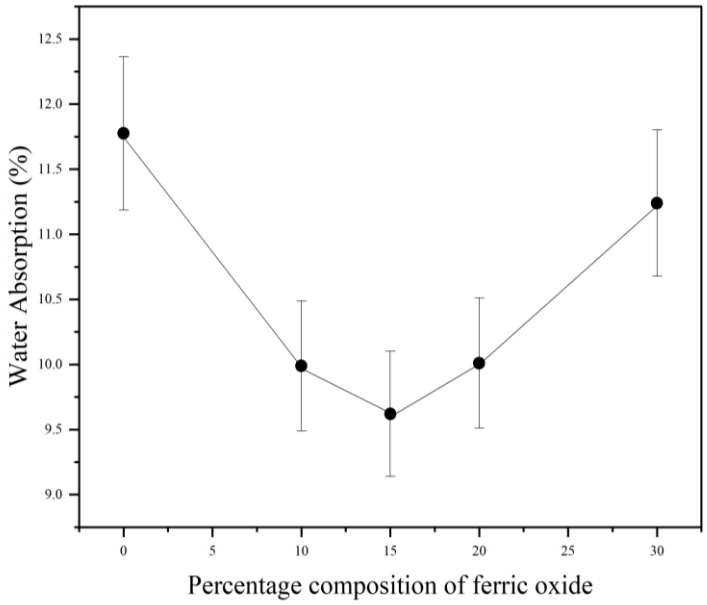

Figure 4. 7: Variation of water absorption capacity with percentage composition of ferric oxide.

4.6.4 Linear Shrinkage

The linear shrinkage of the samples was assessed using the ASTM C373-88 standard method, as described in Chapter 3, Section 3.7.1. The results illustrated in Figure 4.8 and Table 4.8 demonstrate the influence of ferric oxide content on the shrinkage behavior of ceramic tiles. The control sample, with 0 wt % ferric oxide, exhibited the highest linear shrinkage of 1.01%. This elevated shrinkage is primarily attributed to the high quartz content (77 %) and the presence of open pores, as confirmed by SEM and XRD analysis (see Figures 4.2 and 4.3). Quartz, being a thermally stable crystalline phase that resists vitrification, contributes to grain boundary development and leaves unfilled pore spaces, thereby increasing dimensional contraction during firing. Similar observations have been reported by Das et al. (2005) and De Noni et al. (2009), who noted that higher quartz content correlates with increased shrinkage due to poor sintering response and

retained porosity. The absence of mullite in the control sample further impaired densification, hence affecting the linear shrinkage.

Table 4. 8: Linear shrinkage percentages of the tile samples.

Parameter	**Tiles samples**				
	1	**2**	**3**	**4**	**5**
Average length of dry sample (cm)	10.81	10.56	10.58	10.52	10.52
Average length of fired sample	10.71	10.5	10.52	10.47	10.46
Average linear shrinkage (%)	1.01	0.85	0.59	0.46	0.52

The introduction of 10 wt % ferric oxide reduced shrinkage to 0.85 %, which can be attributed to the onset of mullite formation catalyzed by ferric oxide. This finding aligns with studies by Martín-Márquez et al. (2010) and Saponjic et al. (2024), who demonstrated that ferric oxide enhances the formation of mullite during firing, leading to improved particle bonding, reduced pore volume, and more stable microstructures. At 15 wt % ferric oxide, shrinkage dropped further to 0.59 %, indicating more efficient vitrification and optimal mullite content that promoted structural consolidation with minimal volumetric change consistent with the conclusions drawn by Raut et al. (2018), who emphasized the role of mullite in controlling dimensional stability during sintering.

A further decline in shrinkage to 0.46 % at 20 wt % ferric oxide marks the lowest shrinkage observed across all compositions, reflecting peak microstructural densification and minimal open porosity. This is in agreement with findings by Mankai et al. (2018), who reported that optimal mullite formation enhances ceramic body stability by minimizing shrinkage through pore closure and phase

uniformity. However, at 30 wt % ferric oxide, a moderate increase in shrinkage to 0.53% was observed. This reversal may be attributed to excessive ferric oxide interfering with the fluxing action of feldspar, a critical phase for vitrification. Similar shrinkage inconsistencies have been observed by Obolkina et al., (2020), who noted that overloading certain additives can disrupt sintering phase balance, hinder glass phase formation, and ultimately affect densification.

The linear shrinkage values obtained in this study, ranging from 0.46 % to 1.01 %**,** are relatively lower than the typical range reported in recent literature for clay-based ceramics, which often exhibit shrinkage between 2 % and 8 %, depending on raw material composition, firing temperature, and fluxing agent content. Several recent studies have documented higher linear shrinkage levels, attributing them to higher plasticity, glassy phase formation, and enhanced sintering.

Accordingly, Li et al., (2024) observed that linear shrinkage below 1 % typically occurs in ceramic bodies with excess quartz or insufficient vitrification, as quartz acts as a rigid filler that resists sintering contraction, a phenomenon consistent with the observation of high quartz content (~77 %) in the control sample.

Abdelrahman et al., (2022) reported that ceramic tiles formulated with kaolin, feldspar, and quartz showed shrinkage values of 2.5 % to 5.5 %**,** with higher values corresponding to increased mullite formation and reduced quartz content.

Therefore, the low shrinkage values (0.46 %–1.01 %) reported in this study reflect a dominance of quartz and suboptimal sintering temperatures. These

characteristics inhibit significant particle rearrangement and densification, resulting in minimal dimensional change.

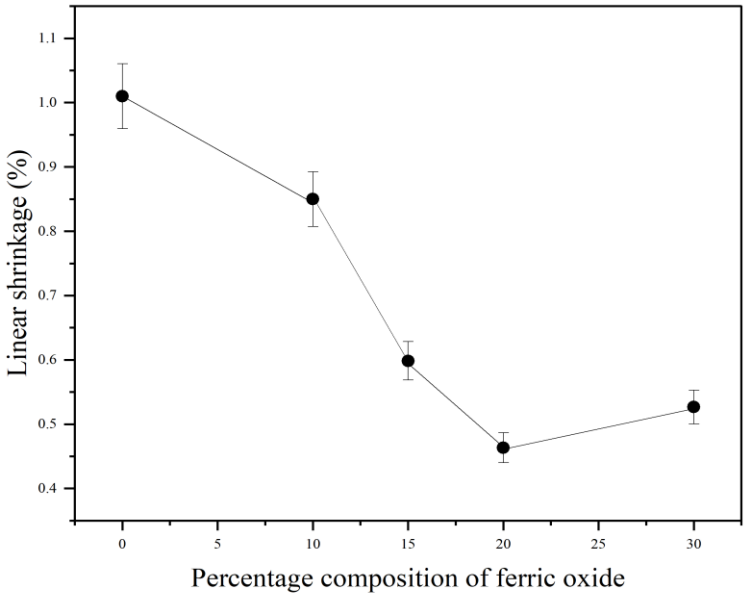

Figure 4. 8: Variation of linear shrinkage with composition of ferric oxide.

4.7 Optimization Using Design Expert Software

The optimal mixing proportions of feldspar and ferric oxide that generated the best mechanical properties were studied and the results are shown in Table 4.9. As observed, seven (07) experimental runs were configured, with ferric oxide and feldspar varied within the range of 0–30 wt %. The other factors (sand, ball clay, and kaolin) were kept constant throughout the study. The responses evaluated included flexural strength, compressive strength, water absorption, and linear shrinkage. The results from optimization show that the best sample formulation requires a high percentage composition of ferric oxide especially when targeting improved flexural strength, water absorption, linear shrinkage and compressive strength.

Table 4. 9: Factors and their responses in the design matrix.

Run	Factors					Responses			
	Ferric Oxide (%)	Feldspar (%)	Ball Clay (%)	Sand (%)	Kaolin (%)	Flexural Strength (MPa)	Compressive strength (MPa)	Water Absorption (%)	Linear shrinkage (%)
1	0	30	20	10	40	41.6564	81.556	10.3780	1.7246
2	5	25	20	10	40	40.9231	56.8757	10.3457	0.9896
3	10	20	20	10	40	40.2996	56.6285	10.3178	0.6163
4	15	15	20	10	40	38.6458	56.6285	9.2452	0.806
5	20	10	20	10	40	41.6698	59.1169	10.3178	0.6965
6	25	5	20	10	40	40.903	56.8187	10.4324	0.9178
7	30	0	20	10	40	41.6675	56.6285	10.5562	1.7246

4.7.1 Optimization of Flexural Strength

The experimental data of flexural strength was subjected to Response Surface Methodology (RSM) tool in design expert 13 software, as described in Chapter 3, Section 3.9. Design Expert Software 13 recommended a quadratic model for the experiment. The sequential model sum of squares and model summary statistics were utilized to examine the flexural strength (FS) response. This produced a quadratic model with an F-value of 4.83, which was significant because the p-value was less than 0.05.

Equation 4.4 shows the final regression function for the FS in terms of the coded components used to create the statistical model.

$$FS=37.01+0.0853A-0.2595B+4.20AB+2.93A^2+3.83B^2, \quad (4.4)$$

where A is the % composition of ferric oxide and B is the % composition of feldspar.

The optimization process of flexural strength indicated that the highest value of flexural strength among the tile samples was 41.6 MPa from the formulation containing 20 wt % of ferric oxide, 10 wt % feldspar, 20 wt % ball clay, 10 wt % sand and 40 wt % kaolin. This is validated by experimental results where a flexural strength of 45.34 MPa was obtained by samples containing 15 wt % ferric oxide, 15 wt % feldspar, 20 wt % ball clay, 40 wt % kaolin and 10 wt % sand. This aligns with Awais et al., (2024) who highlighted a positive trend between ferric oxide and flexural strength. This further confirms that increasing the percentage composition of ferric oxide enhances the flexural strength of tiles. The increase in the flexural strength is attributed to the formation of the mullite fibres as discussed earlier.

The statistical significance of the quadratic models, the lack of fits, and the statistical significance of the model coefficients were all evaluated using ANOVA. A model F-value of 4.83 in Table 4.11 indicates significant results (p-values < 0.05). This suggests that the likelihood of a model F value of this magnitude occurring due to noise is only 0.01%.The quadratic model accurately depicts the functional connection between the experimental factors and response variables, as evidenced by a significant lack of fit (p-value < 0.05). The percentage of ferric oxide and feldspar with a value of $p > 0.05$ shows that the errors were abnormally distributed, and the residual plots were reasonably not excellent. This confirms the association between the percentage of ferric oxide

and the flexural strength FS exhibited in Figure 4.9. Figure 4.9 (a) depicts a plot of studentized residuals versus run of the data for flexural strength. The diagnostic plots for flexural strength show a reliable model. The normal plots of residuals in Figure 4.9 (b) show points that are closely matched with the straight line, indicating a normal error distribution, with an R2 value of 0.7753. The residuals vs expected plot in Figure 4.9 (c) shows a random dispersion around zero, indicating consistent variance and a reasonable model fit (standard error = 0.3228). To assess the model's appropriateness, real vs expected data revealed tendencies in linear regression fit, with no discrepancy between predicted and actual acquired values. The predicted vs. real plots show values clustering near the diagonal, with a moderate validation error of 7.45%, indicating the model's trustworthiness. Overall, the model successfully guided the development of optimal formulations for optimizing flexural strength, resulting in a highly desirable product.

Table 4. 10: Fit statistics for flexural strength.

Std. Dev	**2.92**	**R^2**	**0.7753**
Mean	41.7	Adjusted R^2	0.6148
CV %	7.00	Predicted R^2	-0.4655
		Adq. Precision	6.1677

Table 4.11 reveals that the model's F-Value is 4.83, indicating that it is significant. An F-value this high has a 3.13% probability of being caused by noise. Model terms are considered significant if the P-value is less than 0.0500. AB and B^2 are significant model terms in this instance. The model terms are not important if the value is larger than 0.1000. Model reduction may be significant if the model has a large number of redundant terms.

The lack of fit of 11.23 suggests that it is remarkable. There is a 2.04% chance that this significant lack of fit value is caused by noise. This means that the model won't fit. The overall mean may be a more accurate predictor of the response than the current model, as indicated by a negative predicted R2 (Table 4.10). The signal-to-noise ratio is measured by Adq.precision. It is preferred to have a value greater than 4. The model can be used to investigate the design space, and the signal value of 6.1677 is suitable for this study.

Table 4. 11: ANOVA for Quadratic model for Flexural strength.

Source	**Sum of squares**	**df**	**Mean square**	**F-value**	**P-value**	
Model	205.51	5	41.10	4.83	0.0313	significant
A-Ferric oxide	2.62	1	2.62	0.3084	0.5960	
B-Feldspar	6.34	1	6.34	0.7453	0.4166	
AB	108.98	1	108.98	12.81	0.0090	
A^2	16.52	1	16.52	1.94	0.2062	
B^2	78.98	1	78.98	9.28	0.0187	
Residual	59.56	7	8.51			
Lack of fit	53.24	3	17.75	11.23	0.0204	significant
Pure error	6.32	4	1.58			

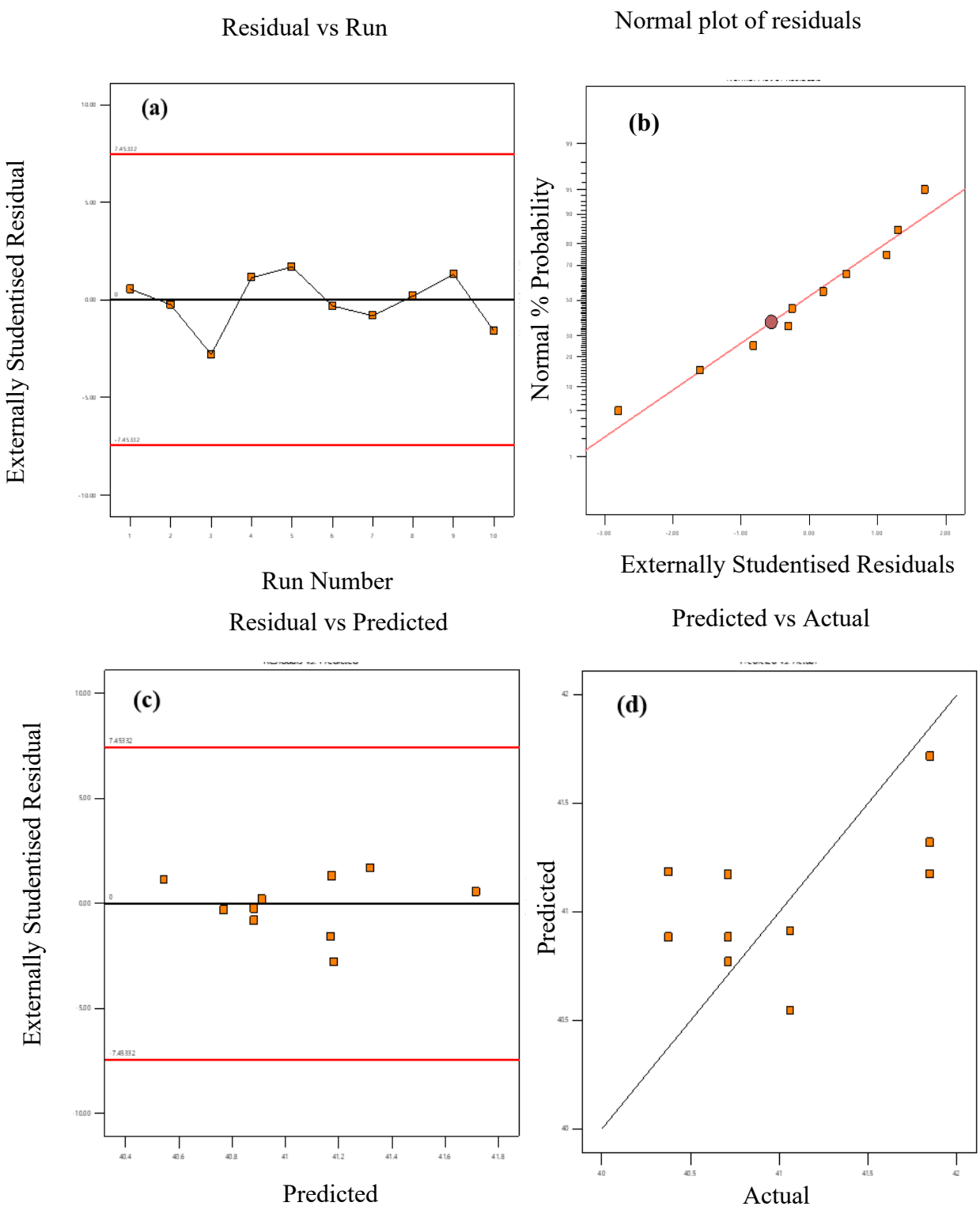

Figure 4. 9: Flexural strength plots of (a) Normal probability vs external studentised residual, (b) Externally studentised residual vs Predicted response, (c) Residual vs run number, and (d) Predicted vs actual values.

4.7.2 Compressive Strength Optimization

According to the guidelines on ceramic materials and predictive modeling (ASTM C67-23; ASTM C373-18). The predictive model's compressive strength optimization revealed that the tile samples with the maximum compressive strength (20 wt% feldspar, 10 wt% ferric oxide, 20 wt% ball clay, 40 wt% kaolin, and 10 wt% sand) had a strength of 48.05 MPa, as shown in Figure 4.2.The maximum experimental compressive strength recorded was 54.93 MPa for the same composition. The predictive model shows a deviation of 4.6 %. This minimal difference indicates that the model effectively represents the material's behavior at this composition. The development of mullite crystals, which improve the mechanical performance of ceramic bodies by enhancing liquid-phase sintering and fortifying particle attachment, is responsible for the observed increase in compressive strength (Olanrewaju & Afolabi, 2024).

The diagnostic plots of compressive strength suggest a lower model fit accuracy as normal residuals plot in Figure 4.9 (a) indicates slight deviation from linearity, indicating mild abnormality. The residuals vs predicted plot in Figure 4.9 (b) shows uneven variance likely due to formation of mullite fibers after sintering. The residuals vs run plot in Figure 4.9 (c) also indicate some inconsistency, possibly because of experimental variation. Figure 4.9 (d) shows predicted vs actual plot and indicates a lot of scatter with an error value of 47 %, an indication that the model slightly under estimated the actual values.

The model's F-value of 4.71 in Table 4.13 indicates that it is significant. P-values less than 0.0500 show that the model terms are significant; in this case, B^2 is an important model term; values greater than 0.0100 suggest that the model terms

are insignificant; if the model contains a large number of irrelevant terms, model reduction may improve it. There is only a 3.33% chance that an F-value this large will occur due to noise. The F-value of 0.04 indicates that the lack of fit is not statistically significant in comparison to the pure error. This lack of fit error is most likely caused by noise, with a 98.6% probability. A non-significant lack of fit is good; therefore, the model is fit.

Table 4.12 demonstrates that the adjusted R^2 of 0.6071 and the expected value R2 of 0.7708 are reasonably in alignment. The signal-to-noise ratio is the measure of precision. A ratio of 5.39 indicates a strong signal since any ratio greater than 4 is preferred. This model facilitates the exploration of the design space.

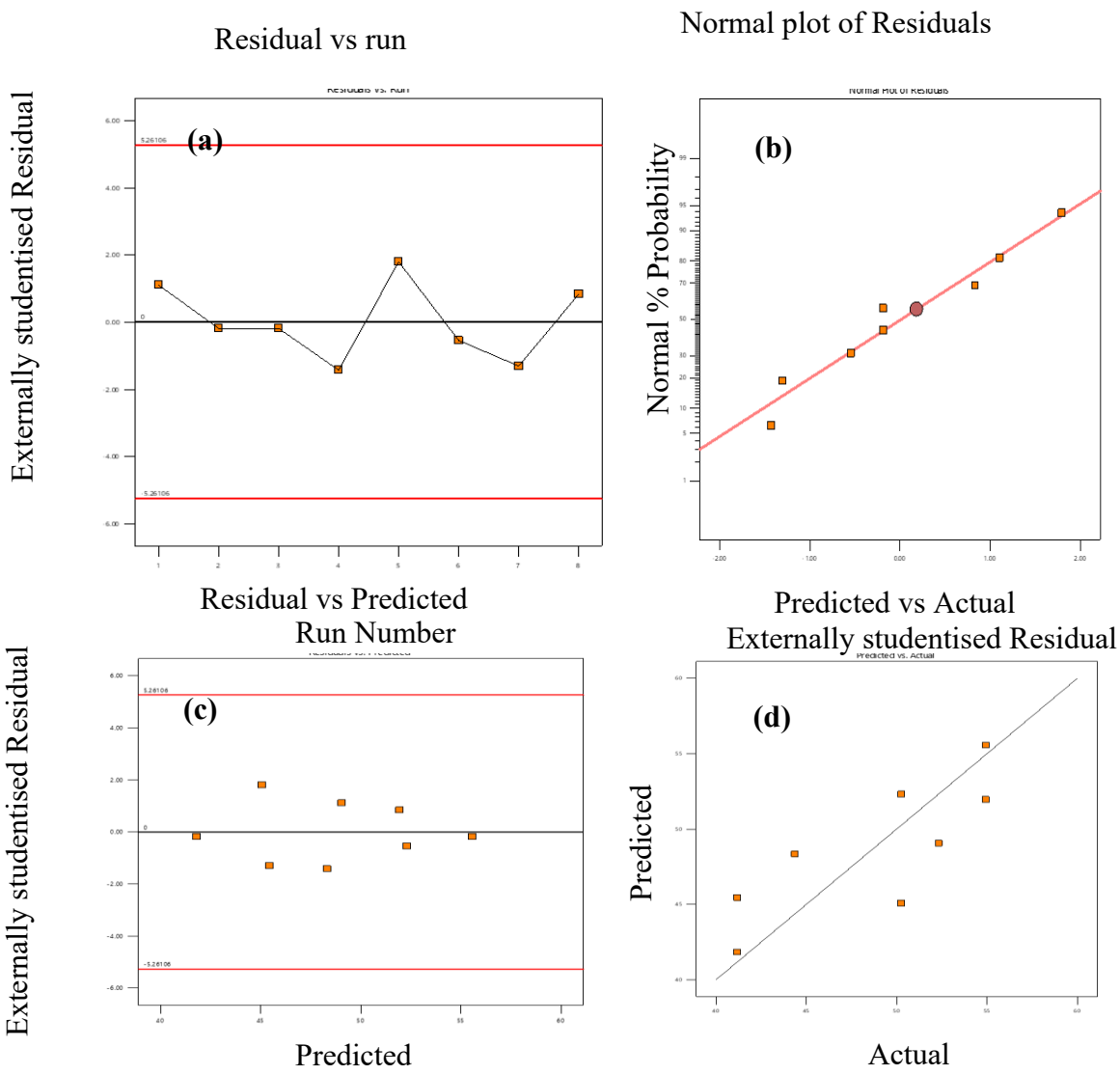

Figure 4. 9: Compressive strength plots of (a) Residual vs run, (b) Normal probability vs external studentised residual, (c) externally studentised residual vs predicted response, and (d) predicted vs actual values.

Table 4. 12: Fit statistics for compressive strength.

Std. Dev	**16.37**	**R^2**	**0.7708**
Mean	56.63	Adjusted R^2	0.6071
CV %	28.91	Predicted R^2	0.6045
		Adq. Precision	5.3998

Table 4. 13: ANOVA for Quadratic model for Compressive strength.

1	**Sum of squares**	**df**	**Mean square**	**F-value**	**P-value**	
Model	6308.25	5	1261.65	4.71	0.0333	significant
A-Ferric oxide	297.85	1	297.85	1.11	0.3268	
B-Feldspar	256.29	1	256.29	0.9565	0.3607	
AB	172.92	1	172.92	0.6453	0.4482	
A^2	1459.56	1	1459.56	5.45	0.0523	
B^2	4710.71	1	4710.71	17.58	0.0041	
Residual	1875.66	7	267.95			
Lack of fit	55.15	3	18.38	0.0404	0.9876	Not significant
Pure error	1820.51	4	455.13			

4.7.3 Optimization of Water Absorption

The statistical analysis of the water absorption response indicates a good model. The normal probability plot of residuals (Figure 4.10 a) displays a near-linear distribution, confirming the assumption of normality. The residuals vs. predicted values plot (Figure 4.10 b) shows minimal scatter, suggesting a stable variance across the predicted range. Additionally, the residuals vs. run plot (Figure 4.10 c) exhibits a consistent pattern with low scatter, indicating that the experimental runs were stable and reproducible.

However, the predicted vs actual plot (Figure 4.10 d) reveals a notable discrepancy, with the model predicting a water absorption of 10.69 %, diverging from some of the actual experimental values. Despite this deviation, the model successfully identified the optimal formulation with the lowest observed water absorption value of 9.62 %, corresponding to a composition of 20 wt % ferric oxide, 10 wt % feldspar, 20 wt % ball clay, 10 wt % sand, and 40 wt % kaolin.

This result suggests that increasing ferric oxide content effectively reduces water absorption, due to enhanced vitrification during sintering. The presence of ferric oxide promotes liquid phase sintering, which reduces porosity through the development of a glassy phase. These findings align with the observations of Khattab et al., (2022), who reported that ferric oxide facilitates mullite formation, contributing to densification and a subsequent reduction in water absorption capacity.

When compared to noise, the model's F-value of 4.42 in Table 4.15 indicates that it is not statistically significant. Noise has a 19.48% probability of causing a high F-value. As shown in Table 4.15, P-values less than 0.0500 suggest that the model terms are significant. There are no model terms in this instance. The model terms are considered insignificant if the value is more than 0.0100. Model reduction may make the model better if it has a significant number of redundant terms.

Table 4.14 shows a projected R2 of -1.0489, which is relatively consistent with the Adjusted R2 of - 0.3028. A quadratic model with a sequential p-value of 0.0962 is evaluated.

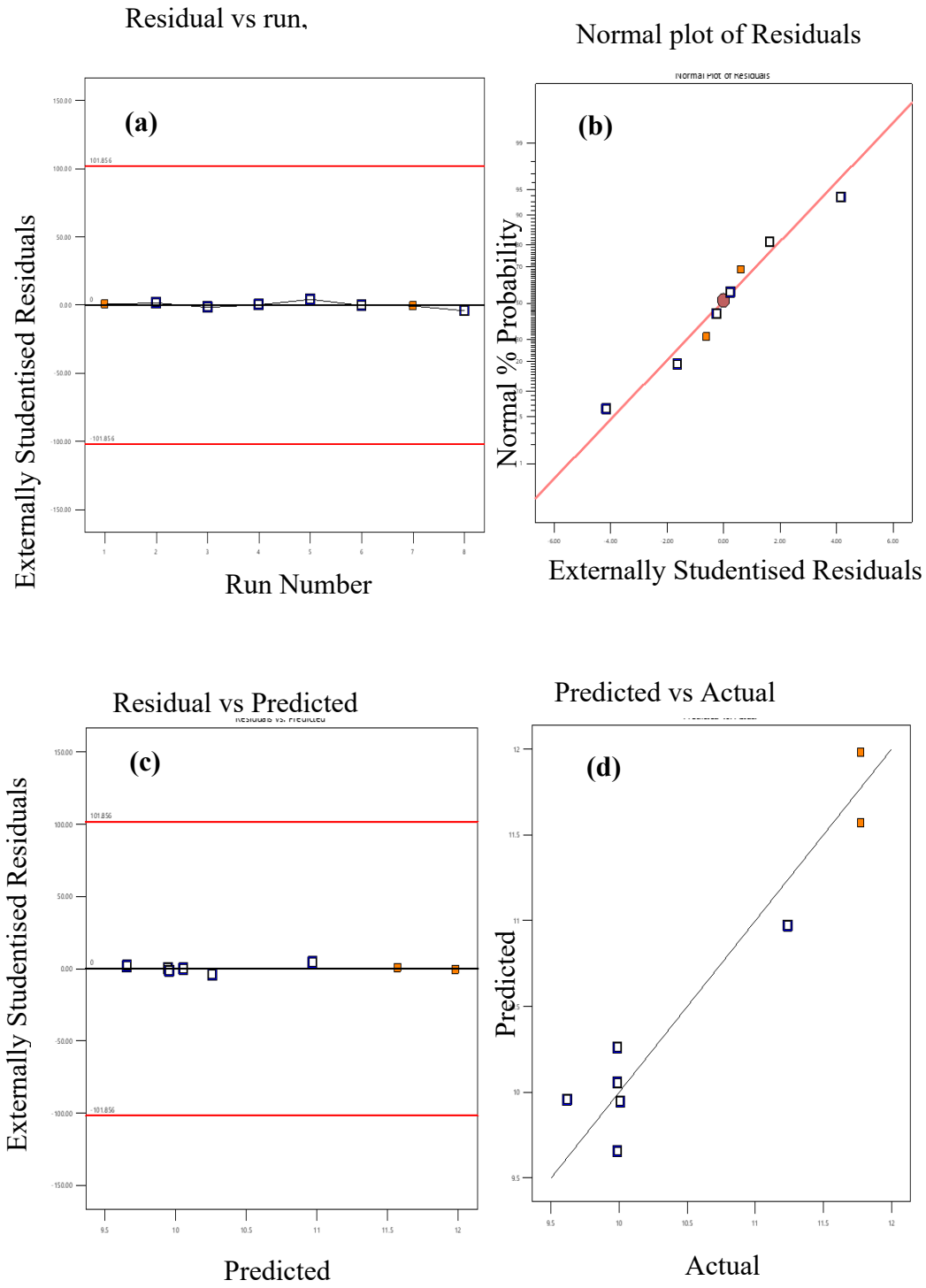

Figure 4. 10: Compressive strength plots of (a) Residual vs run, (b) Normal probability vs external studentised residual, (c) externally studentised residual vs predicted response, and (d) predicted vs actual values.

Table 4. 14: Fit statistics for compressive strength.

Source	Sequential p-value	Adjusted R^2	Predicted R^2	
linear	0.8353	-0.3028	-1.0489	
2FI	0.6048	-0.5097	-1.3972	
Quadratic	0.0962	0.7095	-0.4942	suggested

Table 4. 15: ANOVA for quadratic model for water absorption.

Source	Sum of squares	df	Mean square	F-value	P-value	
Model	5.11	5	1.02	4.42	0.1948	Not significant
A-Water Absorption	0.1350	1	0.1350	0.5835	0.5248	
B-Ferric oxide	0.2522	1	0.2522	1.09	0.4061	
AB	0.3782	1	0.3782	1.63	0.3294	
A^2	2.87	1	2.87	12.41	0.0720	
B^2	0.3367	1	0.3367	1.46	0.3510	

4.7.4 Linear Shrinkage Optimization

The Linear shrinkage data from the experiment was subjected to Response Surface Methodology (RSM) tool in design expert 13 software, as described in Chapter 3, Section 3.8. Design Expert Software 13 suggested a quadratic model for the experiment with a sequential p-value of 0.0557 as shown in Table 4.17.

To investigate this response, a sequential model sum of squares and model summary statistics, as shown in Table 4.17, were examined, resulting in a quadratic model with an F-value of 9.70 and a significant p-value of 0.0047. The model is significant because the p-value was less than 0.05.

Normal plot of residuals in Figure 4.11 (a) shows a linear distribution of plots thus supporting the model's assumptions in the analysis of linear shrinkage. The residuals vs predicted plots in Figure 4.11 (b) and residuals vs run plots in Figure 4.11 (c) both show near linear distribution of the plots thus confirming consistency in conducting the experiments. In Figure 4.11 (d) where predicted is plotted against actual displays a close alignment with the diagonal line and the model had an error of 3 %. This confirms that the model captured the trends correctly thus making it important determining the correct linear shrinkage values. The lowest linear shrinkage value from the experiment was recorded as 0.46 %, compared to the model's predicted value of 0.735 %. This confirms that the trends in model prediction were accurately captured. This is noticeable in a composition of feldspar at 15 wt % and ferric oxide at 15 wt %, 20 wt % ball clay, 40 wt % kaolin and 10 wt % sand. This confirms that having equal proportions of feldspar and ferric oxide further improves the linear shrinkage of tile samples aligning with the findings of Jayaweera et al., 2024.

Table 4.17 shows a model F-value of 9.70, indicating that the model is significant. There is only a 0.47% chance that a significant F-value will occur owing to noise. P-values less than 0.0500 indicate that the model terms are significant, as shown in Table 4.17. In this scenario, A, AB, and B^2 are important model terms.

Values greater than 0.0100 imply that the model terms are insignificant. If the model has a large number of irrelevant terms, model reduction may help it. The F-value of 0.32 indicates that the lack of fit is statistically insignificant when

compared to pure error. This lack of fit error is 81.5% likely to be due to noise. A non-significant lack of fit is desirable; therefore, the model is fit.

Table 4.16 shows that the expected R^2 of 0.6690 is similar to the adjusted R2 of 0.7837. The difference is less than 0.2 Adq. Precision is defined as the signal-to-noise ratio. Any ratio higher than 4 is excellent, hence 10.7841 suggests a strong signal. This model can help you explore the design space.

Table 4. 16: Fit statistics for linear shrinkage.

Std. Dev	**0.2278**	**R^2**	**0.8738**
Mean	0.6965	Adjusted R^2	0.7837
CV %	32.70	Predicted R^2	0.6690
		Adq. Precision	10.7841

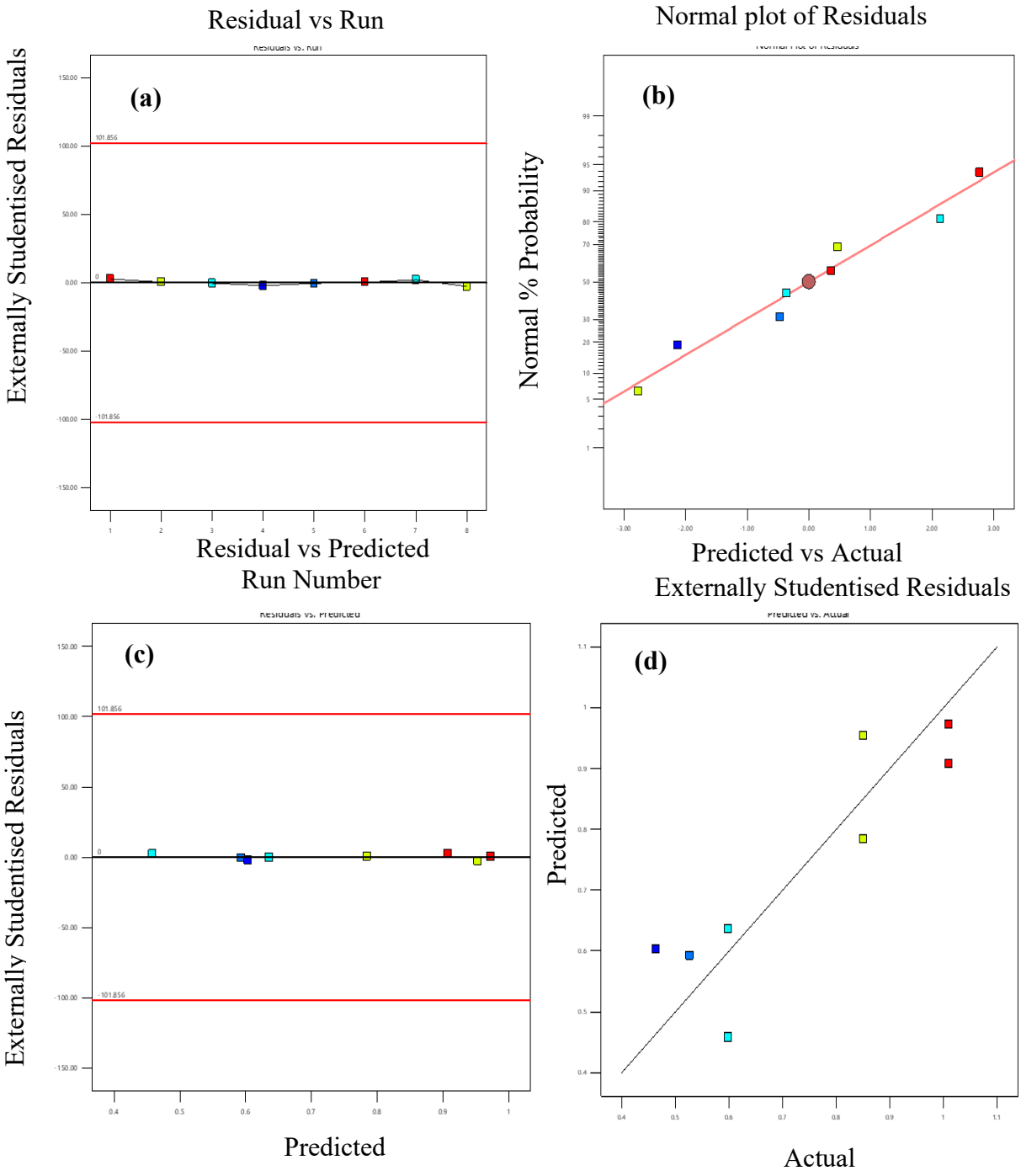

Figure 4. 11: Linear shrinkage plots (a) Normal probability vs external studentized residual, (b) externally studentized residual vs predicted response, (c) residual vs run, and (d) predicted vs actual values.

Table 4. 17: ANOVA for quadratic model for linear shrinkage.

Source	**Sum of squares**	**df**	**Mean square**	**F-value**	**P-value**	
Model	2.52	5	0.5030	9.70	0.0047	significant
A-Ferric oxide	0.3506	1	0.3506	6.76	0.0354	
B-Feldspar	0.1363	1	0.1363	2.63	0.1491	
AB	1.56	1	1.56	30.12	0.0009	
A^2	0.3593	1	0.3593	6.92	0.0338	
B^2	0.1613	1	0.1613	3.11	0.1213	
Residual	0.3631	7	0.0519			
Lack of fit	0.0694	3	0.0231	0.3151	0.8150	Not significant
Pure error	0.2937	4	0.0734			

4.7.5 Validation of the Model

The experimental data presented in Table 4.18, was used to validate the predictive model. Figure 4.12 illustrates the relationship between the model predictions and the experimental results for both the mechanical and physical properties of the tiles. The model underestimated the flexural strength by 8.2 %, which is a relatively minor deviation, indicating that it performs reasonably well in predicting this property. Similarly, it underestimated the compressive strength by 12.5 %, a slightly larger margin that suggests the model may not fully account for all factors influencing this response. In contrast, the model overestimated water absorption by 11.12 %. Although this shows a general alignment with the trend, the negative deviation implies that the actual material absorbed less water

than predicted, potentially reflecting better performance. However, the model significantly overestimated linear shrinkage by approximately 60 %, a substantial deviation that points to a limitation in accurately predicting dimensional changes during processing. Such a discrepancy could impact product design and dimensional tolerance.

Table 4. 18: Validation of the model.

1	Response	Value predicted by the model	Real value of the experiment	Percentage Difference %
1	Flexural strength (MPa)	41.6	45.34	8.2
2	Compressive strength (MPa)	48.05	54.93	12.5
3	Water Absorption (%)	10.69	9.62	-11.12
4	Linear shrinkage (%)	0.735	0.46	-59.7

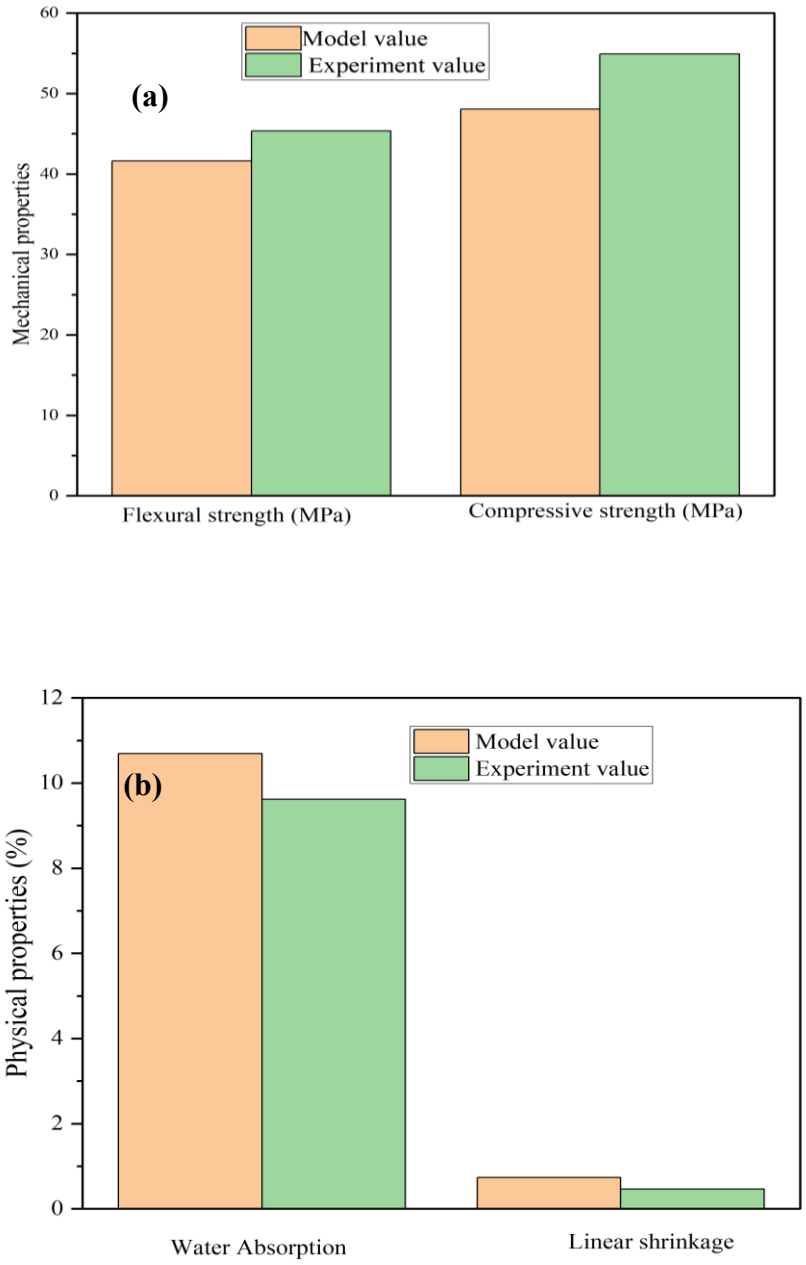

Figure 4. 12: Graphs for Validation of the model for (a) flexural strength and compressive strength values, (b) water absorption and linear shrinkage values.

CHAPTER FIVE: CONCLUSIONS AND RECOMMENDATIONS

5.1 Conclusions

In this study, the use of ferric oxide as a replacement of feldspar in ceramic tiles was explored. The tiles were evaluated based on the physical and mechanical properties. The mechanical properties such as flexural strength and compression strength were determined using the Universal testing machine and the compression testing machine respectively while physical properties such as water absorption and linear shrinkage of the fired products were analyzed using the ASTM C373-88 method. In addition, the morphology and the phase evolution of the fired tiles was evaluated using SEM and XRD methods respectively. The results revealed that increasing the amount of ferric oxide resulted in an increase in the flexural strength of the tiles. This was attributed to the formation of mullite fibres in the fired samples as corroborated by the SEM and XRD data. Samples containing 15 wt % ferric oxide, 15 wt % feldspar, 20 wt % ball clay, 40 wt % kaolin, 10 wt % sand exhibited the highest flexural strength of 45.34 MPa. The optimized flexural strength using design expert software gave a value of 41.6 MPa, based on the compositions containing 15 wt % ferric oxide, 15 wt % feldspar, 20 wt % ball clay, 40 wt % kaolin, 10 wt % sand. As seen, the optimized value is closely related to the experimental value. The tiles formed by these compositions are therefore classified as group BIa based on ISO 13006 standard for ceramic tiles. For water absorption, samples containing 15 wt % ferric oxide, 15 wt % feldspar, 20 wt % ball clay, 40 wt % kaolin, 10 wt % sand exhibited an experimental value of 9.62 % while the optimized value was 10.69 % based on 15 wt % ferric oxide, 15 wt % feldspar,

20 wt % ball clay, 40 wt % kaolin and 10 wt % sand. The ISO 13006 classified these samples as class BII_b non-vitreous tiles since the water absorption is in a range of 6-10 %. Therefore, based on the results obtained, the application of ferric oxide in making of tiles is feasible.

5.2 Recommendations

Basing on the conclusion made in section 5.1, the following recommendations should be considered for the development of ceramic tiles using ferric oxide as the replacement of feldspar.

i. Further research is needed to determine how different sintering temperatures affect the mechanical and physical qualities of ceramic tiles made using ferric oxide. This would assist in optimizing processing conditions for improved performance.
ii. Additional studies should explore broader ranges of ferric oxide content, combined with other raw materials, to further refine the formulation for enhanced strength and reduced water absorption.

REFERENCES.

Abd Halim, M. H., Mokhtar, N. A. M., Masnan, S. S. K., Talib, N. K., Jusoh, A. F., & Saidin, M. (2023). X-Ray Fluorescence (XRF) analysis of iron ore at ancient Kedah iron smelting site, Sungai Batu archaeological complex, Bujang Valley, Kedah, Malaysia. *Heliyon*, *9*(4), e14850. https://doi.org/10.1016/j.heliyon.2023.e14850

Abdullah, M., Ahmed, I., Arafat Islam, M., Ahsan, Z., & Saha, S. (2024). Recent developments and diverse applications of high melting point materials. *Results in Engineering*, *22*, 102376. https://doi.org/https://doi.org/10.1016/j.rineng.2024.102376

Aliyu, Z. S., Garkida, A. D., Ali, E. A., & Dauda, M. (2016). Characterization of feldspar by instrumental analytical techniques. *Characterization of Minerals, Metals, and Materials 2015*, 291–297. https://doi.org/10.1007/978-3-319-48191-3_36

Aljaradin, M., & Amareh, M. (2015). Characterization of the Jordanian Feldspar Raw Materials for Application in the Ceramic and Glass\nIndustries. *International Journal of Mining Engineering and Mineral Processing*, *November 2014*, 1–5. https://doi.org/10.5923/j.mining.20140302.02

Almeida, E. P., Carreiro, M. E. A., Rodrigues, A. M., Ferreira, H. S., Santana, L. N. L., Menezes, R. R., & Neves, G. A. (2021). A new eco-friendly mass formulation based on industrial mining residues for the manufacture of ceramic tiles. *Ceramics International*, *47*(8), 11340–11348. https://doi.org/https://doi.org/10.1016/j.ceramint.2020.12.260

Altimari, F., Andreola, F., Lancellotti, I., & Barbieri, L. (2024). Comparative study of technological behavior of German ball clay and Italian kaolinitic clay in unconventional porcelain stoneware body. *Applied Clay Science*, *255*, 107417. https://doi.org/https://doi.org/10.1016/j.clay.2024.107417

Alves, C. L., Skorych, V., De Noni, A., Hotza, D., González, S. Y. G., & Heinrich, S. (2024). Optimizing raw material composition to increase sustainability in porcelain tile production: A simulation-based approach. *Journal of the American Ceramic Society*, *107*(4), 2110–2127. https://doi.org/10.1111/jace.19581

Alves, H. J., Melchiades, F. G., & Boschi, A. O. (2012). Effect of feldspar particle size on the porous microstructure and stain resistance of polished porcelain tiles. *Journal of the European Ceramic Society*, *32*(10), 2095–2102. https://doi.org/https://doi.org/10.1016/j.jeurceramsoc.2012.03.019

Ariyanto, S. V., Joni, I., & Yunanto, F. (2023). Xrf and Xrd Testing for Sand Mineral Content Identification At Talang Siring Beach. *EduFisika: Jurnal Pendidikan Fisika*, *8*(2), 226–232. https://doi.org/10.59052/edufisika.v8i2.27428

Aronniemi, M., Lahtinen, J., & Hautojärvi, P. (2004). Characterization of iron oxide thin films. *Surface and Interface Analysis*, *36*(8), 1004–1006. https://doi.org/10.1002/sia.1823

Atidi, J., Kasedde, H., Menya, E., & Olupot, P. W. (2023). Optimization of physical and mechanical properties of porcelain tiles from coffee parchment husk ash. *Journal of Engineering Research*, *November*.

https://doi.org/10.1016/j.jer.2023.11.013

Ayalew, A. A., & Demir, I. (2023). Physiochemical Characterization of Ethiopian Mined Kaolin Clay through Beneficiation Process. *Advances in Materials Science and Engineering*, *2023*. https://doi.org/10.1155/2023/9104807

Aydın, T., Tarhan, M., & Tarhan, B. (2021). The Effect of Mould Filling on the Mechanical Properties of Wall Tile Production. *International Journal of Engineering Research and Development*, *13*(3), 40–48. https://doi.org/10.29137/umagd.1036506

Bauluz, B., Mayayo, M. J., Laita, E., & Yuste, A. (2021). Micro- and nanotexture and genesis of ball clays in the lower cretaceous (Se iberian range, ne spain). *Minerals*, *11*(12). https://doi.org/10.3390/min11121339

Bayer Ozturk, Z., Karaca, Y., Kurama, S., & Ubay, E. (2024). Evaluating pumice as a sustainable raw material in porcelain tile production: impact on technical properties. *Journal of the Australian Ceramic Society*, *60*(5), 1591–1599.

Bell, A. M. T., Backhouse, D. J., Deng, W., Eales, J. D., Kilinc, E., Love, K., Rautiyal, P., Rigby, J. C., Stone, A. H., Vaishnav, S., Wie-Addo, G., & Bingham, P. A. (2020). X-ray fluorescence analysis of feldspars and silicate glass: Effects of melting time on fused bead consistency and volatilisation. *Minerals*, *10*(5). https://doi.org/10.3390/min10050442

Benali, F., Hamidouche, M., Belhouchet, H., Bouaouadja, N., & Fantozzi, G.

(2016). Thermo-mechanical characterization of a silica-alumina refractory concrete based on calcined algerian kaolin. *Ceramics International*, *42*(8), 9703–9711. https://doi.org/10.1016/j.ceramint.2016.03.059

Benito, J. M., Conesa, A., Rubio, F., & Rodríguez, M. A. (2005). Preparation and characterization of tubular ceramic membranes for treatment of oil emulsions. *Journal of the European Ceramic Society*, *25*(11), 1895–1903. https://doi.org/10.1016/j.jeurceramsoc.2004.06.016

Blagojević, D., Lazić, D., Kešelj, D., Ostojić, G., & Imamović, M. (2018). Determination of titanium dioxide content in bauxites using X-ray fluorescence spectrometry by fusion and by pressing. *Acta Chimica Slovenica*, *65*(2), 380–387. https://doi.org/10.17344/acsi.2017.4098

Bombazaro, J. L., & Bernardin, A. M. (2022). Improving plasticity of kaolins by high-energy milling for use in porcelain tile compositions. *Open Ceramics*, *10*, 100256. https://doi.org/https://doi.org/10.1016/j.oceram.2022.100256

Boulos, T. R., Ibrahim, S. S., & Yehia, A. (2015). Differential Flotation of Some Egyptian Feldspars for Separation of Both Silica and Iron Oxides Contaminants. *Journal of Minerals and Materials Characterization and Engineering*, *03*(06), 435–443. https://doi.org/10.4236/jmmce.2015.36046

Bouzerara, F., Harabi, A., & Condom, S. (2009). Porous ceramic membranes prepared from kaolin. *Desalination and Water Treatment*, *12*(1–3), 415–419. https://doi.org/10.5004/dwt.2009.1051

Buyondo, A. K., Kasedde, H., Kirabira, J. B., & Bongomin, O. (2024). Characterization and treatment effects on Mutaka kaolin for additive in coatings: Mineral composition, thermal and structural modifications. *Heliyon*, *10*(1), e24238. https://doi.org/10.1016/j.heliyon.2024.e24238

Cox, M. R., & Budhu, M. (2008). A practical approach to grain shape quantification. *Engineering Geology*, *96*(1–2), 1–16. https://doi.org/10.1016/j.enggeo.2007.05.005

Cui, K., Zhang, Y., Fu, T., Wang, J., & Zhang, X. (2020). Toughening Mechanism of Mullite Matrix Composites: A Review. In *Coatings* (Vol. 10, Issue 7). https://doi.org/10.3390/coatings10070672

Das, S. K., Dana, K., Singh, N., & Sarkar, R. (2005). Shrinkage and strength behaviour of quartzitic and kaolinitic clays in wall tile compositions. *Applied Clay Science*, *29*(2), 137–143. https://doi.org/https://doi.org/10.1016/j.clay.2004.10.002

De Noni, A., Hotza, D., Soler, V. C., & Vilches, E. S. (2009). Effect of quartz particle size on the mechanical behaviour of porcelain tile subjected to different cooling rates. *Journal of the European Ceramic Society*, *29*(6), 1039–1046. https://doi.org/https://doi.org/10.1016/j.jeurceramsoc.2008.07.052

Dewi, R., Agusnar, H., Alfian, Z., & Tamrin. (2018). Characterization of technical kaolin using XRF, SEM, XRD, FTIR and its potentials as industrial raw materials. *Journal of Physics: Conference Series*, *1116*(4). https://doi.org/10.1088/1742-6596/1116/4/042010

Dhivya, A., & Keshav, A. (2022). Fabrication of ball clay based low-cost ceramic membrane supports and their characterization for microfiltration application. *Journal of the Indian Chemical Society*, *99*(7), 100557. https://doi.org/https://doi.org/10.1016/j.jics.2022.100557

Druckrey, A. M., Alshibli, K. A., & Al-Raoush, R. I. (2016). 3D characterization of sand particle-to-particle contact and morphology. *Computers and Geotechnics*, *74*, 26–35. https://doi.org/10.1016/j.compgeo.2015.12.014

Dutra, R. P. S., Pereira, L. M., Souza, P. D. P., Nascimento, R. M., Martinelli, A. E., & Paskocimas, C. A. (2008). *Study of Water Absorption By Preparation of Ceramic Bodies With Different Clays for Porcelain Tile Manufacture*. 131–134.

Ekincioglu, M. (2023). *Ekincioglu, M. (speaker), 2023, Hacking MIT's McCormick Hall's Archive: Architecture and Wellness, the 76th SAH Annual International Conference, September 22. (Virtual session)., h... September*.

Elakhame, Z. U., Ifebhor, F., & Asotah, W. A. (2016). Development and Production of Ceramic Tiles From Waste Bottle Powder (Milled Glass). *Kathmandu University Journal of Science, Engineering and Technology*, *12*(2), 50–59. https://doi.org/10.3126/kuset.v12i2.21521

Elgamouz, A., Tijani, N., Shehadi, I., Hasan, K., & Al-Farooq Kawam, M. (2019). Characterization of the firing behaviour of an illite-kaolinite clay mineral and its potential use as membrane support. *Heliyon*, *5*(8), e02281. https://doi.org/10.1016/j.heliyon.2019.e02281

Ezra, R. (2022). Deconstructing Glass and Building up Shards at the Early Royal Society. *Renaissance Quarterly*, *75*(1), 88–135. https://doi.org/DOI: 10.1017/rqx.2021.331

Fatile, O. (2014). Characterization of Vitrified Porcelain Tiles using Feldspar from Three Selected Deposits in Nigeria. *Research Journal of Recent Sciences*, *3*(9), 67–72.

Fragassa, C. (2015). Limits in application of international standards to innovative ceramic solutions. *International Journal for Quality Research*, *9*(2), 279–298.

Fujishiro, K., Kawamura, G., Matsuda, A., Tan, W. K., & Muto, H. (2025). Electrostatically Design of Composite Particles for Efficient Ceramics Sintering. *Funtai Oyobi Fummatsu Yakin/Journal of the Japan Society of Powder and Powder Metallurgy*, *72*, S1029–S1032. https://doi.org/10.2497/jjspm.16A-T7-18

Furszyfer Del Rio, D. D., Sovacool, B. K., Foley, A. M., Griffiths, S., Bazilian, M., Kim, J., & Rooney, D. (2022). Decarbonizing the ceramics industry: A systematic and critical review of policy options, developments and sociotechnical systems. *Renewable and Sustainable Energy Reviews*, *157*(July 2021), 112081. https://doi.org/10.1016/j.rser.2022.112081

Gautam, L., Jain, J. K., Kalla, P., & Danish, M. (2021). Sustainable utilization of granite waste in the production of green construction products: A review. *Materials Today: Proceedings*, *44*, 4196–4203. https://doi.org/https://doi.org/10.1016/j.matpr.2020.10.532

Ghosh, S., Das, M., Chakrabarti, S., & Ghatak, S. (2002). Development of ceramic tiles from common clay and blast furnace slag. *Ceramics International*, *28*(4), 393–400. https://doi.org/10.1016/S0272-8842(01)00107-9

Gikunju, E. M., Bosire, G. O., Onyari, J. M., Nyongesa, F. W., & Beleta, D. (2024). Physico-chemical characterization of feldspars for application as fluxing agents: Experimental and ab initio computational approaches. *Physics and Chemistry of the Earth, Parts A/B/C*, *135*, 103651. https://doi.org/https://doi.org/10.1016/j.pce.2024.103651

Gorelova, L. A. (2023). Phase Transformations in Feldspar Group Minerals with Paracelsian Topology under High Temperature and High Pressure. *Russian Geology and Geophysics*, *64*(8), 950–961. https://doi.org/10.2113/RGG20234557

Guo, D., Liu, H., Zang, C., Wang, Y., Sun, F., Lei, D., Wu, J., Zhu, H., & Wang, Z. (2024). Experimental study on the direct firing of ceramic ware using concentrated solar energy. *IScience*, *27*(7), 110222. https://doi.org/10.1016/j.isci.2024.110222

Iqbal, Y., & Lee, W. E. (2000). Microstructural evolution in triaxial porcelain. *Journal of the American Ceramic Society*, *83*(12), 3121–3127. https://doi.org/10.1111/j.1151-2916.2000.tb01692.x

Isobe, T., Ooyama, A., Shimizu, M., & Nakajima, A. (2012). Pore size control of Al2O3 ceramics using two-step sintering. *Ceramics International*, *38*(1), 787–793. https://doi.org/10.1016/j.ceramint.2011.08.005

Iwaszko, J., Kudła, K., & Lubas, M. (2024). Application of Product of Vitrification of Asbestos-Cement Waste and CRT Glass Cullet as Reinforcing Phase in Surface Composites Produced by FSP Method. *Materials*, *17*(22), 1–9. https://doi.org/10.3390/ma17225508

Jalaluddin, M. L., Azlan, U. A. A., Rashid, M. W. A., & Tamin, N. (2024). Effect of sintering temperatures on the physical, structural properties and microstructure of mullite-based ceramics. *AIMS Materials Science*, *11*(2), 243–255. https://doi.org/10.3934/MATERSCI.2024014

Janjaroen, D., Dilokdumkeng, P., & Jhandrta, P. (2018). Effect of water hardness and pH on adsorption kinetic of arsenate on iron oxide. *Engineering Journal*, *22*(2), 13–23. https://doi.org/10.4186/ej.2018.22.2.13

Jayaweera, J. M. N., Narayana, M., & Adikary, S. U. (2024). Modeling and simulation of ceramic tiles linear shrinkage variation during the sintering process. *Forces in Mechanics*, *15*, 100274. https://doi.org/https://doi.org/10.1016/j.finmec.2024.100274

Karslıoğlu, A., Onur, M. İ., & Balaban, E. (2022). Investigation of boron waste usage in civil engineering applications TT - İnşaat mühendisliği uygulamalarında bor atıklarının kullanımının araştırılması. *Niğde Ömer Halisdemir Üniversitesi Mühendislik Bilimleri Dergisi*, *11*(3), 727–735. https://doi.org/10.28948/ngumuh.1084831

Khalil, A. K. A., Elgamouz, A., Nazir, S., Atieh, M. A., Alawadhi, H., & Laoui, T. (2024). Preparation and characterization of clay based ceramic porous membranes and their use for the removal of lead ions from synthetic

wastewater with an insight into the removal mechanism. *Heliyon*, *10*(3), e24939. https://doi.org/10.1016/j.heliyon.2024.e24939

Khater, G. A., Romero, M., López-Delgado, A., Padilla, I., El-Kheshen, A. A., Farag, M. M., Elmaghraby, M. S., Nasralla, N., & Shendy, H. (2024). Novel ceramic materials based on industrial wastes within the CaO-MgO-Al2O3-SiO2 system. *Materials Chemistry and Physics*, *331*, 130178. https://doi.org/10.1016/j.matchemphys.2024.130178

Kurian, M., & Thankachan, S. (2023). 1 - Introduction: ceramics classification and applications. In M. Kurian, S. Thankachan, & S. S. B. T.-C. C. Nair (Eds.), *Elsevier Series in Advanced Ceramic Materials* (pp. 1–17). Elsevier. https://doi.org/https://doi.org/10.1016/B978-0-323-85746-8.00009-6

Leide, A. (n.d.). Reaction-bonded silicon carbide for nuclear fusion blanket applications VO - RT - Thesis. In *OP* - (Issue WP-).

Li, J., Peng, J., Guo, S., & Zhang, L. (2013). Application of response surface methodology (RSM) for optimization of the sintering process of preparation calcia partially stabilized zirconia (CaO-PSZ) using natural baddeleyite. *Ceramics International*, *39*, 197–202. https://doi.org/10.1016/j.ceramint.2012.06.009

Liang, Q., Feng, X., Zhang, K., Li, J., & Hou, X. (2022). Measuring device for thermal expansion coefficient and shrinkage rate during cure process of thermosetting resin. *Yi Qi Yi Biao Xue Bao/Chinese Journal of Scientific Instrument*, *43*, 35–43. https://doi.org/10.19650/j.cnki.cjsi.J2109082

Lindex. (2022). Sustainability Report 2022. *Report:*, 1–69.

Liu, C., Zhou, J., & Lu, J. (2025). *Sinterability , structural evolution and pinhole elimination of high strength self-glazed glass-ceramics sintered from granite sludge by instant glaze firing*. *3*(1), 1–15.

Liu, M., Ma, G., Zhang, X., Liu, J., & Wang, Q. (2020). Preparation of black ceramic tiles using waste copper slag and stainless steel slag of electric arc furnace. *Materials*, *13*(3), 5–10. https://doi.org/10.3390/ma13030776

Mankai, S., Madiouli, J., Sghaier, J., & Lecomte, D. (2018). Determination of porosity from shrinkage curves during sintering of granular materials. *Drying Technology*, *36*(5), 557–566. https://doi.org/10.1080/07373937.2017.1348358

Martín-Márquez, J., Rincón, J. M., & Romero, M. (2010). Mullite development on firing in porcelain stoneware bodies. *Journal of the European Ceramic Society*, *30*(7), 1599–1607. https://doi.org/10.1016/j.jeurceramsoc.2010.01.002

Menegazzo, A. P. M., Dias, L. L., Jodas, L. S., & Silva, F. D. (2022). *Study of Different Test Methods for Determining Water Absorption in Ceramic Tiles*. *November*, 1–3. https://doi.org/10.13140/RG.2.2.14805.70885

Mohamed, A., Ngida, R., Farag, R., & Zawrah, M. (2024). Industrial Wastes for Production of Thermally Stable and Corrosion Resistant alumino-silicate Refractory Ceramic Bodies. *Journal of Inorganic and Organometallic Polymers and Materials*, *34*, 4661–4673. https://doi.org/10.1007/s10904-

024-03108-1

Morsy, F. A., El-Sherbiny, S., Hassan, M. S., & Mohammed, H. F. (2014). Modification and evaluation of Egyptian kaolinite as pigment for paper coating. *Powder Technology*, *264*, 430–438. https://doi.org/10.1016/j.powtec.2014.05.040

Muthukumar, B., Duraimurugan, R., Parthipan, P., Rajamohan, R., Rajagopal, R., Narenkumar, J., Rajasekar, A., & Malik, T. (2024). Synthesis and characterization of iron oxide nanoparticles from Lawsonia inermis and its effect on the biodegradation of crude oil hydrocarbon. *Scientific Reports*, *14*(1), 1–11. https://doi.org/10.1038/s41598-024-61760-6

Nigussie, A., Demisse, T., & Getaneh, W. (2023). Industrial properties and uses of silica sand from Blue Nile Basin, Central Ethiopia. *Arabian Journal of Geosciences*, *16*(3), 213. https://doi.org/10.1007/s12517-023-11302-7

Njoya, D., Tadjuidje, F. S., Ndzana, E. J. A., Pountouonchi, A., Tessier-Doyen, N., & Lecomte-Nana, G. (2017). Effect of flux content and heating rate on the microstructure and technological properties of Mayouom (Western-Cameroon) kaolinite clay based ceramics. *Journal of Asian Ceramic Societies*, *5*(4), 422–426. https://doi.org/10.1016/j.jascer.2017.09.004

Obolkina, T. O., Goldberg, M. A., Smirnov, V. V, Smirnov, S. V, Titov, D. D., Konovalov, A. A., Kudryavtsev, E. A., Antonova, O. S., Barinov, S. M., & Komlev, V. S. (2020). Increasing the Sintering Rate and Strength of ZrO2–Al2O3 Ceramic Materials by Iron Oxide Additions. *Inorganic Materials*, *56*(2), 182–189. https://doi.org/10.1134/S0020168520020156

Ochen, W., D'ujanga, F. M., & Oruru, B. (2019). Microstructure and Residual Stress Effect on the Flexural Strength of Porcelain Tiles Formulated from Locally Available Materials in Uganda. *East African Journal of Science, Technology and Innovation*, *1*(1), 1–10. https://doi.org/10.37425/eajsti.v1i1.73

Ochen, W., D'ujanga, F. M., Oruru, B., & Olupot, P. W. (2021a). Physical and mechanical properties of porcelain tiles made from raw materials in Uganda. *Results in Materials*, *11*, 100195. https://doi.org/https://doi.org/10.1016/j.rinma.2021.100195

Ochen, W., D'ujanga, F. M., Oruru, B., & Olupot, P. W. (2021b). Physical and mechanical properties of porcelain tiles made from raw materials in Uganda. *Results in Materials*, *11*, 100195. https://doi.org/10.1016/j.rinma.2021.100195

Odzijewicz, J. I., Wołejko, E., Wydro, U., Wasil, M., & Jabłońska-Trypuć, A. (2022). Utilization of Ashes from Biomass Combustion. In *Energies* (Vol. 15, Issue 24). https://doi.org/10.3390/en15249653

Olanrewaju, O., & Afolabi, O. A. (2024). *Processing and Applications of Composite Ceramic Materials for Emerging Technologies* (A. Borrell Tomás & R. Benavente Martínez (eds.)). IntechOpen. https://doi.org/10.5772/intechopen.1007296

Olupot, P. W. (2006). *Assessment of Ceramic Raw Materials in Uganda for Electrical Porcelain Peter Wilberforce Olupot*.

Olupot, P. W., Jonsson, S., & Byaruhanga, J. K. (2006). *Electroporcelains from Raw Materials in Uganda: A Review* (J. A. Mwakali & G. B. T.-P. from the I. C. on A. in E. and T. Taban-Wani (eds.); pp. 454–464). Elsevier Science Ltd. https://doi.org/https://doi.org/10.1016/B978-008045312-5/50049-2

Osman, R. A. (2021). Assessment of Chemical and Mineralogical Features on Silica Sand and its Potential Industrial Applications at Elwadi Elgedid, Western Desert, Egypt. *International Journal of Innovative Science, Engineering & Technology*, *8*(10), 99–115.

Ozturk, Z. B., Karaca, Y., Kurama, S., Ubay, E., & Cengiz, U. (2025). Utilizing waste zirconia nozzles for eco-friendly ceramic tile production. *Journal of Ceramic Processing Research*, *26*(1), 43–50. https://doi.org/10.36410/jcpr.2025.26.1.43

Panzi Mukhokosi, E., Mukwaya, G. W., & Enjiku, B. (2023). Structural and Mechanical Properties of Non-Glazed Ceramic Tiles Developed from Selected Mineral Deposits in Uganda. *Nano-Horizons*, *2*(2), 1–14. https://doi.org/10.25159/nanohorizons/13816

Park, H.-Y., Lee, H.-J., Seo, H., Kim, H., Choi, H., Kim, B.-G., Yeo, J., Heo, S. Y., Jung, Y.-G., Byeun, Y.-K., Yang, B., & Yang, S. (2024). Improvement of mechanical properties of ceramic green body and fired body by aging of inorganic binder in ceramic slurry for 3D printing. *Journal of the European Ceramic Society*, *44*(5), 3400–3409. https://doi.org/https://doi.org/10.1016/j.jeurceramsoc.2023.12.066

Patrick, D. O., Kefas, H. M., John, Y. M., & Ameh, V. I. (2015). Investigation of the physical properties of tiles produced with Otukpo clay. *Leonardo Electronic Journal of Practices and Technologies*, *14*(27), 162–176.

Piemonti, A., Conforti, A., Cominoli, L., Sorlini, S., Luciano, A., & Plizzari, G. (2021). Use of Iron and Steel Slags in Concrete: State of the Art and Future Perspectives. In *Sustainability* (Vol. 13, Issue 2). https://doi.org/10.3390/su13020556

Prahara, E., & Meilani. (2014). Compressive strength and water absorption of pervious concrete that using the fragments of ceramics and roof tiles. *EPJ Web of Conferences*, *68*, 2–6. https://doi.org/10.1051/epjconf/20146800015

Robertson, I., Holzer, L., Prestat, M., Münch, B., & Graule, T. (2010). Effects of particle and pore sizes, surface area and porosity on the performance of LSC cathodes. *Proceedings of the 9th European Fuel Cell Forum*, 10–83.

Romero, M., Padilla, I., Contreras, M., & López-Delgado, A. (2021). Mullite-Based Ceramics from Mining Waste: A Review. In *Minerals* (Vol. 11, Issue 3). https://doi.org/10.3390/min11030332

Saponjic, A., Maletaškić, J., Radovanović, Ž., Pošarac-Marković, M., & Gordić, M. (2024). Properties of Durable Mullite Bodies Manufactured from Waste Clay-Diatomite. *Metallurgical and Materials Data*, *2*(2), 55–58. https://doi.org/10.30544/mmd32

Sawadogo, A., Cissé, H., Taale, E., Kambou, A., Ouédraogo, C. P., Séré, L.,

Sondo, A., Zongo, C., & Savadogo, A. (2023). Assessment of the Sanitary Quality of Precooked Cereal-Based Foods Produced in Ouagadougou, Burkina Faso. *Journal of Applied Life Sciences International*, *26*(6), 48–57. https://doi.org/10.9734/jalsi/2023/v26i6627

Silveira, J., Leite, J. P., & Pessoa, J. (2010). Technique for optimization of ceramic bodies using mixture design (Técnica para otimização de corpos cerâmicos usando projeto de misturas). *Matrix*, *56*, 347–354.

Sonuparlak, B., Sarikaya, M., & Aksay, I. (2005). Spinel Phase Formation During the 980°C Exothermic Reaction in the Kaolinite-to-Mullite Reaction Series. *Journal of the American Ceramic Society*, *70*, 837–842. https://doi.org/10.1111/j.1151-2916.1987.tb05637.x

Stathis, G., Ekonomakou, A., Stournaras, C. J., & Ftikos, C. (2004). Effect of firing conditions, filler grain size and quartz content on bending strength and physical properties of sanitaryware porcelain. *Journal of the European Ceramic Society*, *24*(8), 2357–2366. https://doi.org/10.1016/j.jeurceramsoc.2003.07.003

Taib, M. (2020). 2019 Minerals Yearbook. *Office National Des Hydrocarbures et Des Mines*, *6*, 29.

Varghese, L., Iveth Cedillo-González, E., Cattini, A., Vacchi, M., & Siligardi, C. (2024). Frit-Free solar reflective porcelain stoneware ceramic tiles using recycled granite Waste: An investigation on its engobe and glaze formulations. *Energy and Buildings*, *311*, 114129. https://doi.org/https://doi.org/10.1016/j.enbuild.2024.114129

Vasić, M. V., Mijatović, N., & Radojević, Z. (2022). Aplitic Granite Waste as Raw Material for the Production of Outdoor Ceramic Floor Tiles. *Materials*, *15*(9). https://doi.org/10.3390/ma15093145

Vieira, A. W., Daniel, M., Innocentini, D. M., Mendes, E., Gomes, T., Demarch, A., Rubem, O., Montedo, K., & Angioletto, E. (2017). Comparison of Methods for Determining the Water Absorption of Glazed Porcelain Stoneware Ceramic Tiles. *Materials Research*, *20*(2), 637–643.

Wang, C., Zhong, W., Ping, W., Lin, Z., Wang, R., Dai, J., Guo, M., Xiong, W., Zhao, J. C., & Hu, L. (2021). Rapid Synthesis and Sintering of Metals from Powders. *Advanced Science*, *8*(12), 1–6. https://doi.org/10.1002/advs.202004229

Wang, S., Eng, B., & Eng, M. (2023). *Effects of Kaolinite, Vermiculite and Palygorskite on Fired Clay Brick Properties*.

Yakubu, K. (2025). *Effect of Particle Size on the Mechanical , Water Absorption and Thermal Properties of Flamboyant Seed Particle-filled Polyester Composites for Tile Applications*. *3121*, 34–43.

Yan, W., Li, N., Tong, J., Liu, G., & Xu, J. (2013). Effect of particle size on the pore characterization and strength of porous cordierite-mullite ceramics prepared by a pore-forming in-situ technique. *Science of Sintering*, *45*(2), 165–172. https://doi.org/10.2298/SOS1302165Y

Yaya, A., Tiburu, E. K., Vickers, M. E., Efavi, J. K., Onwona-Agyeman, B., & Knowles, K. M. (2017). Characterisation and identification of local kaolin

clay from Ghana: A potential material for electroporcelain insulator fabrication. *Applied Clay Science*, *150*(September), 125–130. https://doi.org/10.1016/j.clay.2017.09.015

Yibing, T. (2020). Technical analysis of water absorption rate of ceramic tiles. *E3S Web of Conferences*, *185*, 1–3. https://doi.org/10.1051/e3sconf/202018504039

Yuan, G., Cao, Y., Schulz, H. M., Hao, F., Gluyas, J., Liu, K., Yang, T., Wang, Y., Xi, K., & Li, F. (2019). A review of feldspar alteration and its geological significance in sedimentary basins: From shallow aquifers to deep hydrocarbon reservoirs. *Earth-Science Reviews*, *191*(February), 114–140. https://doi.org/10.1016/j.earscirev.2019.02.004

Zanelli, C., Conte, S., Molinari, C., Soldati, R., & Dondi, M. (2021). Waste recycling in ceramic tiles: a technological outlook. *Resources, Conservation and Recycling*, *168*(November), 105289. https://doi.org/10.1016/j.resconrec.2020.105289

Zawada, A., Przerada, I., Lubas, M., Sitarz, M., & Leśniak, M. (2021). Application of statistical methods in predicting the properties of glass-ceramic materials obtained from inorganic solid waste. *Materials*, *14*(10). https://doi.org/10.3390/ma14102651

Zawrah, M. F., Taha, M. A., & Youness, R. A. (2024). Advanced Ceramics: Stages of Development. In S. J. Ikhmayies (Ed.), *Advanced Ceramics* (pp. 1–46). Springer Nature Switzerland. https://doi.org/10.1007/978-3-031-43918-6_1

Zewdie, T. M., Prihatiningtyas, I., Dutta, A., Gabbiye Habtu, N., & van der Bruggen, B. (2021). Characterization and beneficiation of Ethiopian kaolin for use in fabrication of ceramic membrane. *Materials Research Express*, *8*(11), 115201. https://doi.org/10.1088/2053-1591/ac2f75

Zhao, L., Li, Y., Zhang, L., & Cang, D. (2017). Effects of CaO and Fe2O3 on the microstructure and mechanical properties of SiO2-CaO-MgO-Fe2O3 ceramics from steel slag. *ISIJ International*, *57*(1), 15–22. https://doi.org/10.2355/isijinternational.ISIJINT-2016-064

Zheng, N., Gao, H., & Chen, X. (2025). Properties and prediction of dry shrinkage deformation in cement-stabilised sand and gravel. *Road Materials and Pavement Design*, 1–18.

ZHOU, Q., LI, C., LI, X., PENG, Z., LIU, G., & QI, T. (2016). Reaction of ferric oxide in system during reductive sintering process.

APPENDIX I:

Figure A 1: (a) Raw ball clay, (b) filtration of ball clay paste, (c) soaking of raw materials in water, (d) sieving to remove impurities, (e) impurities found in sand, (f) mixing of raw materials.

Figure A 2: (a) Ferric oxide waste at a steel factory, (b) green bodies after pressing, (c) sample tiles after firing.